UC Berkeley
UC Berkeley Electronic Theses and Dissertations

Title
Charge and Thermal Transport in Oxide Nanowire Systems

Permalink
https://escholarship.org/uc/item/3cn4d9qv

Author
Andrews, Sean Charles

Publication Date
2013

Peer reviewed|Thesis/dissertation

eScholarship.org
Powered by the California Digital Library
University of California

Charge and Thermal Transport in Oxide Nanowire Systems

By

Sean Andrews

A dissertation submitted in partial satisfaction of the requirement for the degree

Doctor of Philosophy

in

Chemistry

in the

Graduate Division

of the

University of California, Berkeley

Committee in Charge:

Professor Peidong Yang, Chair
Professor Gabor Somorjai
Professor Junqiao Wu

Spring 2013

Charge and Thermal Transport in Oxide Nanowire Systems

© 2013

by Sean Andrews

Abstract

Charge and Thermal Transport in Oxide Nanowire Systems

by

Sean Andrews

Doctor of Philosophy in Chemistry

University of California, Berkeley

Professor Peidong Yang, Chair

Due to their unique properties, nanostructured materials have developed into promising components for next-generation optoelectronic and energy converting devices. Their nanoscale dimensions and features allow for incredible interactions with phenomena occurring at similar length scales. Nanowires made of oxide materials are especially attractive for controlling the transport of phonons, photons, and charged species for added thermal and chemical stability. By controlling the nanowire dimensions, the propagation of these species can be tailored to be suitable in a variety of applications, even those operating at elevated temperatures.

One of these applications is thermoelectrics, where the conversion of heat to electricity occurs entirely in the solid-state. Though decades of research yielded little progress due to the limiting interdependencies of transport properties, the nanowire geometry allows for the decoupling of the otherwise tethered conduction of heat and charge. By merely existing in the size regime between the respective mean free paths of electrons and phonons, thermal conduction can be impeded by increased phonon boundary scattering while the electrons can proceed with mobility of a single crystal. However, further phonon scattering can occur with the addition of nanostructured features along the length of the nanowire. To accomplish this, $InXO_3(ZnO)_n$ (X = Ga, Fe) polytypoid nanowires were synthesized using a facile, solid-state conversion scheme. Using aberration correction Z-contrast electron microscopy, detailed analysis of the resulting structure lead to the discovery of the formation of single atomic sheets of In existing within the ZnO matrix. Evidence is provided that these octahedrally coordinated In planes act as inversion domain boundaries and necessitate the existence of polarity-restoring "zig-zag" features between them. With experimental observations coupled with DFT calculations, both a structure model and formation mechanism are proposed. Single nanowire thermoelectric measurements on In-Ga-ZnO reveal simultaneous improvement in all the factors that contribute to the thermoelectric conversion efficiency. This is the first demonstration of enhancement of all three thermoelectric parameters in a nanowire system.

ZnO-based nanowires could also hold the key to nanosized optoelectronic interconnects and lasers. Because of its high optical gain, lasing is easily achieved in ZnO nanostructures via optical pumping. However, any actual device integration requires the input power to be electrical. The most common way to electrically pump a material is to create a homo-junction

diode, meaning both n- and p-type conduction has to be present in a single material. Therefore, much work has been done to achieve p-type ZnO, with limited success and repeatability caused from compensation from intrinsically-occurring donor defects. A strategy avoiding such compensation was employed via *in situ* Li incorporation during the chemical vapor transport growth, followed by dopant activation annealing. X-ray diffraction and photoluminescence qualitatively confirmed the incorporation of Li into the ZnO nanowires using this method. Field effect transconductance exhibited p-type behavior after the annealing step. The sign of the Seebeck Coefficient confirmed that the majority carrier type was positive. However, the p-type behavior only lasted a matter of days, where the longevity may have a direct relation on the nanowire diameter. Unfortunately, the growth of these Li-doped ZnO nanowires was unable to be reproduced for a variety of possible reasons. However, the data collected may help make p-type conduction a reliable reality.

The large amount of surface in the nanowire geometry allows for exploration into interface effects on ionic transport for use as electrolytes in solid-oxide fuel cells. These energy producing devices currently only operate at high temperature, due to the relative energy needed for ionic conduction. Therefore, much effort has been directed towards designing material systems to conduct ions at lower temperature. One strategy is to utilize interfaces in nanostructured systems, which can exhibit strain and space charge effects, to provide pathways of lesser resistance for ionic migration. To explore the possibilities of these effects, core/shell CeO_2/ZrO_2 nanowires were studied. First, CeO_2 were hydrothermally grown nanowires and dried into thin films. A ZrO_2 coating of a few nanowires was added and calcined to promote crystallinity. TEM and STEM images show that there is no coherence between the two materials. However, the ionic conductivity increased by an order of magnitude upon addition of the ZrO_2. Furthermore, the activation energy of the coated samples is decreased by ~30%, indicating the interface is playing a role in changing the mechanism of ionic conduction. These results give hope to the eventual discovery of a nanostructured oxide material capable of ionic conduction at room temperature.

These studies on various oxide nanowire systems help provide experimental merit to the theoretical benefits and disadvantages of nanostructured materials. Thermoelectric material performance was enhanced due to the presence of nanostructured inclusions in converted ZnO-based polytypoid nanowires. P-type conduction was attained in Li-doped ZnO, but the larger surface to volume ratio of the nanowire geometry may indeed limit stability. Effects of the designed boundary between CeO_2 and ZrO_2 were seen in the conduction of oxygen because of the shear amount of interfacial density present in the nanowire thin films. These studies take advantage of the intrinsic properties of nanostructured materials and bring the implementation of nanowires to marketable applications closer to reality.

I dedicate this dissertation to my Grandfather, Charles Andrews.
May my life inspire the lives of those around me, as yours did mine.

Table of Contents

Chapter 1 Introduction

1.1 Why Nanostructured Materials? ____ 1
- 1.1.a The Specialty of Nanostructuring ____ 1
- 1.1.b Appropriate Application ____ 1

1.2 Nanowire synthesis ____ 2
- 1.2.a Gas-Phase vs. Solution-Phase ____ 2
- 1.2.b Conversion Chemistry ____ 3

1.3 Nanowires Effects in Energy Conversion Applications ____ 3
- 1.3.a Thermoelectricity ____ 3
- 1.3.b Solid-Oxide Fuel Cells ____ 5

1.4 References ____ 6

Chapter 2 ZnO-based Polytypoid Nanowires and their Thermoelectric Properties

2.1 Introduction ____ 11
- 2.1.a Better Nanowire Designs for Thermoelectric Transport ____ 11
- 2.1.b Indium-Ga-ZnO Alloys ____ 12

2.2 Synthesis of Polytypoid Nanowires via Solid-State Conversion ____ 13

2.3 Structure Determination of IXZO (X = Ga, Fe) Nanowires ____ 16
- 2.3.a XRD, EDS, and CTEM ____ 16
- 2.3.b Control of Inclusion Spacing and Density ____ 18
- 2.3.c InO_2^- Plane Inclusion Structure ____ 20
- 2.3.d Zig-Zag Structure and Model ____ 23
- 2.3.e Formation Mechanism of Inclusion Layers ____ 27

2.4 Thermoelectric Transport in IGZO Nanowires ____ 29
- 2.4.a Electrical Conduction ____ 30
- 2.4.b Seebeck Coefficient ____ 31
- 2.4.c Carrier Mobility and Power Factor ____ 32
- 2.4.d Thermal Conductivity and Figure of Merit ____ 33

2.5 Conclusions ____ 35

2.6 References ____ 36

Chapter 3: The possibility of P-type ZnO Nanowires

3.1 Introduction ____ 41
3.1.a The importance of p-type ZnO ____ 41
3.1.b Obstacles to p-type Conduction in ZnO ____ 42
3.1.c Strategy to Bypass Compensation ____ 43
3.2 Li-doped ZnO Nanowires ____ 44
3.2.a Synthesis and Conversion ____ 44
3.2.b Solid-state Characterization ____ 45
3.3 Carrier Type Determination ____ 48
3.3.a Field-Effect Conduction ____ 48
3.3.b Seebeck Coefficient ____ 49
3.4 Stability and Reproducibility ____ 51
3.4.a As function of Size and Time ____ 51
3.4.d Thoughts on Issues with Reproducibility ____ 52
3.5 Conclusions ____ 53
3.6 References ____ 54

Chapter 4: Ionic Conduction in Core/Shell Oxide Nanowires

4.1 Introduction ____ 57
4.1.a Conduction in CeO_2 and ZrO_2 ____ 57
4.2.b Nanoscale Effects on Ionic Conduction in Oxides ____ 57
4.2 Synthesis of CeO_2/ZrO_2 Core Shell Nanowires ____ 58
4.2.a Hydrothermal Synthesis and Coating Method ____ 58
4.2.b Shell Crystallization ____ 60
4.3.c Interfacial structure ____ 60
4.3 Nanowire Thin Film ____ 61
4.3.a ZrO_2 Coating Schemes ____ 61
4.3.b Thin Film Creation and Optimization ____ 62
4.3.c Contacting Considerations ____ 63
4.4 Impedance Measurements ____ 63
4.4.a Activation Energy ____ 64
4.4.b Ionic Transport Number ____ 65
4.4.c Dependence on O_2 Partial Pressure ____ 66
4.5 Conclusions ____ 67
4.6 References ____ 68

Appendix: List of Publications ____ 70

Acknowledgements

My work at Berkley would not have been accomplished if not for the support, assistance, and encouragement from my friends, family, and coworkers, both near and far. Whether it was through scientific discussions or gift packages sent in the mail, the interactions by those dearest to me have directly impacted the work presented in this dissertation.

Specifically, I would first like to thank my advisor, Professor Peidong Yang. His drive to find and create new areas of quality research has and continues to inspire me towards furthering my own goals in basic and applied research. I have not only benefitted from the opportunity to work within his lab, but also by observing his way of interacting within the scientific community and abroad. And I will forever be grateful for Jiro, as I too dream of that sushi.

Next, I am extremely grateful for my family, specifically my parents, John and Carol, whose love and support of me and my career goals has never wavered. They have forever been role models for me, providing me with a template of how Godly people should be, in both word and deed. Always knowing that they are there to help has allowed me to pursue goals I otherwise may not have. My brother Derek has also been a source of support, but also a role model in how he lives his life and what he has accomplished so far. I hope to one day achieve the level of success both professionally and personally that he has.

Many friends from back in Wisconsin and here in Berkeley deserve much thanks and appreciation as well. While there are many in this group, I would like to give special thanks to a few. To Eric McDermid, whether it has been camping in the wilderness of Yellowstone or sitting silent in a room for hours while we quest, I have been- and always shall be- his friend. To Chris Hahn, who was not only always available for throwing the football during the day or eating at In-n-Out after going to the range, but who taught me what it was to be a true Cal Bear. To Dave Unruh, who I can always count on for an apparently can't miss 3-team parley that is sure to fail, as well as fantasy football team names. To Amy Cordones-Hahn, whose prowess at finding Vegas deals is matched only be her ability to run from danger. And to Dan Gargas, who has mentored me in the way of the Captain.

I would also like to express my thanks and appreciation to all the wonderfully skilled coworkers and colleges with whom I have had the pleasure to work, both at UC-Berkeley and Lawernce Berkeley National Lab. These people include my first-year mentor Allon Hochbaum, for discussions on science and baseball have helped shape the way I view those topics; mentor Vladimir Radmilovic, from whom I have learned both basic and advanced principles of electron microscopy and whose skill at microscopy is very difficult to match; Michael Moore, both for his work toward our shared projects and numerous deli hash breakfasts; Melissa Fardy, for her hard work on IGZO and ease of being startled; Anna Goldstein, for work on the zig-zag structure and singing with my guitar playing; Jongwoo Lim, who has been my brother in thermoelectric and comfy pants wearing; Joel Henzie, for his thoroughness and appreciation of science and beer; and finally to Anthony Fu, for excellent research discussions and slow ice skating. Others in the Yang group, both past and present, who have impacted my time at Berkeley include Erik Garnett, Alex Briseno, Hanwei Gao, Chong Liu, Sarah Brittman, Jaeho Lee, Neil Dasguta, Haoming Chen, and Hungta Wang.

Lastly, I would like to thank my love, Jackie. I cannot imagine where I would be or what life would be like without her love, support, and excellent cooking. I am so looking forward to our future together.

Once again, thank you all.

Chapter 1

Introduction

1.1 – Why Nanostructured Materials?

1.1.a – The Specialty of Nanostructuring

Few areas of research have witnessed the same boom of efforts and studies over the past decade as the area of semiconductor nanowires. Exponential growth in the number of nanowire related papers that have been published since 2001 indicate that great interest remains in this field.[1] But what makes nanostructured materials of such great interest? Consider the nanowire geometry: the intrinsic size regime implied by the name places the range of diameters between 1nm and several hundred nanometers, with relatively large aspect ratios. This length scale is on the same order as the interaction distances of many interesting and useful phenomena, including the wavelength of light, phonon and electron mean free paths, exciton Bohr radii, and many more.[2–5] Therefore, with the correct design, materials at these length scales can begin to create new and novel interactions with these phenomena not available with the use of bulk materials.[6–9]

Another benefit to nano-sized materials is the larger surface to volume ratio. The usefulness of this feature is obvious for applications such as catalysis, where it is desired to have the largest number of active sites per unit volume of the catalyst.[10,11] Moreover, unique catalytic properties have been observed as a function of particle size, giving rise to the possibilities of increasing the catalytic activity of previously inert materials.[12]

Lastly, the ability to synthesize single crystal nanowire now allows for the measurement of purely crystalline materials. Bulk single crystal materials are often difficult or expensive to fabricate,[13,14] whereas single crystal nanowire materials can be readily prepared.[3,15–23] Furthermore, some previously non-allowed alloys and crystal phases are now able to exist in nanowire, nanoparticle, or quantum well forms.[24–28] The properties of these highly crystalline materials can give another layer of control to experimental designs, as well as help deconvolute otherwise ambiguous results.

1.1.b – Appropriate Application

While nanowires and nanostructured materials hold great promise in some next-generation energy conversion devices and other applications, they are by no means a cure-all

solution. Specific reasons and rational must be present when applying a nanostructured geometry for a specific application. For example, the nanowire geometry allows a material to act as both the optical gain medium and resonating cavity for lasing applications.[29,30] Also, typical nanowire diameters lie in between the respective mean free paths of phonons and electrons, allowing for a decoupling of thermal and electrical conduction for thermoelectric application.[4,7,31] Without considerations like these, applying the nanowire geometry to a material system is likely a result of academic peer pressure.

1.2 – Nanowire Synthesis

Nanowire properties can be useful in a variety of applications, but other considerations other than the choice of material and its size can dictate those properties. Relatively large dependences on the synthetic route taken have been well documented in the literature.[32–41] The two main methods for bottle-up nanowire growth are designated by the phase of the precursors used: Gas-phase and Solution-Phase. The benefits and disadvantages of each are briefly addressed in the following section.

1.2.a – Gas-Phase vs. Solution-Phase

Typical gas-, or vapor-, phase deposition mechanisms of nanowire growth can be divided into two categories: those with and those without external catalysts.[42] For vapor deposition with foreign catalysts, vapor-liquid-solid (VLS) is the basic process. For vapor deposition without foreign catalysts, physical vapor deposition and chemical vapor deposition are usually applied. A typical VLS process consists of four sequential steps: (1) transport of the vapor phase precursor, (2) precursor adsorption and desorption at the catalyst surface, (3) material diffusion across the liquid alloy catalyst, and (4) precipitation of solid crystals forming the nanowire morphology.[43] Growth without foreign catalysts is relatively more complicated and can involve various growth mechanisms. Dislocation-driven growth is a popular mechanism in which the anisotropic nanowire growth is achieved by preferred deposition at the self-perpetuating spirals of axial dislocations.[44] Self-catalyzed growth is commonly found in compound semiconductor nanowires due to the different deposition rates of the various elements.[45]

There are many advantages these vapor deposition methods when compared to solution-based techniques. First, the high temperature, and sometimes high vacuum, conditions used provide high degrees of crystallinity. Additionally, it has been shown that the cooling rate can be slowed from those high temperatures to secure excellent optical quality as well.[46,47] Second, specific control of the location, composition, dimension, and organization of the nanowires can be achieved in vapor deposition processes by carefully designing the catalysts, growth sites on the substrates, and/or the precursors themselves.[48,49] Finally, due to the broad range of vapor deposition conditions (high temperature, inert environment,…), a multitude of material systems can be synthesized into the nanowire geometry.

While these advantages hold true for vapor-phase synthesis of nanowires, the same high temperatures that allow for excellent quality are also not cost effective nor scalable. Therefore, solution-phase techniques, which are run at much lower temperatures and provide more sample quantity, are more desirable for mass production on an industrial scale. These synthetic routes can rely on facet-specific stabilizers[50] or participate in the solid-liquid-solid mechanism[51,52] (analogous to VLS) to direct growth along a certain crystallographic direction.

1.2.b – Conversion Chemistry

Even with the combined spectrum of tools at the disposal of the previously described techniques, there are some material designs that are problematic to produce. For example, superlattice structures of various materials can be grown in the vapor phase,[53] but with limited success and repeatability. Conversion chemistry allows for the design of superlattice structures and more via a pseudo top-down approach. Fundamentally, conversion is just the result of overwhelming one material system with another element or elements to form the coexisting phase.

Consider the following example: A <100> Si nanowire (50 nm diameter, 1 μm in length) has Ni deposited at specific points along the length, as defined by electron beam lithography. The nanowire is then annealed such that Ni diffusion takes place, but only perpendicular to the nanowire axis.[54] With sufficient amount of Ni, the volume into where Ni diffuses is now a certain phase of $NiSi_x$.[55] And due to the lithographic patterning, the Si nanowire has become a $Si/NiSi_x$ superlattice nanowire.

This and other geometries are also available using conversion techniques. Potential for axial junctions parallel to the nanowire axis or compositionally-varying superlattice structures exist. This notion of site-specific material modification could become a power tool with the appropriate conditions using the concept of conversion chemistry.

1.3 – Nanowire Effects in Energy Conversion Applications

The nanostructures created by the various methods described above can exhibit unique properties useful in many applications, including energy conversion and production. Two specific energy related applications the work in this thesis most directly applies are thermoelectrics and fuels cells.

1.3.a – Thermoelectricity

The direct conversion of thermal energy to electrical power, or vice versa, is known as thermoelectricity. With a typical car engine wasting nearly 75% of its energy to exhaust heat,[56] water heating, and motor friction, the need for thermoelectric devices as thermal energy scavengers is obvious. An even more obvious picture is developed when considering energy production on a global scale. The world consumed 16.3 TW worth of power in 2012,[57] but large scale power plants only run at ~40-45% efficiency. Therefore, over 40 TW of power was produced to satisfy the demand. Much of that energy is lost to the system, not unlike a car

engine losing heat to the surroundings. If thermoelectric devices could convert that otherwise wasted heat into useable electrical power at 3% efficiency,[58] enough power would be produced to cover the demand of over 30 states for an entire year.[59]

The current problem in the thermoelectric community is that the heat to energy conversion in state of the art devices is nowhere close to 3% efficient. This is because the materials used in the devices do not have the necessary properties for efficient thermal conversion. The first and most important of these properties is the Seebeck Coefficient, which is the voltage developed under application of a temperature gradient ($S = V/\Delta T$). Good thermoelectric materials require this value to be at least $\pm$ 200 μV/K or greater in magnitude. The other properties include electrical resistivity and thermal conductivity, both of which are required to be as low as possible. Together, these properties combine to form the thermoelectric figure of merit, $z = S^2\sigma/k$, where S is the Seebeck coefficient, σ is the electrical conductivity, and k is the thermal conductivity. In order for thermoelectric devices to become economically viable, the product zT, where T is temperature, must be equal to or greater than 3.

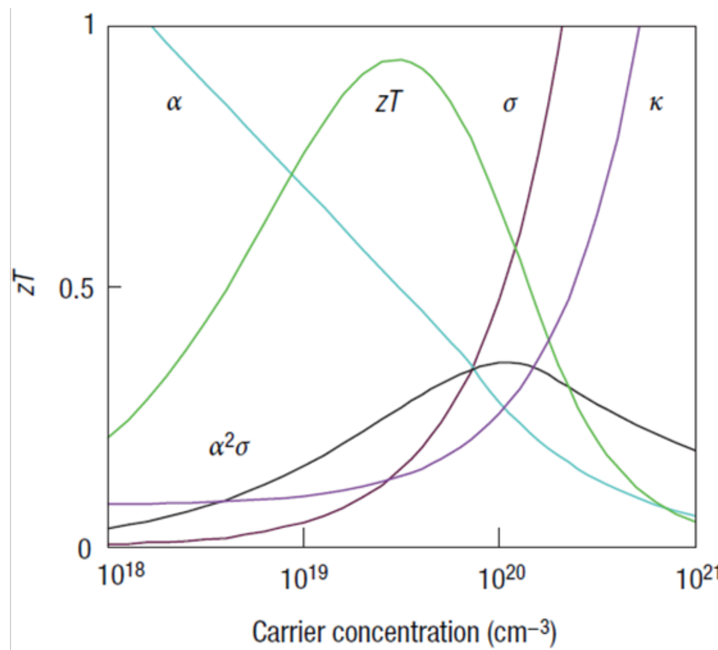

Figure 1.1 – Dependences of the Factors of zT on Carrier Concentration: This figure was adapted from reference 60.

What is currently limiting the zT in all systems are the interdependencies between the three factors that comprise it. The Seebeck, electrical conductivity, and thermal conductivity all have dependencies on the material carrier concentration, however, not in the same direction. Figure 1.1 depicts the various dependencies on the carrier concentration for BiTe.[60] From that graph, it is clear that the carrier concentration should be at the level of a degenerately doped semiconductor for optimized zT. The other electronic issue arises between the Seebeck and electrical conductivity in the form of carrier mobility. As the mobility increases, electrical

conductivity increases, but the Seebeck decreases, putting them directly at odds with one another.

The nanowire geometry can help alleviate these dependencies in two ways. First, the Seebeck is dependent on the slope of the density of state with respect to energy. Therefore, if the nanowire diameter is on the order of the exciton Bohr radius of the material, confinement to a 1-dimentional system leads to sharp features in the density of states (Figure 1.2),[61] thereby raising the Seebeck without affecting the electrical conductivity.[62] Second, and more practically, thermal conductivity is intrinsically limited in the nanowire geometry.[63,64] There are two components to the thermal conductivity, an electron component (depends on carrier concentration) and a lattice component (where thermal energy travels in quantized lattice vibrations called phonons). Due to the relatively long mean free path of phonons in single crystal semiconductors, boundary scattering at the nanowire surface limits phonon propagation, therein lowering the thermal conductivity without affecting either the Seebeck or electrical resistivity. Further work exhibiting enhancement in all factors of zT has yet to be demonstrated.

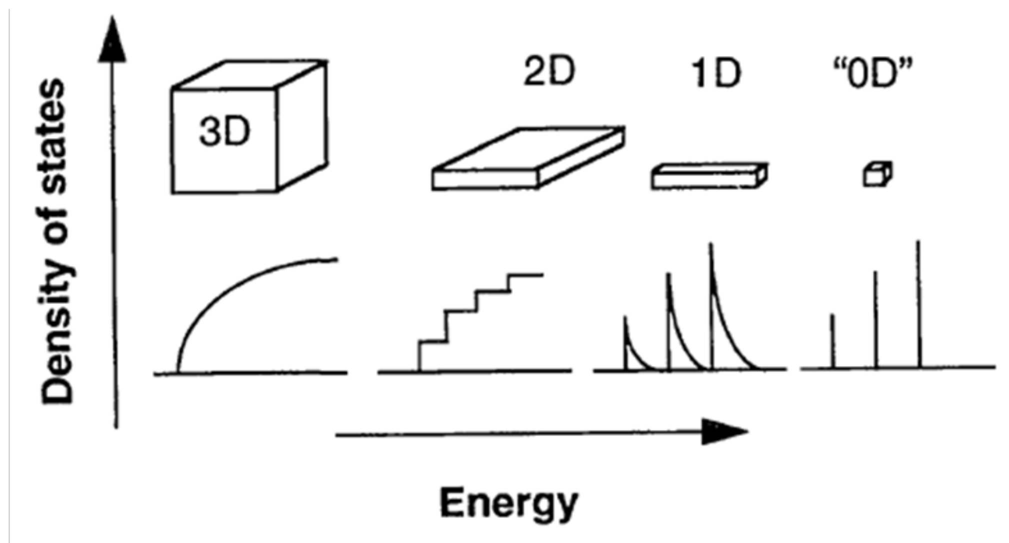

Figure 1.2 – Shape Dependent Density of States: Based on the dimensionality of confinement, the density of states as a function of energy will have various features. This figure was adapted from reference 61.

1.3.b – Solid-Oxide Fuel Cells

Research on fuel cell technologies has risen to high prominence due to growing concerns over greenhouse gas emissions. Fuel cells are electrochemical power generation devices, which can operate at higher efficiencies compared to combustion based power production.[65] They have a wide range of potential applications including both small and large scale stationary power applications. Solid oxide fuel cells (SOFCs) are all solid state systems that offer the most promise when it comes to commercialization. They consist of three main components: an electrolyte (which conducts oxide ions or protons), a cathode, and an anode.

They typically operate at elevated temperature (700-1000 ^oC) to ensure adequate ionic conduction in the electrolyte.[66,67] The high temperature operation has the disadvantages of maintaining sealing of the cells (particularly for temperatures >700 ^oC), the long-term stability of the individual materials, and compatibility between electrolyte and electrodes.[68,69] Therefore there has been huge interest in developing new material systems for low temperature operation.

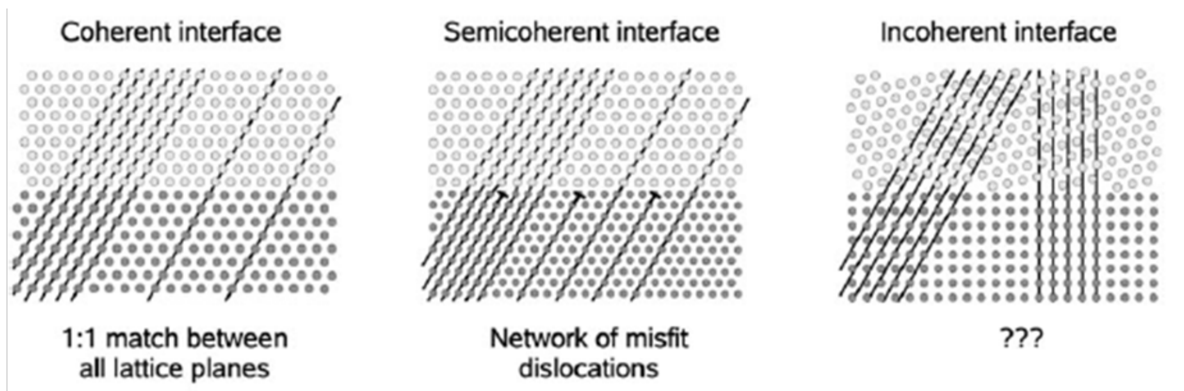

Figure 1.3 – Interface Coherence: Sketch representing a simplified dependence of the interface structure on the lattice mismatch between two materials. This figure was adapted from reference 72.

Nanostructured materials offer several key advantages and novelties that may produce a low temperature ionic conductor. They are characterized by short diffusion lengths, a high density of interfaces, and in some cases, where the interfaces are closely spaced, completely new properties are observed, as found for the transport properties of an artificial superlattice of CaF_2 and BaF_2.[70] In fact, if the density of interfaces is very high the interfacial effects may completely dominate, regardless of materials![71] These interfacial effects can be cause by space charge regions, strain, or yet unexplained phenomena, depending on the coherence on the interface between the two materials (Figure 1.3).[72] While this field is still in its infancy, it holds a great deal of promise to provide the world with a low temperature oxide ionic conductor.

1.4 – References

1. Yang, P., Yan, R. & Fardy, M. Semiconductor nanowire: What's next? *Nano letters* (2010).at <http://pubs.acs.org/doi/abs/10.1021/nl100665r>
2. Cui, Y., Wei, Q., Park, H. & Lieber, C. Nanowire nanosensors for highly sensitive and selective detection of biological and chemical species. *Science* **1289**, (2001).
3. Joyce, H. J. *et al.* III–V semiconductor nanowires for optoelectronic device applications. *Progress in Quantum Electronics* **35**, 23–75 (2011).

4. Boukai, A. I. *et al.* Silicon nanowires as efficient thermoelectric materials. *Nature* **451**, 168–171 (2008).
5. Duan, X., Huang, Y., Agarwal, R. & Lieber, C. Single-nanowire electrically driven lasers. *Nature* **421**, 241–245 (2003).
6. Andrews, S. C. *et al.* Atomic-level control of the thermoelectric properties in polytypoid nanowires. *Chemical Science* **2**, 706 (2011).
7. Hochbaum, A. I. *et al.* Enhanced thermoelectric performance of rough silicon nanowires. *Nature* **451**, 163–7 (2008).
8. Nika, D. L., Pokatilov, E. P., Askerov, a. S. & Balandin, a. a. Phonon Thermal Conduction in Graphene. *Materials Science* 43 (2008).at <http://arxiv.org/abs/0812.0518>
9. Heron, J., Fournier, T., Mingo, N. & Bourgeois, O. Mesoscopic size effects on the thermal conductance of silicon nanowire. *Nano letters* **9**, 1861–1865 (2009).
10. Yamada, Y. *et al.* Nanocrystal bilayer for tandem catalysis. *Nature chemistry* **3**, 372–6 (2011).
11. Cao, A., Lu, R. & Veser, G. Stabilizing metal nanoparticles for heterogeneous catalysis. *Physical chemistry chemical physics : PCCP* **12**, 13499–510 (2010).
12. Xu, Z., Xiao, F., Purnell, S. & Alexeev, O. Size-dependent catalytic activity of supported metal clusters. *Nature* **372**, (1994).
13. Sumathi, R. R. Bulk AlN single crystal growth on foreign substrate and preparation of free-standing native seeds. *CrystEngComm* **15**, 2232 (2013).
14. Avrutin, V., Silversmith, D. & Morkoç, H. Doping asymmetry problem in ZnO: current status and outlook. *Proceedings of the IEEE* (2010).at <http://ieeexplore.ieee.org/xpls/abs_all.jsp?arnumber=5462903>
15. Peng, K.-Q. & Lee, S.-T. Silicon nanowires for photovoltaic solar energy conversion. *Advanced materials* **23**, 198–215 (2011).
16. Oh, S. H. *et al.* Oscillatory mass transport in vapor-liquid-solid growth of sapphire nanowires. *Science* **330**, 489–93 (2010).
17. Fortuna, S. a & Li, X. Metal-catalyzed semiconductor nanowires: a review on the control of growth directions. *Semiconductor Science and Technology* **25**, 024005 (2010).
18. Fan, H. J. *et al.* Vapour-transport-deposition growth of ZnO nanostructures: switch between c -axial wires and a -axial belts by indium doping. *Nanotechnology* **17**, S231–S239 (2006).
19. Fang, X., Wu, L. & Hu, L. ZnS nanostructure arrays: a developing material star. *Advanced materials* **23**, 585–98 (2011).
20. Xu, T., Ji, P., He, M. & Li, J. Growth and Structure of Pure ZnO Micro/Nanocombs. *Journal of Nanomaterials* **2012**, 1–5 (2012).
21. Ozgur, U. *et al.* A comprehensive review of ZnO materials and devices. *Journal of Applied Physics* **98**, (2005).
22. Baxter, J. & Aydil, E. Epitaxial growth of ZnO nanowires on - and -plane sapphire. *Journal of Crystal Growth* **274**, 407–411 (2005).
23. Wen, C.-Y. *et al.* Formation of compositionally abrupt axial heterojunctions in silicon-germanium nanowires. *Science* **326**, 1247–50 (2009).
24. Lei, H., Chen, J. & Ruterana, P. Role of c-screw dislocations on indium segregation in InGaN and InAlN alloys. *Applied Physics Letters* **96**, 161901 (2010).

25. Tsukazaki, A. *et al.* Repeated temperature modulation epitaxy for p-type doping and light-emitting diode based on ZnO. *Nature Materials* **4**, 42–46 (2004).
26. Thakur, J. S. *et al.* Investigation of E1(LO) phonon-plasmon coupled modes and critical points in In1−xGaxN thin films by optical reflectance measurements. *Applied Physics Letters* **96**, 181904 (2010).
27. Hahn, C. *et al.* Effect of Thermal Annealing in Ammonia on the Properties of InGaN Nanowires with Different Indium Concentrations. *The Journal of Physical Chemistry C* **117**, 3627–3634 (2013).
28. Kuykendall, T., Ulrich, P., Aloni, S. & Yang, P. Complete composition tunability of InGaN nanowires using a combinatorial approach. *Nature materials* **6**, 951–6 (2007).
29. Huang, M. H. *et al.* Room-temperature ultraviolet nanowire nanolasers. *Science (New York, N.Y.)* **292**, 1897–9 (2001).
30. Gargas, D. J., Toimil-Molares, M. E. & Yang, P. Imaging single ZnO vertical nanowire laser cavities using UV-laser scanning confocal microscopy. *Journal of the American Chemical Society* **131**, 2125–7 (2009).
31. Zhang, G., Zhang, Q., Bui, C.-T., Lo, G.-Q. & Li, B. Thermoelectric performance of silicon nanowires. *Applied Physics Letters* **94**, 213108 (2009).
32. Gargas, D. J., Gao, H., Wang, H. & Yang, P. High quantum efficiency of band-edge emission from ZnO nanowires. *Nano letters* **11**, 3792–6 (2011).
33. Kumari, L. *et al.* Controlled Hydrothermal Synthesis of Zirconium Oxide Nanostructures and Their Optical Properties. *Crystal Growth & Design* **9**, 3874–3880 (2009).
34. Yogamalar, N. R. & Chandra Bose, a. Burstein–Moss shift and room temperature near-band-edge luminescence in lithium-doped zinc oxide. *Applied Physics A* **103**, 33–42 (2011).
35. Chang, P. & Lu, J. ZnO nanowire field-effect transistors. *IEEE Transactions on Electron Devices* **55**, 2977–2987 (2008).
36. Look, D. C., Claflin, B. & Smith, H. E. Origin of conductive surface layer in annealed ZnO. *Applied Physics Letters* **92**, 122108 (2008).
37. Yang, X., Xu, C. & Giles, N. Intrinsic electron mobilities in CdSe, CdS, ZnO, and ZnS and their use in analysis of temperature-dependent Hall measurements. *Journal of Applied Physics* **104**, 073727 (2008).
38. Janotti, A. & Van de Walle, C. G. Fundamentals of zinc oxide as a semiconductor. *Reports on Progress in Physics* **72**, 126501 (2009).
39. Liu, X., Giordano, C. & Antonietti, M. A molten-salt route for synthesis of Si and Ge nanoparticles: chemical reduction of oxides by electrons solvated in salt melt. *Journal of Materials Chemistry* **22**, 5454 (2012).
40. Janotti, A. & Van de Walle, C. G. Native point defects in ZnO. *Physical Review B* **76**, 1–22 (2007).
41. Ruankham, P., Sagawa, T., Sakaguchi, H. & Yoshikawa, S. Vertically aligned ZnO nanorods doped with lithium for polymer solar cells: defect related photovoltaic properties. *Journal of Materials Chemistry* **21**, 9710 (2011).
42. Xiong, Q. *et al.* Semiconductor Nanowires and Nanotubes: From Fundamentals to Diverse Applications. *Journal of Nanotechnology* **2012**, 1–2 (2012).

43. Kodambaka, S., Tersoff, J., Reuter, M. C. & Ross, F. M. Diameter-Independent Kinetics in the Vapor-Liquid-Solid Growth of Si Nanowires. *Physical Review Letters* **96**, 096105 (2006).
44. Bierman, M. J., Lau, Y. K. A., Kvit, A. V, Schmitt, A. L. & Jin, S. Dislocation-driven nanowire growth and Eshelby twist. *Science* **320**, 1060–3 (2008).
45. Morin, S. a, Bierman, M. J., Tong, J. & Jin, S. Mechanism and kinetics of spontaneous nanotube growth driven by screw dislocations. *Science* **328**, 476–80 (2010).
46. Wu, J. Z., Yun, S. H., Dibos, a., Kim, D.-K. & Tidrow, M. Fabrication and characterization of boron-related nanowires. *Microelectronics Journal* **34**, 463–470 (2003).
47. Wang, S. & Yang, S. Growth behaviour of straight crystalline copper sulphide nanowires. *Advanced Materials for Optics and …* **45**, 39–45 (2000).
48. Yu, Q. *et al.* Control and characterization of individual grains and grain boundaries in graphene grown by chemical vapour deposition. *Nature materials* **10**, 443–9 (2011).
49. Huang, M. *et al.* Catalytic Growth of Zinc Oxide Nanowires by Vapor Transport. *Advanced Materials* **13**, 113–116 (2001).
50. Chiu, C. *et al.* Platinum nanocrystals selectively shaped using facet-specific peptide sequences. *Nature chemistry* **3**, (2011).
51. Heitsch, A. T., Fanfair, D. D., Tuan, H.-Y. & Korgel, B. a Solution-liquid-solid (SLS) growth of silicon nanowires. *Journal of the American Chemical Society* **130**, 5436–7 (2008).
52. Chen, G. *et al.* Growth of In2O3 Nanowires Catalyzed by Cu via a Solid-Liquid-Solid Mechanism. *Nanoscale research letters* **5**, 898–903 (2010).
53. Li, D., Wu, Y., Fan, R., Yang, P. & Majumdar, A. Thermal conductivity of Si/SiGe superlattice nanowires. *Applied Physics Letters* **83**, 3186 (2003).
54. Léonard, F. & Talin, a A. Electrical contacts to one- and two-dimensional nanomaterials. *Nature nanotechnology* **6**, 773–83 (2011).
55. Foggiato, J., Yoo, W. S., Ouaknine, M., Murakami, T. & Fukada, T. Optimizing the formation of nickel silicide. *Materials Science and Engineering: B* **114-115**, 56–60 (2004).
56. Kumar, S., Heister, S. D., Xu, X., Salvador, J. R. & Meisner, G. P. Thermoelectric Generators for Automotive Waste Heat Recovery Systems Part II: Parametric Evaluation and Topological Studies. *Journal of Electronic Materials* **42**, 944–955 (2013).
57. BP Statistical Review of World Energy June 2012. (2012).
58. Majumdar, A. Thermoelectricity in semiconductor nanostructures. *Science* **303**, 777–778 (2004).
59. DOE Annual Energy Outlook 2012. (2012).
60. Snyder, G. J. & Toberer, E. S. Complex thermoelectric materials. *Nature Materials* **7**, 105–14 (2008).
61. Alivisatos, P. Semiconductor clusters, nanocrystals, and quantum dots. *Science* **271**, 933–937 (1996).
62. Hicks, L. & Dresselhaus, M. Thermoelectric figure of merit of a one-dimensional conductor. *Physical review B: Condensed matter* **47**, 631–634 (1993).
63. Donadio, D. & Galli, G. Atomistic simulations of heat transport in silicon nanowires. *Physical review letters* **102**, 195901 (2009).
64. Lu, X. Longitudinal thermal conductivity of radial nanowire heterostructures. *Journal of Applied Physics* **106**, 064305 (2009).

65. Tarancón, A. Strategies for Lowering Solid Oxide Fuel Cells Operating Temperature. *Energies* **2**, 1130–1150 (2009).
66. Menzler, N. H., Tietz, F., Uhlenbruck, S., Buchkremer, H. P. & Stöver, D. Materials and manufacturing technologies for solid oxide fuel cells. *Journal of Materials Science* **45**, 3109–3135 (2010).
67. Nesaraj, A. Recent developments in solid oxide fuel cell technology-a review. *Journal of Scientific & Industrial Research* **69**, 169–176 (2010).
68. Fabbri, E., Pergolesi, D. & Traversa, E. Materials challenges toward proton-conducting oxide fuel cells: a critical review. *Chemical Society reviews* **39**, 4355–69 (2010).
69. Tao, S. & Irvine, J. T. S. A redox-stable efficient anode for solid-oxide fuel cells. *Nature Materials* **2**, 320–3 (2003).
70. Kilner, J. Ionic conductors: Feel the strain. *Nature Materials* **7**, (2008).
71. Maier, J. Nanoionics: ionic charge carriers in small systems. *Physical Chemistry Chemical Physics* **11**, 3011–3022 (2009).
72. Fabbri, E., Pergolesi, D. & Traversa, E. Ionic conductivity in oxide heterostructures: the role of interfaces. *Science and Technology of Advanced Materials* **11**, 054503 (2010).

Chapter 2

ZnO-based Polytypoid Nanowires and their Thermoelectric Properties

2.1 - Introduction

The increasing environmental concerns associated with fossil fuel-based energy production have induced a wave of scientific research into affordable alternative energy sources that are both clean and renewable.[1] While efforts into green power generation continue in a variety of exciting and promising directions, one avenue that has caught the attention of the scientific community over the past decade is thermoelectrics, wherein electrical power is generated through the scavenging of waste heat. The efficiency of this conversion is related to the material-dependent figure of merit, $zT = S^2\sigma T/k$, where S, σ, T, and k represent the Seebeck coefficient, electrical conductivity, absolute temperature, and thermal conductivity, respectively. Though this has been a topic of scientific study for a number of decades, material engineering directed at maximizing zT has been complicated by the interdependencies of the previously mentioned parameters, limiting the efficiency.[2] Specifically, the Seebeck coefficient's inverse dependence on carrier concentration is at odds with the electrical conductivity's direct dependence. An additional problem is that electrons carry both charge and heat, causing a synchronous increase in the electrical and thermal conductivities with carrier concentration. While the interplay of these parameters has limited zT of bulk materials to ~1 at 300 K, theoretical studies pioneered by Hicks and Dresselhaus predict that it is possible to increase zT by using low dimensional materials, for example, nanowires.[3] The enhancement can be attributed to two factors: electronic band structure changes (increasing the Seebeck coefficient) and enhanced interface phonon scattering (reducing the lattice thermal conductivity), both of which are described in more detail in Chapter 1 of this thesis.[4] Experimentally, both enhancements have been shown separately in certain nanostructured materials.[5–10]

Due to its natural conduction pathway and intrinsically phonon-limiting structure, the nanowire geometry possesses great promise to be used in next generation thermoelectric devices. However, in order to achieve 1-dimentional confinement necessary to observe electronic band-related enhancements in the Seebeck coefficient, the diameter of the nanowires must be on the order or smaller than the exciton Bohr radius of the comprising material. For example, if nanowires of PbSe, with a bulk exciton Bohr radius of ~47 nm,[11] could

be made with diameters less than 40 nm, confinement effects should begin to appear. In fact such nanowires have been made, but due to uncontrollable concentration of carriers and strong surface state effects, the effect of quantization on the Seebeck has not been observed.[12] As for ZnO, with a bulk exciton Bohr radius of 2.34 nm,[13] nanowires of such small dimensions would be robust enough for neither accurate measurements nor actual implementation in an energy scavenging device.

This chapter contains material from the following publication: [Andrews, S. C. *et al. Chemical Science* **2**, 706 (2011)] - Reproduced by permission of The Royal Society of Chemistry http://pubs.rsc.org/en/Content/ArticleLanding/2011/SC/c0sc00537a

2.1.a - Better Nanowire Designs for Thermoelectric Transport

Instead of pursuing traditional 1-dimentional confinement by limiting the nanowire diameter, nanosized inclusions created along the length of the nanowire could serve a similar function. If nanostructuring can have distances close to the exciton Bohr radius, pseudo 2-dimentional confinement may be able to positively affect the Seebeck response while not affecting electrical conduction. In fact, if the defects used to create such nanostructuring can also act as either donors or acceptors, then the electrical conductivity may actually increase. Apart from the proposed effects on the electrical properties, introducing features on the nanometer length scale will only further reduce the transport of thermal energy. While it is true that the nanowire diameter limits long wavelength phonons from even existing, the modes with the highest thermal energy per phonon occur at the nanometer scale. For example, the dominant phonon wavelength in Si is ~2.3 nm;[14] therefore, the suppression of thermal transport was found to be greatest when surface roughness approached that length scale.[10] With these combined effects, nanostructuring along the nanowire could show enhancement in all 3 factors of zT.

2.1.b - Indium-Ga-ZnO Alloys

As a means of creating nanosized features within a nanowire, one needs to look no further than Indium-ZnO system. Early work in the literature discovered that ZnO mixed with high amounts of In formed a superlattice-like structure with formula $In_2O_3(ZnO)_n$, where *n* is the number of ZnO layers sandwiched between single atomic sheets of octahedrally-coordinated In, with formula InO^{2-}.[15] These single atomic sheets of In lie in the (002) plane of the ZnO wurzite matrix, and can form in nearly perfect periodicity.[16] Additional work also found that the superlattice-forming materials could be generalized to $In_2O_3(ZnO)_n$, where M is In, Ga, Fe, and/or other trivalent metals.[17,18]

Furthermore, these materials have shown excellent transport behavior, even while being made by various methods. Nomura, et al. created crystalline $InGaO_3(ZnO)_5$ via pulsed laser deposition (PLD) which exhibited field-effect mobilities up to 80 $cm^2\ V^{-1}\ s^{-1}$ while maintaining excellent transparency.[19] While at the time the authors proposed this performance

was largely due to the highly crystalline product created from their PLD process, they later discovered that the amorphous material Indium-Galium-ZnO (a-IGZO, no stoichiometric relation known) also exhibited admirable transistor characteristics, with carrier concentrations and mobilities ranging from 10^{17}-10^{20} cm^{-3} and 3-11 cm^2 V^{-1} s^{-1}, respectively.[20] These findings have spurned a flurry of research on this material, as it is now being used in electronic displays.[21–26]

As for thermoelectric applications, one can first evaluate the zT of the matrix ZnO. While ZnO can itself already exhibit relatively high electrical conductivity due to the formation of intrinsic donor defects, such as oxygen vacancies and zinc interstitials, the introduction of Al, In, and/or Ga can further increase the conductivity when substituted for Zn.[27–29] Previous reports have shown zT of Al-doped ZnO to be as high as .02 at 300K, with the main increase over pure ZnO being from the increase in electrical conductivity.[30] However, in this case, the thermal conductivity was still limiting overall performance (35 W m^{-1} k^{-1}). By combining Ga and Al, further increases can be achieved, but with overall zT still limited to < .04 at 300K.[31,32]

While further efficiency gains were expected to be observed in the $In_2O_3(ZnO)_n$ system, Ohta et al. measured the zT to be ~ 0.01 at 500 K.[33] In this case, the thermal conductivity was lowered from that of pure ZnO, but both the electrical conductivity and Seebeck coefficient were lowered considerably. While this was not an expected result, two items must be mentioned: first, the material was not single crystalline, giving way for misinterpretation of the observed phenomena to the intrinsic material, rather than the present grain boundaries. Second, the materials measured contained, on average, more superlattice-type structures, meaning that they obtained the thermodynamic product from their synthetic technique. This distinction between kinetic versus thermodynamic products will be address in more detail later in this thesis.

It should be noted that IGZO nanowires have before been synthesized via gas-phase methods, such as chemical vapor deposition.[34–38] These nanowires typically result in perfect to near perfect superlattice structure, which can be considered a stoichiometric, or thermodynamic, product. However, what these reports show in periodicity, they lack in control, with variations of n values, phase, and yield. Such variation is suitable for neither structure-transport relation studies nor eventual device integration.

This work demonstrates a novel method for the rational design and control of nanometer-sized features in the polytypoid $M_2O_3(ZnO)_n$ nanowire system and show an enhancement in zT for indium gallium zinc oxide (IGZO, $In_{2-x}Ga_xO_3(ZnO)_n$) nanowires as a result of these features. Furthermore, the first simultaneous improvement in the Seebeck coefficient, electrical conductivity, and thermal resistivity for a nanowire system was measured.

2.2 - Synthesis of Polytypoid IXZO (X= Ga, Fe) Nanowires via Solid-State Conversion

In contrast to direct synthesis of IZO and IGZO nanowires via chemical vapor deposition, a 3-step solid-state diffusion process shown schematically in Figure 2.1 was used. This facile

design allows for a high level of control in manipulating material composition, structure, and properties.

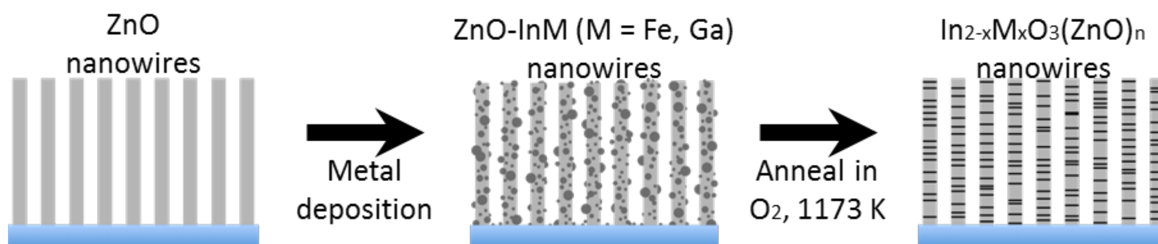

Figure 2.1 - Schematic of Facile Diffusion Scheme to Created Alloyed Nanowires

First, ZnO nanowires were grown on double-polished a-plane (110) sapphire substrates by a Au-catalyzed CVT process.[39] Sapphire substrates were diced into 2 mm x 2 mm pieces and thoroughly clean by sonication in acetone for 1 hour. A thin layer of Au (~1-5 nm) was sputtered onto the substrates and the substrates were annealed in air at 1223 K for 1 min to melt the Au thin film, causing it to bead up into small Au nanoparticles. ZnO and C (1:1 ratio by weight) powders were mixed using a motor and pestle and loaded into a small alumina boat. One Au coated sapphire substrate was placed on the downstream end of the boat on top of the ZnO/C precursor. The boat was inserted 4 cm inside a 0.5-inch diameter quartz tube and this tube was placed inside a 1-inch diameter quartz tube. The tubes were loaded into a tube furnace such that the front of the alumina boat was downstream from the center of the furnace. The tube was purged with a flow of 10% O_2 /Ar and Ar. The furnace was rapidly heated to 1173 K and kept there for a growth time of 15 min. Typical nanowires had diameters of 80-130 nm and lengths of 10-15 µm and grew along the [001] direction.

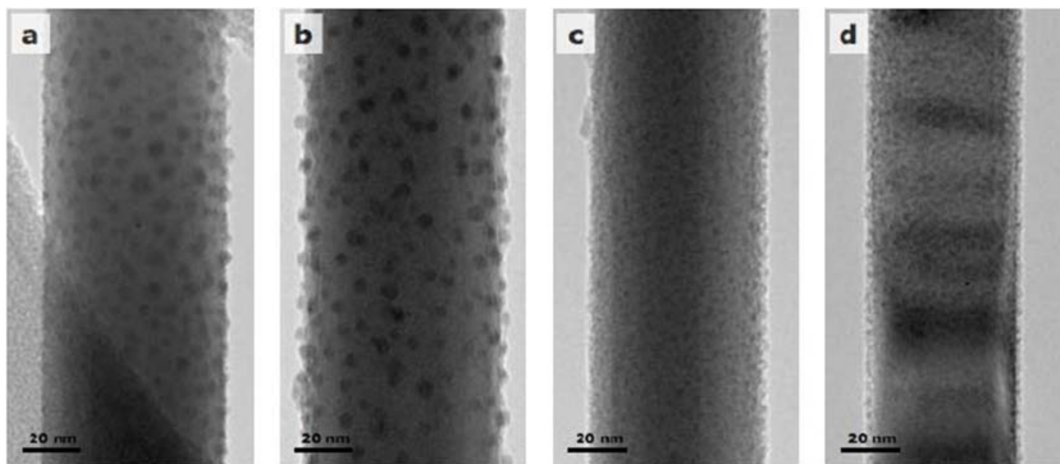

Figure 2.2 – Metal Coated Nanowires (after step 2 from previous figure): ZnO nanowires coated with (a) 5 nm of In and 5 nm of Ga, (b) 10 nm of In, (c) 10 nm of Ga, and (d) 5 nm of In and 5 nm Fe

Next, a home-built thermal evaporation system was used to deposit varying amounts of In, Ga, and Fe metals as measured by the film thickness of evaporated metal incident on a quartz crystal monitor. By monitoring the thickness of the deposited metal it was possible to

generate reproducible alloy concentrations and control metal ratios in mixed depositions (Figure 2.2).

Lastly, the metal-coated ZnO nanowire substrates were loaded into the center of a 1-inch diameter quartz tube and heated in a tube furnace under an O_2 atmosphere at 1173 K for 12–96 h. The superlattice structure remained no matter how long the nanowires were annealed, indicating that the structure is thermally stable. For metal loadings greater than 20 nm, samples were prepared using successive coating/annealing cycles, with no loss to the nanowire morphology or crystallinity (Figure 2.3). This method was used to synthesize IZO, IGZO, and IFZO nanowires.

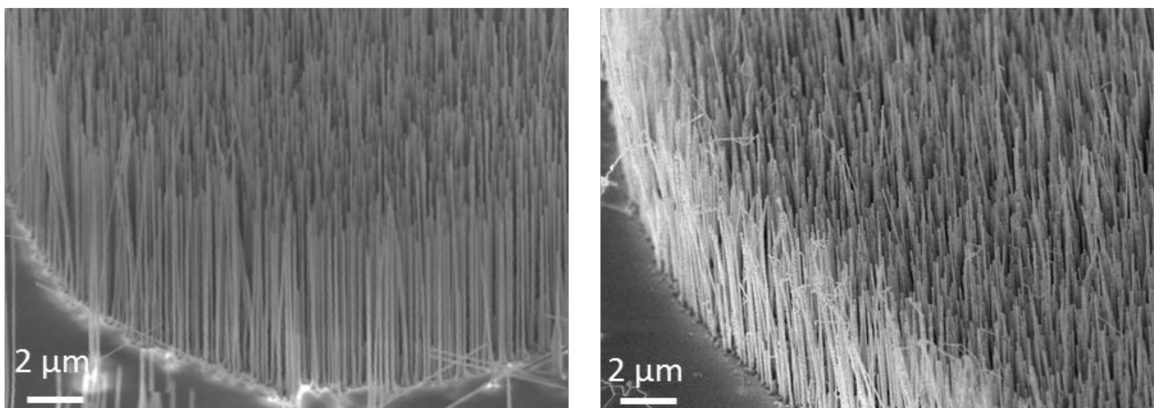

Figure 2.3 – Before and After Conversion: (a) Vertically aligned ZnO nanowires grown on sapphire. (b) After deposition and annealing, the nanowires lose neither orientation nor morphology

Note that for the remainder of this thesis, samples will be referred to by the thickness of the metal coating, rather than a specific chemical formula (for example, 20/20 IGZO refers to 20 nm of In and 20 nm of Ga deposited). This designation is more meaningful than a chemical formula largely due to the fact that the natural distribution of nanowire diameters and relatively low concentrations of metal deposited combine to give non-stoichiometric, or kinetic, products. Presumably, if heated to higher temperatures for longer amounts of time, the relatively low amounts of metal would be able to find their equilibrium structure in a single nanowire of a specific diameter and length. These products would be more in line with bulk and CVT-made nanowires containing periodic structuring and very well could be the focus of further transport studies.

2.3 - Structure Determination of IXZO (X = Ga, Fe) Nanowires

2.3.a - XRD, EDS, and CTEM

Figure 2.4 shows the XRD patterns of IGZO nanowires with different amounts of metal deposited. The pure ZnO sample shows peaks corresponding to the wurzite phase, along with a few peaks attributed to the Au catalyst and Al_2O_3 substrate used to grow the ZnO nanowires. Upon addition of In and Ga, and subsequent annealing, the peaks for the wurzite phase ZnO remain intact. However, there is a little shift from the position of the ZnO nanowire diffraction peaks, but peak broadening towards smaller angles is also observed, suggesting the formation of non-uniform alloys. The strong 002 peak in both patterns of IGZO indicate that the nanowire arrays in each case have maintained a vertical orientation after the conversion and no In_2O_3 or Ga_2O_3 peaks were observed in the IGZO samples. New peaks appear in the low-angle region (<10°) for the 40/40 IGZO sample, corresponding to spacings of 0.86 and 1.12, which are in good agreement with the predicted lattice constants for $M_2O_3(ZnO)_n$ with n = 1 and n = 2 (as mark in the figure). Additional higher-order peaks for n =1 and n = 2 are observed in the 15- 32° range.

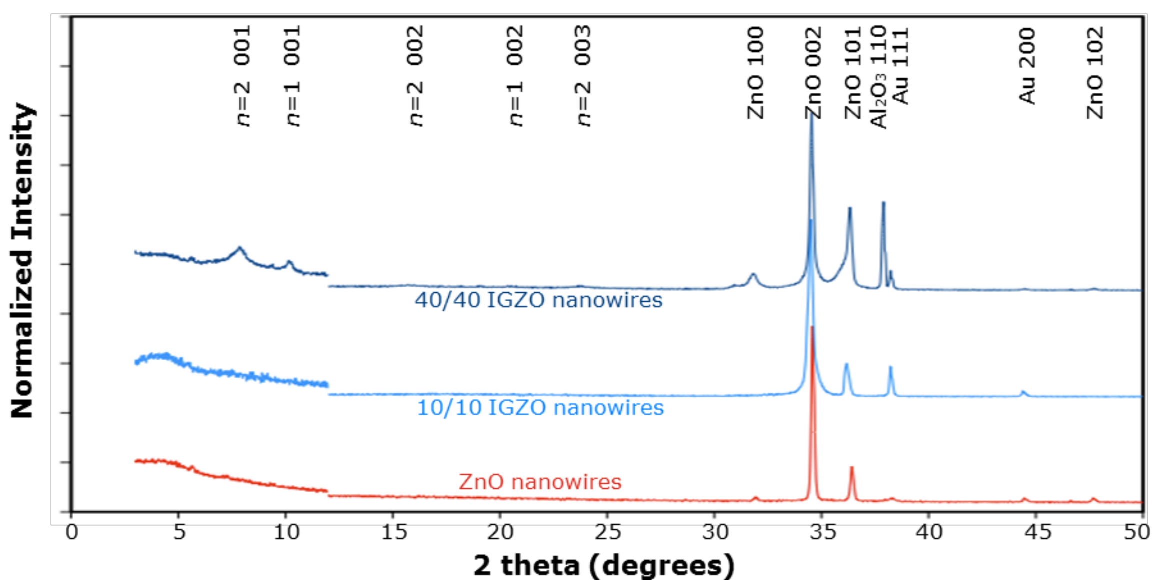

Figure 2.4 – X-Ray Diffraction: XRD patterns of ZnO nanowires (bottom) and IGZO nanowires prepared with 10/10 (middle) and 40/40 (top) of In and Ga metal deposition. Longer acquisition times were needed below 12° for better signal to noise and thus were normalized separately.

CTEM image of 10/10 IGZO nanowires (Figure 2.5) show a change in contrast perpendicular to the nanowire axis and repeating along the length due to the single In sheets.

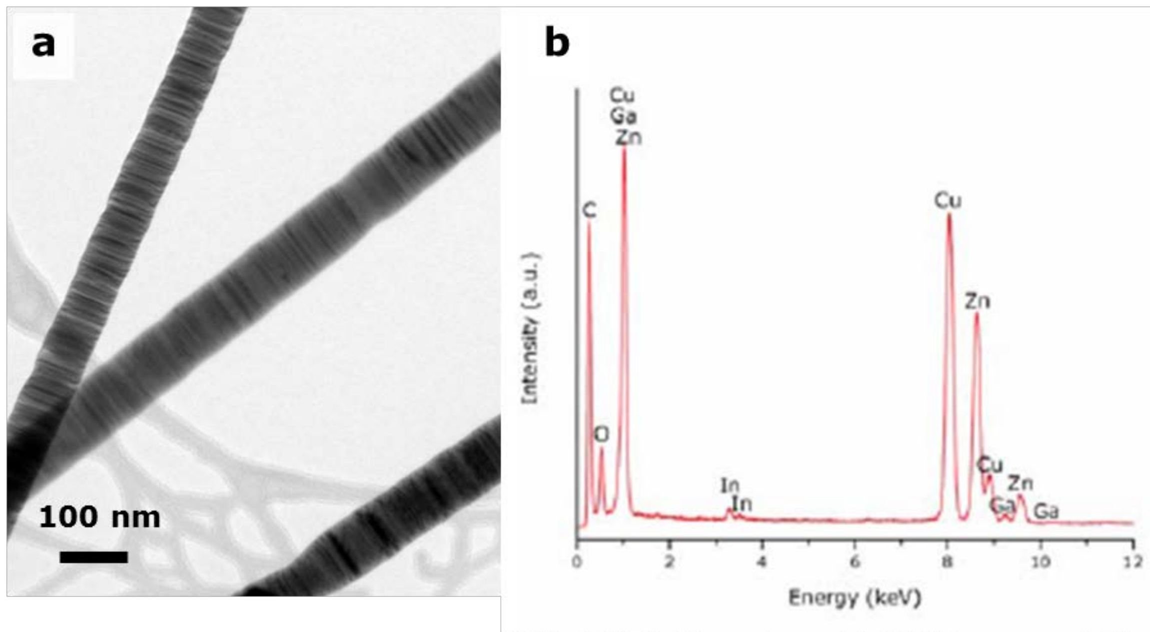

Figure 2.5 – Conventional TEM and EDS of IGZO Nanowires: (a) TEM images and (b) EDS spectrum of IGZO nanowires prepared by coating ZnO nanowires with 10 nm of In and 10 nm of Ga and annealing at 900 °C in oxygen for 12 hours. The In:Ga ratios were approximately 1:1 by EDS in all the nanowires.

The large-area EDAX spectrum for that specific IGZO sample shows a small amount of In and Ga, but their respective locations within the structure of the nanowire were not able to be obtained with this method. Measurements on IFZO (Figure 2.6) show similar structural features but also exhibit a lower inclusion density on average.

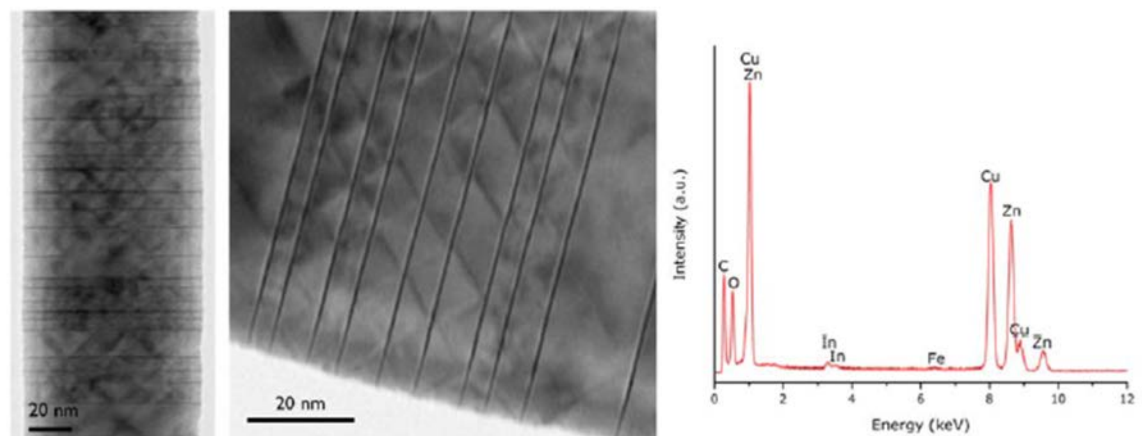

Figure 2.6 – Conventional TEM and EDS of IFZO Nanowires: (a) TEM images and (b) EDS spectrum of IFZO nanowires prepared by coating ZnO nanowires with 5 nm of In and 5 nm of Fe and annealing at 900 °C in oxygen for 12 hours.

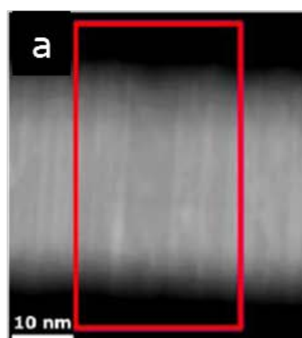

Figure 2.7 – Elemental Mapping of IGZO Nanowires: (a) Darkfield STEM image of a IGZO nanowire. The region within the rectangle was elementally mapped by EDS for (b) In, (c) Ga, (d) Zn, and (e) O.

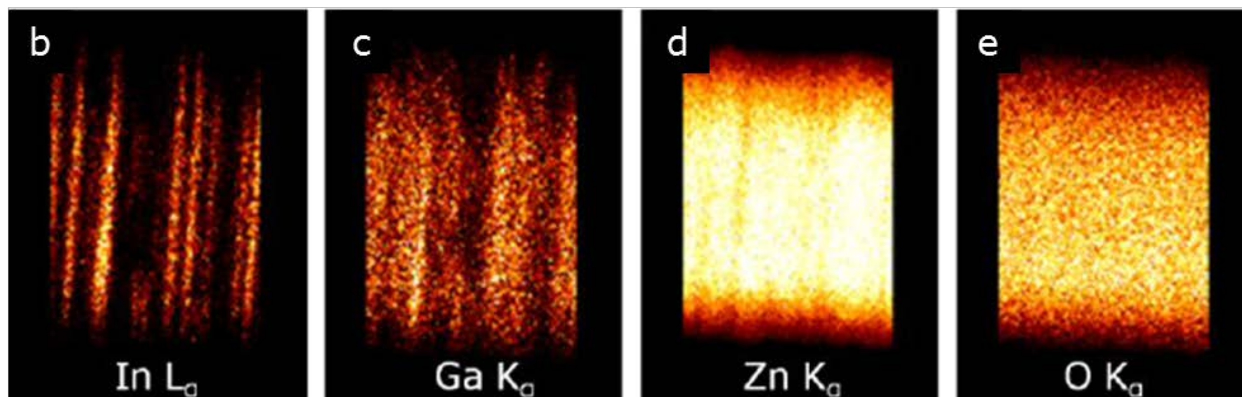

To obtain a clearer picture of where the various metals lie within the ZnO matrix, STEM mode EDS mapping was conducted (Figure 2.7). The elemental maps show a concentration of In within the octahedral inclusions. The Ga is more evenly spread across the nanowire. As expected, the Zn map shows a lack of Zn in the octahedral inclusions and the O is evenly spread around the nanowire.

2.3.b - Control of Inclusion Spacing and Density

Since the In was confirmed to be segregated into the perpendicular inclusions of the IGZO nanowires, Z-contrast electron beam imaging was utilized as a means to identify elemental positions based on image contrast. Briefly, High Angle Annular Dark Field Scanning Transmission Electron Microscopy (HAADF-STEM) is an imaging technique that utilizes large-angle scattering, which are mostly due to atomic interactions with the electron beam (Figure 2.8). Thus, for sufficiently large enough angles, elemental contrast in such images is proportional to ~ Z^2. Such contrast is typically referred to as Z-contrast, and will be used thusly. For the case of the IZO system and its constitutes, the difference between In (Z = 49) and Zn (Z = 30) alloys for unambiguous determination between the two elements. However, the difference between Ga and Zn is too small and cannot be distinguished from each other using this method (ΔZ = 1).

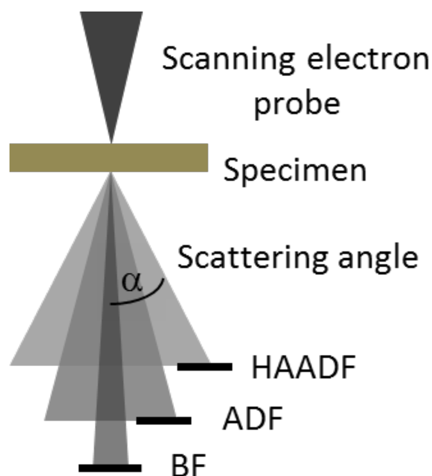

Figure 2.8 – Schematic of the Various STEM Detectors: (Above specimen) Conical electron beam focused into a nano-probe. (Below Specimen) Different interactions with the specimen cause the electrons to be scattered by angle α away from the primary beam axis. Smaller angled scattering results from weak interactions. Much of the contrast in BF STEM is due to diffraction and strain effects. Large angled scattering results from much stronger interactions with the nuclei , allowing for contrast relating to atomic number.

However, one must be careful when using such a tool, since misinterpretation of contrast is a common error. For example, if the HAADF detector is placed at too shallow of an angle, relatively large contributions from other types of scattering can and will contribute to the overall signal generated, clouding the interpretation of the collected image. This can be avoided by taking a series of images with various detector lengths (various collection angles) and comparing the relative contrast changes image to image. With this in mind, it is imperative to know how to operate electron microscopes properly, but especially when it comes to issues of STEM detector placement.

Figure 2.9 is a Z-contrast image of an IGZO nanowire clearly showing the presence of In-enriched layers (brightest lines) oriented perpendicular to the [002] direction. The slight increase in brightness toward the center of the nanowire is from an increased amount of non-atomic scattering from the change in thickness. Even at the smallest detector distances, thickness-dependent contrast cannot be voided. Therefore, any claims to the purity of the atomic species present in the layers cannot be made except for samples with uniform thickness.

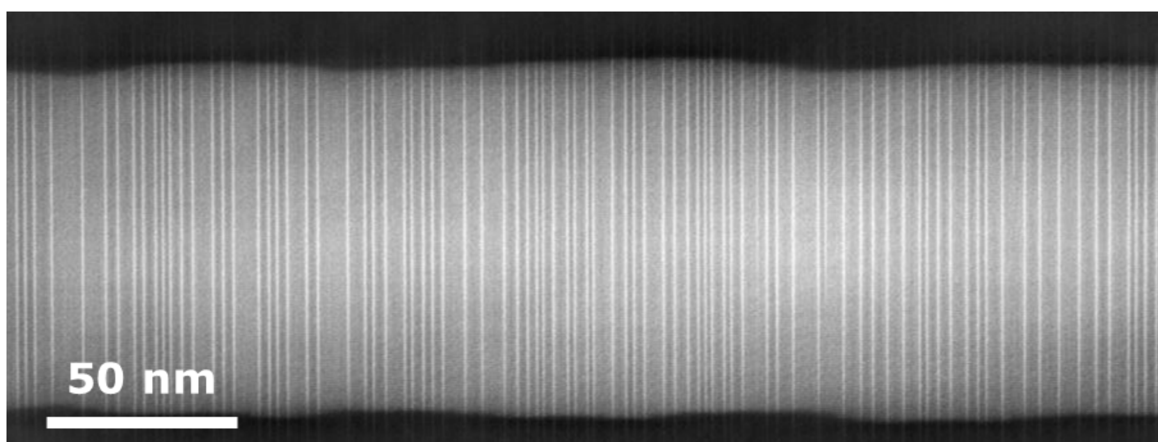

Figure 2.9 – HADDF STEM Image of IGZO Nanowire: Z-contrast is clearly obtained with this microscopy technique, as the In-rich inclusion layers show up as brighter lines than the ZnO matrix within which they are housed.

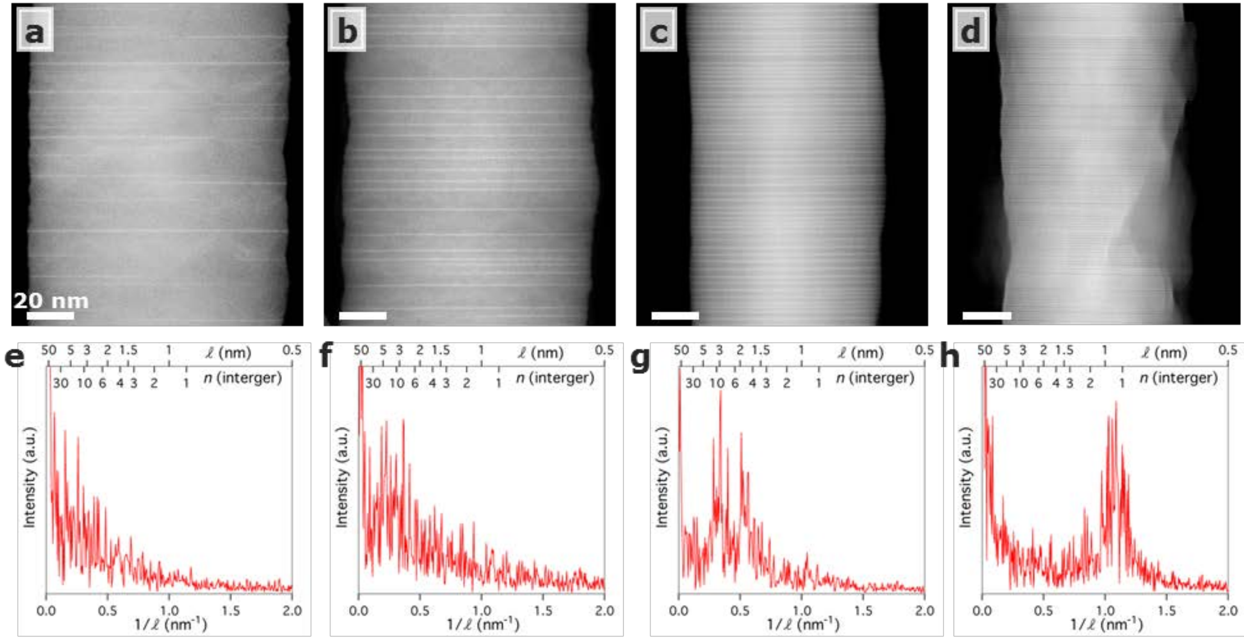

Figure 2.10 – Spacing Control: (a-d) Z-contrast STEM images of IGZO nanowires prepared with 10, 20, 40, and 80 nm of total metal (1:1 of In:Ga by film thickness, respectively. (e-h) Power spectra generated using line intensity profiles drawn along the length of the nanowires showing the frequency of reciprocal distance between InO_2^- layers for (a-d).

The amount of metal deposition was varied to determine its effect on inclusion layer density (Figure 2.10). As the metal amount increased, the inclusion density also increased, as expected. The surface of the 40/40 IGZO nanowire shown in Figure 10d appears rough due to the presence of oxide particles left over after the solid-state diffusion process. However, most IGZO nanowires in the sample did not show surface particles. Line intensity profiles drawn along the nanowire axis were used to generate power spectra (Figure 10 e-h) from the nanowires shown in Figure 10 a-d. The power spectra show the most common frequencies ($1/\ell$) within the nanowires, providing information regarding the InO_2^- layer spacings and the periodicity of the spacings. As the thickness of metal deposition is increased the most common frequencies shift to higher $1/\ell$ (smaller ℓ) indicating that the distance between layers decreases with increased metal deposition. The periodicity also increases with metal deposition, which can be seen in the emergence of distinct peaks, such as in Figure 10g. As seen in Figure 10h, the majority of inclusion layers in the 40/40 IGZO are separated by 2 or 3 layers of ZnO, which is supported by the low-angle XRD pattern Figure 4. It is evident from these power spectra that both *n* and the periodicity can be controllably tuned by adjusting the amount of metal deposition. However, it should be noted that his parameters are coupled, wherein low *n* values necessitate high degrees of periodicity.

2.3.c - InO_2^- Plane Inclusion Structure

The effect these In inclusions have on the bonding and structure of the IGZO nanowires was investigated via Z-Contrast imaging using the transmission electron aberration-corrected

microscope (TEAM) 0.5 operated at 300 KV. This microscope consists of a modified FEI Titan 80-300 microscope equipped with a special high-brightness Schottky-field emission electron source, gun monochromator, and two CEOS hexapole-type spherical aberration correctors, all of which enable 50 pm resolution.

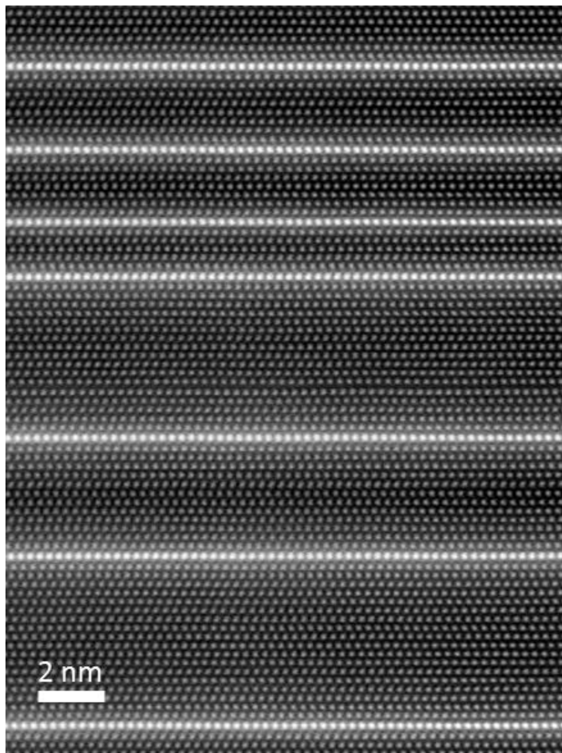

Figure 2.11 – High Resolution Z-contrast Image of IGZO Nanowire: Aberration corrected image that shows individual InO_2^- layers sandwiched between multiple $MZn_nO_{(n+1)}^+$ layers

Figure 2.11 is a high resolution Z-contrast image of an IGZO nanowire oriented along the [10-10] zone axis. It is clear from an image of this resolution that the In atoms sit in individual planes and are separated by wurtzite $MZn_nO_{(n+1)}^+$ slabs of varying thickness. While intensity analysis would have been able to prove definitively that these single atomic layers consist of only In atoms, the exact thickness of the sample must either be known to a precise level or assume the same thickness in the field of view of the image. Neither of these criteria were ever met in the HR images.

Upon examination of the HR-STEM images, two features at the inclusion are noticed. First, the inclusion layer is associated with a stacking fault, which produces an ABAB**A**CACA stacking sequence in which the wurtzite lattice on one side of the In/Ga layer is translated by ⅓<100> (Figure 2.12a). The location of the octahedral InO_2^- within the stacking sequence is denoted by the bold **A**.

Second, by taking an intensity line profile across the inclusion/matrix interface, the d spacing in the ZnO matrix was found to be unchanged from (002) of pure ZnO (0.26 nm), in excellent agreement with the XRD (Figure 2.12b). However, the distance from the In inclusion layer to nearest neighboring Zn layer measures to be 17% larger ($.30_7$). This expansion is due to the octahedral bonding structure of the In in the inclusion plane and is associated with a large amount of lattice strain.

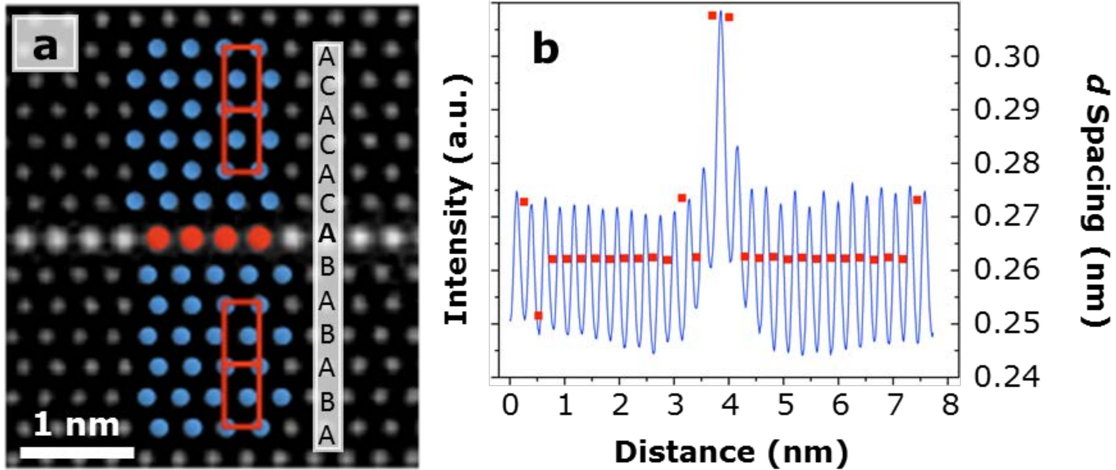

Figure 2.12 – Stacking Fault and Expansion: (a) Aberration corrected HRTEM image highlighting the change in stacking sequence across a InO_2^- layer. (b) Intensity profile and d spacing across a InO_2^- layer. On either side of the inclusion, the d spacing shows an expansion of ~17% to that of pure ZnO.

To further examine the bonding at the interface of the inclusion layer, the oxygen positions were observed via an annular dark field (ADF) detector (reference Figure 8), which is more sensitive to scattering of lighter elements, through the contrast is no longer directly relatable directly to Z^2.

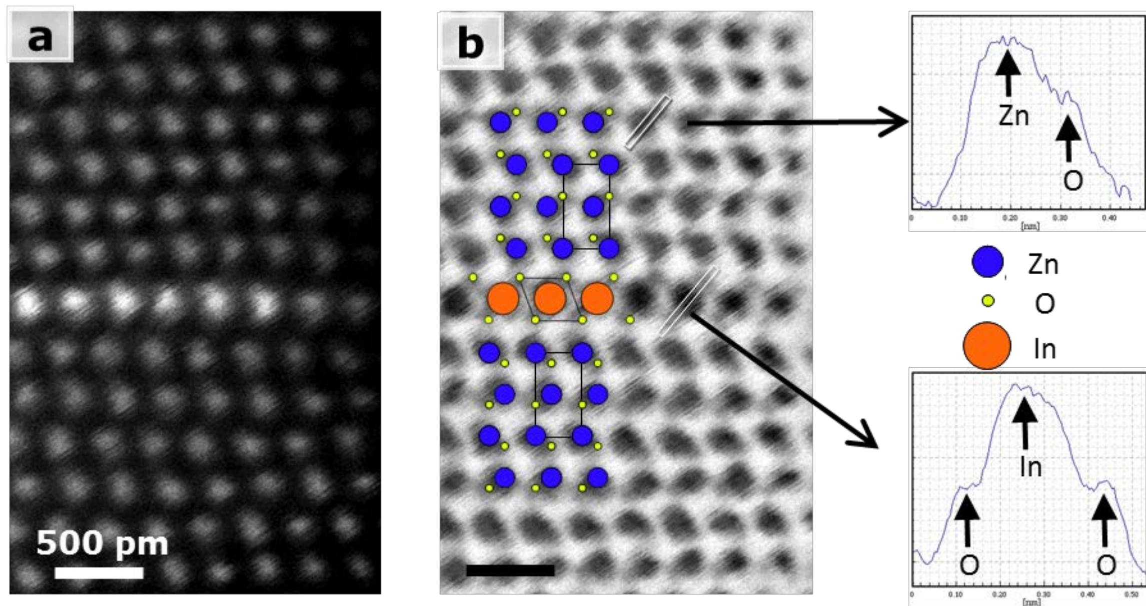

Figure 2.13 – HAADF vs ADF, Looking for Oxygen: (a) Aberration corrected HAADF image around a InO_2^- layer. No oxygen is observed. (b) Annular Dark Field image revealing the position of oxygen within the ZnO matrix. (Right side,) Intensity plots of lines drawn across both Zn (Top) and In (Bottom) atoms show oxygen more accurately.

Figure 2.13a and 2.13b are HAADF and ADF images taken of the same area at the same time. From Figure 11b, slightly darkened shoulders next to the Zn and In positions are oxygen. It's BEAUTIFUL. The positions of oxygen next to the Zn sites indicate the direction or polarity of the wurtzite tetrahedra. Above the In inclusion plane, the direction is face-up (oxygen pointing up). However, the tetrahedra on the other side of the inclusion are facing the opposite direction. Therefore, not only does the In inclusion layer have an associated stacking fault, but it also acts as an inversion domain boundary. This is due to the oxygen atoms on either side of the octahedrally coordinated In participating in bonding with the neighboring Zn.

2.3.d - Zig-Zag Structure and Model

With the existence of inversion domain boundaries clearly existing within the IGZO structure, it begs the question: how does the polarity switch before reaching the next inclusion layer? It remains possible that for very small *n* values (Figure 2.14), the bonding within the ZnO matrix can accommodate the strain felt by the neighboring inclusion layers. However, for *n* values large enough to exhibit conventional wurtzite bonding (Figure 2.11), there must be a second IDB in the ZnO matrix to restore the orientation of the tetrahedra between two basal inclusions. Additionally, because the charge balance of the crystal is disturbed by the MO_2^- composition of the basal layer, there must be extra M^{3+} ion substitutions to balance the overall charge. Further complexity is presented by the balance between the two alloying metals in IFZO and IGZO. There are a number of competing structural models that attempt to identify the second IDB, as well as the location of the additional M^{3+}, none of which can account for all the experimental observations.

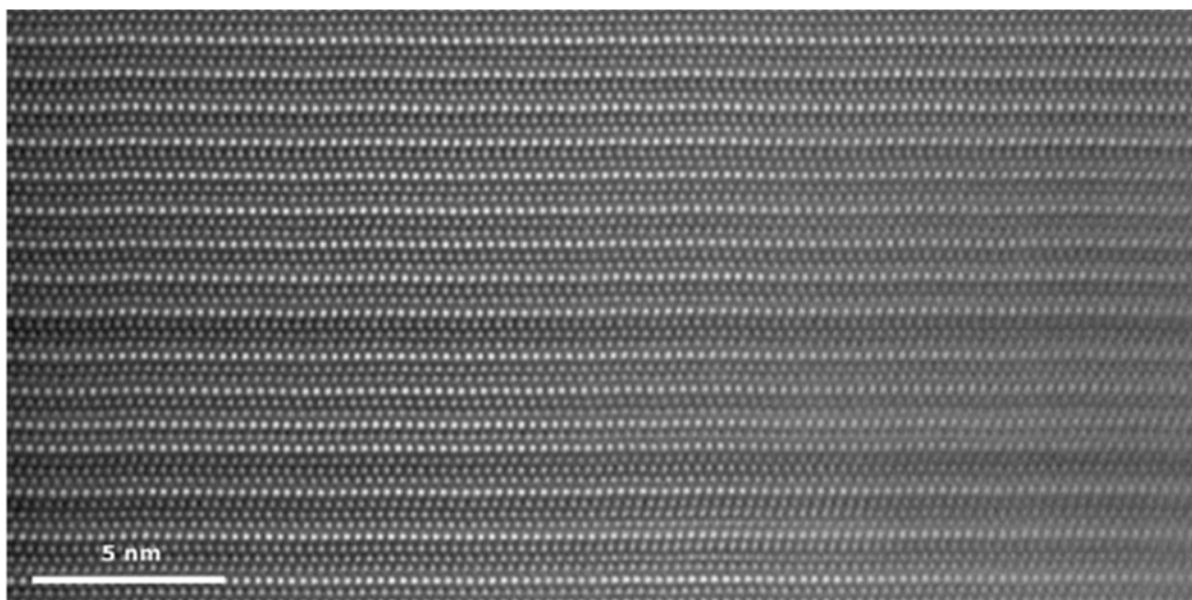

Figure 2.14 – 40/40 IGZO: Z-Contrast STEM image showing a high density of inclusion layers with spacing corresponding to n = 2 and n = 1.

Prior TEM studies of IZO and IFZO revealed a modulated "zigzag" layer in the ZnO slab.[18,40] Li et al. suggested that the center of mass in the wurtzite tetrahedra gradually shifts,

yielding a trigonal bipyramidal layer in the center of the slab (Figure 2.15a).[41] Here, zigzag contrast is supposedly caused by substitution of M^{3+} for Zn^{2+}, which form {1-212} planes that are sharply visible along the [10-10] zone axis. Hörlin et al. claimed that the zigzag for IFZO is a {1-214} plane, based on its incident angle with the basal plane by TEM. They also found that the indium resides predominantly in the basal inclusions, while iron is located mainly in the wurtzite slabs.[18]

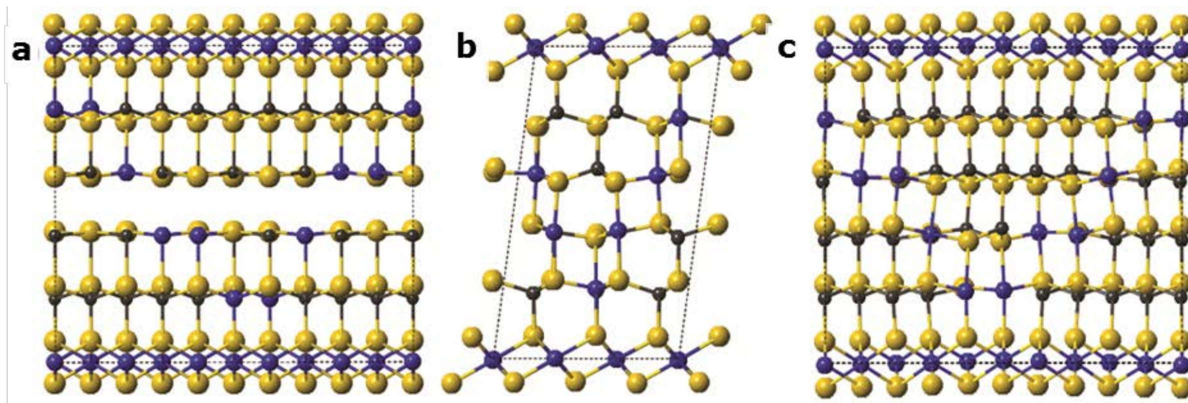

Figure 2.15 – Zig-Zag models: Zigzags in the model proposed by Li et al. are shown (a) along the [10-10] zone axis, with oxygen (yellow), zinc (gray), and indium (blue) atoms. The Yan model (b) is viewed along the [11-20] zone axis. Our proposed structure (c) is more favorable than any alternative model tested. Selected oxygen atoms have been hidden for clarity.

More recently, drawing on DFT calculations, Yan et al.[42] and Da Silva et al.[43] suggested that the IZO zigzags are composed of trigonal bipyramidal indium atoms that serve as the second IDB (Figure 2.15b). The indium layer is placed on the {10 $\bar{1}$1} plane, where it would be sharply viewable along [11-20], contrary to experimental reports.[18,40,41,44–46] Recent calculations using density functional theory (DFT) concluded that the model of Yan et al. has a similar formation energy to that of Li et al.[47]

The model proposed here from HRSTEM images and theoretical simulations resolves the structure of IZO and IFZO. Density functional theory (DFT) within the generalized gradient approximation (PBE)[48] was used to optimize atomic positions and compute total energies of several IZO and IFZO systems. For all calculations, VASP package[49] and projector augmented-wave potentials[50] were used. Electrons taken to be valence were In $5s^24d^{10}5p^1$, Fe $3p^64s^23d^6$, Zn $4s^23d^{10}$, and O $2s^22p^4$. A plane-wave cutoff of 500 eV was used throughout. In systems with iron, Fe 3d states were treated with an effective Hubbard term $U_{eff} = U - J = 3$, 4 or 6 eV.[51,52] Due to the rapid increase in computational expense with unit cell size, calculations were limited to $In_2O_3(ZnO)_3$ and $InFeO_3(ZnO)_3$. The structure in Figure 2.15c (110 atoms) is treated with a 5x2x2 k-point mesh, with k-points for other unit cells scaled accordingly. The structure model developed here is general to IGZO as well, albeit with some specific differences which may occur from the different size of Ga.

The nanowire growth direction is the c-axis of wurtzite; therefore, nanowires dispersed on TEM grids were all close to either the [11-20] or the [10-10] zone axis, the latter of which is distinguishable by its rectangular pattern of metal atoms. Because the [10-10] zone axis is 30° around the c-axis from the nearest member of the [11-20] family, it is rare to find a nanowire

that allows access to both zone axes within the limited range of the double tilt stage (≤20° for both α and β). The nanowire segment shown in Figure 2.16 allowed such a rotation, and thus we could observe the same feature from two directions. This segment contains a pair of edge dislocations that point along the [10-10] direction, as evidenced by the extra half-plane of Zn atoms at the termination of each basal inclusion. Figure 2.16a shows zigzag contrast both above and below basal inclusions, where none is visible in Figure 2.16b on the [11-20] zone axis. Note that no atomic resolution of an edge-on zig-zag is observed. Rather, a distribution of bright contrast across a region of 5-10 atoms, approximately 0.5-1 nm, is observed.

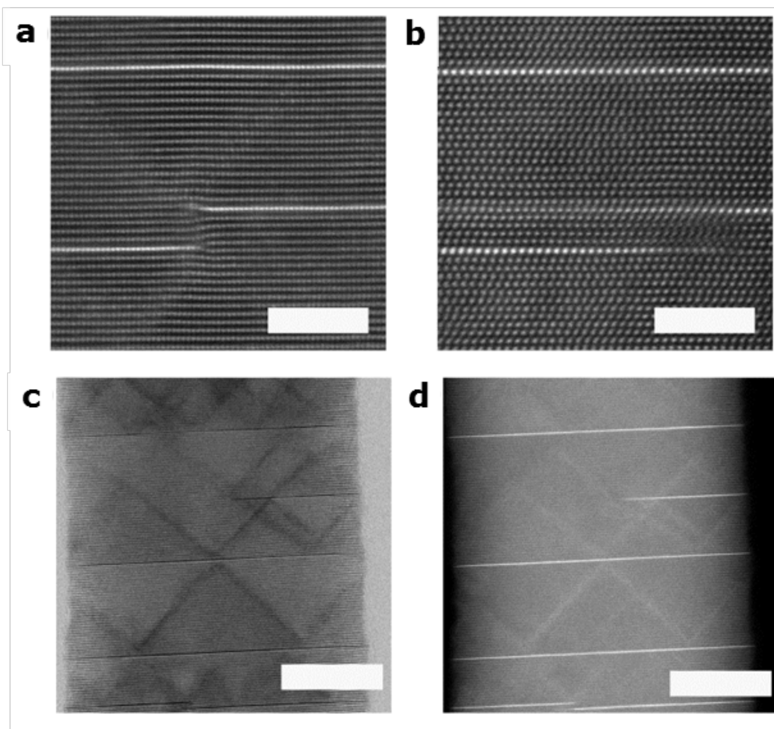

Figure 2.16 – Partial Inclusions in IFZO Nanowiress: Two basal inclusions meet in the body of an IFZO nanowire, as imaged along the (a) [11-20] and (b) [10-10] zone axes (scale bar is 2 nm). Another nanowire segment of IFZO was imaged simultaneously along [10-10] using (c) bright field and (d) high-angle annular dark field detection (scale bar is 8 nm).

Because there are three symmetrically equivalent zone axes in the [10-10] family, this zigzag in Figure 2.16a could be attached to a defect that is 60° rotated from the zone axis. If we assume that the zigzag is bounded by a linear edge orthogonal to the diffusion front, then we can predict the relationship between the true zigzag angle and the apparent angle. The formula for this calculation is the following: $\tan\theta_o/\cos\alpha = \tan\theta_a$, where θ_o is the true zigzag angle, α is the rotation around the c axis from the edge dislocation, and θ_a is the apparent angle. For an ℓ=4 zigzag rotated 60° around the c axis, $\theta_a = 58°$.

IFZO nanowires were imaged simultaneously by bright field and dark field STEM (Figure 2.16c-d), and contrary to the model of Li et al., the images demonstrate that the second IDB lies along the zigzag itself. The contrast in both images overlaps perfectly, where the dark contrast in bright field shows that the zigzags are regions of strain (as expected for an IDB) while the bright contrast in dark field indicates that these same areas are also indium rich. The dual nature of the zigzag as an IDB and site of indium substitution is also shown by DFT calculations of $In_2O_3(ZnO)_3$. For simplicity, the zigzags are depicted as a well-defined atomic plane, thus enabling relative comparisons of different single-plane structures. Using the starting geometry of a c-plane IDB in the center of the slab, as in the model of Li et al., the relaxed atomic

positions place the IDB along the zigzag itself, by making the indium atoms 5-fold coordinated (Figure 2.15c). The most stable structure of the type proposed here has a total energy per formula unit that is 18 meV lower than that proposed by Yan et al. and Da Silva et al.

Table 2.1 – DFT Calculated Energies: Structural energy per formula unit from our DFT calculations, describing two crystal compositions over a range of zigzag angles (θ). Energies are reported relative to the most stable zigzag angle for a given composition.

ℓ	θ	$In_2O_3(ZnO)_3$	$InFeO_3(ZnO)_3$ (U=4)
2	58.0°	38 meV	202 meV
3	46.8°	0 meV	31 meV
4	38.7°	18 meV	0 meV
5	32.6°	54 meV	—
6	28.1°	83 meV	—

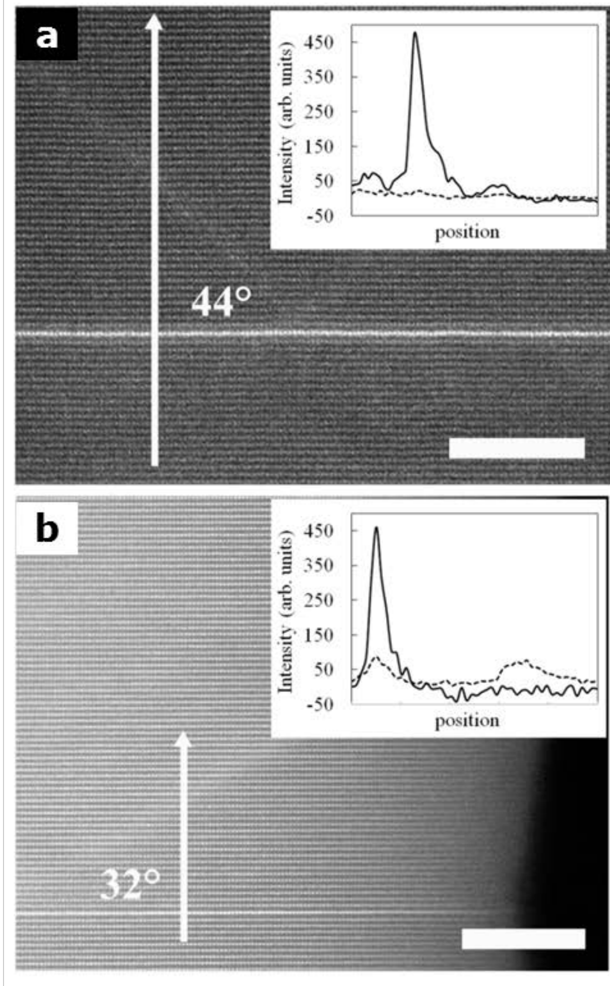

Figure 2.17 – Angle Dependent on Composition: EELS line scans were performed across two areas of an IFZO nanowire, and the integrated peaks of In (solid line) and Fe (dashed line) are plotted in the inset. The zigzag in (a) has a higher incident angle on the basal plane, and shows In in both inclusions and no peak for Fe, while the zigzag in (b) has a lower incident angle and a higher ratio of Fe:In. Scale bar is 5 nm

To assign crystallographic notation to a zigzag plane, we note that it must contain the [10-10] vector, so it can be written as {1-21ℓ}, where 1/ℓ is the fractional intersection of the plane with the *c* axis. The angle formed between (0002) and (1-21ℓ) is: $\theta = \tan^{-1}[(2/\ell) \cdot (c/a)]$. Using the *c/a* ratio of 1.6 for ZnO, the expected angles for a given ℓ value are listed in Table 2.1. The measured zigzag angles for IZO are in the range of 49-59°, so we assign them ℓ=2-3. We find that the zigzag angle depends on the metal composition. A range of 31-48° is observed for samples that contained various proportions of indium and iron, yielding L values of 3-5 for IFZO. DFT total energy calculations of $In_2O_3(ZnO)_3$ and $InFeO_3(ZnO)_3$ confirm this trend (Table 2.1). In IZO, the most stable computed structure corresponds to ℓ=3 9 (Figure 2.15c). Calculations of IFZO systems are limited in size to ℓ≤4, due to the added computational expense of spin polarization. Three different values of the effective Hubbard term U_{eff} were applied (3, 4, and 6 eV) with no qualitative change in the results. For all zigzag angles, antiferromagnetic ordering of Fe spins was more stable than ferromagnetic ordering (not shown), in agreement

with past literature.[18] We find that in IFZO, the most stable zigzag angle corresponds to $\ell \geq 4$ and is shallower than that of IZO, in agreement with experiment.

EELS data on IFZO further illustrate the dependence of the zigzag angle on the metal composition. Local quantities of iron and indium oxide on the nanowire surface determine the availability of each metal to diffuse and the resulting composition of the inclusions in IFZO, as expressed by the chemical formula $In_{2-x}Fe_xO_3(ZnO)_n$. To identify the relative proportion of In and Fe within either the basal or zigzag layers, EELS line scans were performed across both types of inclusions. In Figure 2.17a, a line scan shows a small Fe concentration across an entire region of IFZO, while the In peak has a sharp increase at the basal inclusion and a small rise at the zigzag. This indicates that the x value for this nanowire segment is low (<1), and indium is the majority M^{3+} ion.

Analysis of another nanowire segment (Figure 2.17b) shows that the Fe peaks across both types of inclusions are equally strong in this case, and there is no In peak observed in the zigzag. This segment of IFZO therefore has a higher x value than the one shown in Fig. 4a, and the angle of this inclusion pair is also noticeably lower (32° vs. 44°). The distribution of indium and iron between the zigzag and the basal inclusion is likely determined by the stability of the respective ions in those coordination environments. The In^{3+} ion is larger than Fe^{3+} (0.80 Å for 6-coordinate In^{3+} vs. 0.65 for high spin Fe^{3+})[53]. This contributes to the stability of indium in the octahedral site, making the zigzag the preferred site for iron when both species are present.

2.3.e - Formation Mechanism of Inclusion Layers

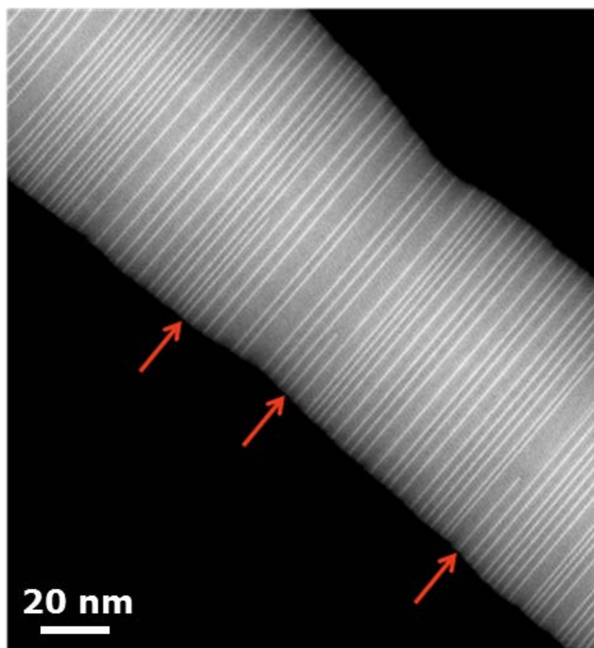

Figure 2.18 Diameter Fluctuations and Partial Octahedral Layers: HAADF STEM image of a 10/10 IGZO nanowire showing diameter fluctuations with inclusion density. The arrows indicate where some partial inclusions are located.

The ability to control the MO_2^- inclusion density is a direct result of the solid-state diffusion process by which the polytypoid nanowires are produced. The diffusion rates of In, Ga, and Zn within ZnO are extremely high at the 1173 K annealing temperature, with values of 6.62×10^{-12}, 1.09×10^{-14}, and 1.13×10^{-12} $cm^2\ s^{-1}$, respectively.[54] DFT calculations by various groups show that Zn atoms diffuse through ZnO using Zn vacancies.[55] Based on their activation energies for diffusion, In and Ga are also thought to diffuse through Zn vacancies, though some controversy exists regarding their true activation energies.[54,56,57] Since In and Ga are substitutional dopants, Zn atoms must diffuse out when the In and Ga atoms diffuse inward. The Zn atoms diffuse to the surface of the nanowire, leading to a modulation in the diameter (Figure 2.18). In areas of higher inclusion density, the

diameter of the nanowire is slightly thicker (more In and Ga diffused in, more Zn diffused out) compared to areas of lower inclusion density.

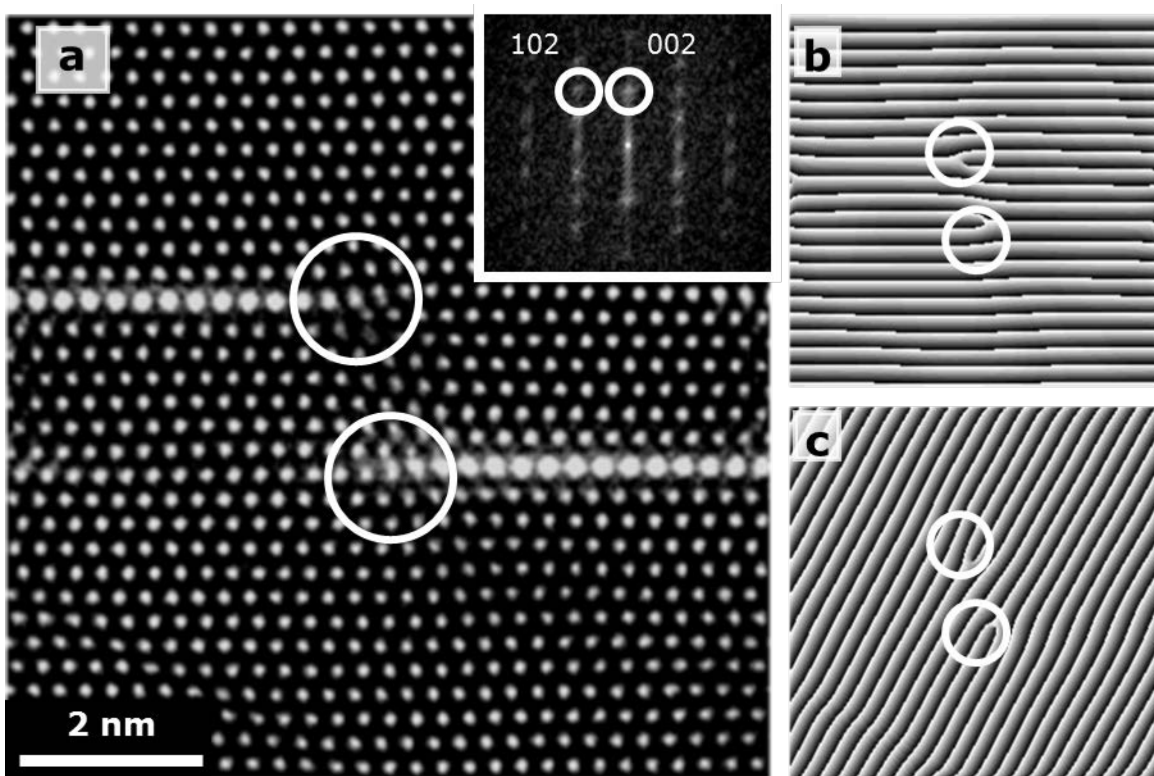

Figure 2.19 - HRSTEM of Partial Inclusions: (a) HAADF STEM image of IGZO on the [10-10] axis with two partial InO_2^- layers and the FFT (inset). Moire images taken along the (b) 002 and (c) 102 reflections clearly showing the presence of edge dislocations at the end of each incomplete layer.

Once the In and Ga initially diffuse into the nanowire from the surface, they strain the wurtzite lattice of the pure ZnO, deforming the structure, and eventually relaxing the strain by creating octahedral inclusions and trigonal bipyramidal layers. Defects such as edge dislocations, stacking faults, and inversion domain boundaries are known to attract impurities and can assist in the formation of impurity inclusions.[58] In some of the nanowires synthesized in this study, especially those made with lower amounts of In and Ga, partial In inclusions were observed (Figure 2.18). The ends of these partial inclusions are usually associated with edge dislocations with the dislocation line lying at the leading edge of the InO_2^- plane.[59] Edge dislocations can be seen in Figure 2.19a in the HRSTEM image of two partial inclusions. Moire images taken along the 002 and 102 reflections clearly show the presence of the edge dislocations (Figure 2.19b-c). Another interesting observation is that the partial inclusions are always connected to one surface of the nanowire (Figure 2.18), indicating that the growth of the inclusion starts at the surface and proceeds across the diameter of the nanowire until it either reaches the opposite side.

If the inclusions are growing through a defect-assisted process and the inclusion formation begins at the nanowire surface, then the edge dislocation must somehow nucleate

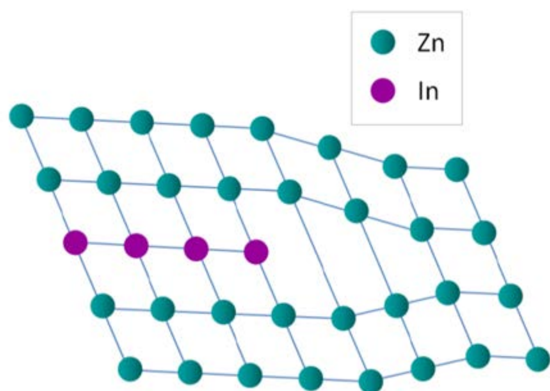

Figure 2.20 - Defect-assisted Inclusion Propagation: Schematic depicting the edge dislocation and associated expanded lattice which facilitates growth of the InO_2^- octahedral inclusions

near the surface. One possible scenario is that the edge dislocations are formed on the nanowire surface via heterogeneous nucleation, which occurs with the help of defects such as impurity atoms. Since In has a larger ionic radius compared to Zn, the dissolution of In within the wurtzite lattice will create strain. The presence of dislocations within the lattice can relax some of this strain if the In atoms diffuse towards the dislocations and eventually occupy those lattice positions below the edge dislocations where the lattice is already expanded (Figure 2.20). The edge dislocation basically creates a ‘‘hole’’ in which the larger In atoms can sit. Due to the high diffusion rate of In within the ZnO lattice, the In atoms can rapidly concentrate at the sites of edge dislocations. Since the In atoms have a mutual attraction they can crystallize into another phase (octahedrally coordinated InO_2^-) which will flow in one direction towards the dislocation. The growth of the inclusion will continue along the dislocation until the concentration of In within the lattice decreases to the point at which local equilibrium is reached. In the lower concentration samples, more partial inclusions can be observed, likely resulting from insufficient quantities of In atoms necessary to complete the inclusions. As a note, no partial inclusions were observed in the 40/40 IGZO.

2.4 - Thermoelectric Transport in IGZO Nanowires

The presence of the InO_2^- inclusions alters both the thermal and electrical properties in the converted polytypoid nanowires. While ZnO can exhibit a relatively high intrinsic electrical conductivity due to formation of oxygen vacancies acting as donor states, the introduction of slight amounts of Al, In, or Ga can further increase the conductivity when substituted for Zn.[60] Considering all the $M_2O_3(ZnO)_n$ nanowires synthesized in this work, the high inclusion density and significant dopant level present in the IGZO nanowires makes them the ideal candidate for thermoelectric enhancement, and thus, IGZO nanowires were used for all transport studies.

Devices for electrical measurements were fabricated on p^{++} Si chips with 200 nm of dry thermal oxide coating the surface. Nanowires were then either placed into specific areas on the chips via micromanipulation or randomly dispersed by dry transfer. Standard photolithography was used to define electrodes on the nanowires for a top contacting scheme (inset of Figure 2.22). Ti/Au was used at the metal contact to ZnO, while Zn/Ti/Au was used for the IGZO. The later required ~2nm of Zn to elicit Ohmic behavior. All devices required rapid thermal annealing

(450 °C in Ar, 60 s) to achieve linear IV curves. Details on the Seebeck Coefficient measurement can be found elsewhere.[12]

2.4.a - Electrical Conduction

The increased electrical conductivity observed at room temperature in the IGZO nanowires when compared to the ZnO nanowires is consistent with that of a slightly doped semiconductor (Figure 2.21). However, considering the relatively large amount of In and Ga incorporation (greater than 2% atomic of each metal atom from EDS), the observed increase in conductivity is smaller than the metallic-like value of conduction that is expected. While the In and Ga impurities can act as electrical dopants in ZnO when substituted for tetrahedrally-coordinated Zn, In and Ga also sit in the trigonal bipyramidal sites, helping to preserve electroneutrality and reducing the number of generated carriers. Moreover, the InO_2^- inclusions can act as barriers to oxygen diffusion leading to decreased conductivity by suppressing the formation of oxygen vacancies.[19] Interestingly, the linear temperature-dependent resistance of IGZO, as seen in Figure 2.21, is not typical behavior for a slightly doped semiconductor (of which pure ZnO nanowires are an example) nor of a degenerately doped semiconductor (which should give metallic behavior). This deviation from the classical semiconducting behavior indicates a departure from the traditional thermally-activated mechanism. The octahedral layers could be acting as potential barriers to electron diffusion, leading to alternative transport mechanisms such as pseudo variable-range hopping or percolation conduction.[61]

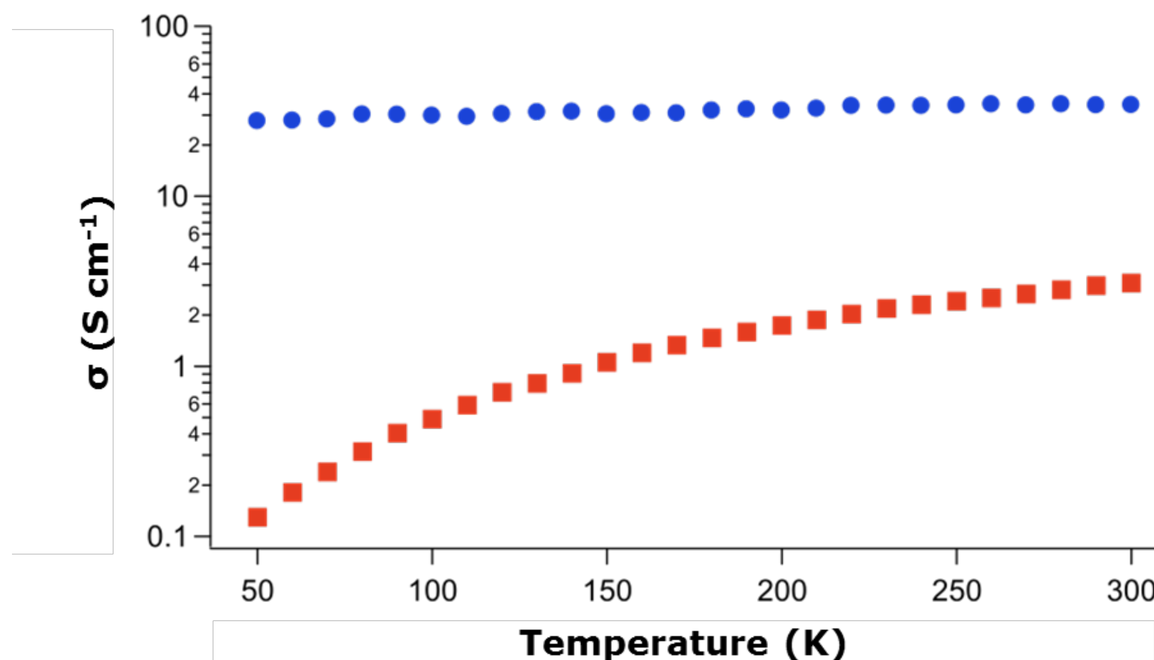

Figure 2.21 - Electrical Conductivity as function of Temperature: Single nanowire electrical response for a 120 nm diameter 5/5 IGZO nanowire (blue circles) and a 110 nm diameter ZnO nanowire (red squares).

2.4.b - Seebeck Coefficient

This non-typical transport presumably caused by the presence of the In inclusions is also evident in the Seebeck voltage acquired as a function of temperature in Figure 2.22. At 300 K, the Seebeck coefficient grew in magnitude from -188 μV K^{-1} in ZnO nanowires to -402 μV K^{-1} in IGZO nanowires. Similar Seebeck values were observed in each of the many ZnO and IGZO nanowire samples measured, respectively. The observed increase in Seebeck coefficient may be an effect of the potential barriers, which could act as low-energy electron filters.[62] When a temperature gradient is applied, charges diffuse to states of lower chemical potential. While most of these states are on the colder side, unoccupied states on the hotter side allow for charge diffusion in the opposing direction, thereby limiting the overall potential that can develop for a given temperature gradient. Charges that participate in back diffusion are referred to as ‘‘cold electrons’’ (for n-type semiconductors) since they possess lower carrier energy. However, potential barriers with appropriate energy levels can act as low energy charge filters by preferentially affecting their mobility.[63] By limiting the amount of back diffusion, a larger potential can develop, resulting in an increased Seebeck coefficient.

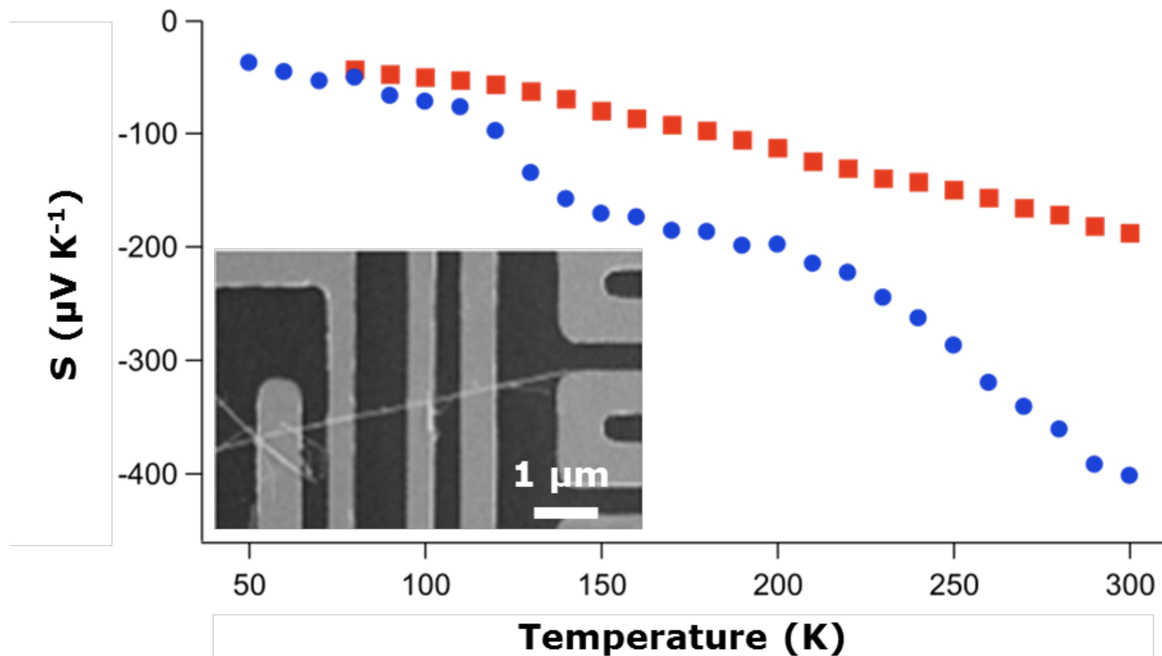

Figure 2.22 - Seebeck Coefficient as function of Temperature: Single nanowire thermopower response for the same nanowires as Figure 2.21. Inset is an SEM image of the electrical device.

Aside from filtering, the possibility exists that electronic quantum confinement caused by closely spaced inclusion layers contributes to the rise in Seebeck values.[64,65] Since l values of less than 2.34 nm (exciton Bohr radius of ZnO) were observed, thermopower enhancement might be due to slight changes in the density of states near the Fermi level.[66] While difficult to

quantify at this time, the random nature of the single crystalline, polytypoid nanowires perhaps plays a role in these and other transport phenomena.

2.4.c - Carrier Mobility and Power Factor

To ensure that the observed Seebeck enhancement is not due to mere increases in impurity scattering, FET mobilities were measured on the same nanowires from which the electrical conductivity and Seebeck coefficient were determined (Figure 2.23).[12] Both carrier concentration and mobility enhancements were observed when compared to the pure ZnO nanowires. This indicates that the carrier concentration, and not the mobility, is the limiting factor in the electrical conductivity, contrary to what may have been suspected based on the defects that accompany each basal InO_2^- atomic layer. Furthermore, 177 $cm^2\ V^{-1}\ s^{-1}$ at 300 K is more than twice the field effect mobility value previously measured in single crystalline IGZO thin films.[19] The nature of the mobility enhancement in the polytypoid IGZO nanowires over IGZO thin films is not fully understood.

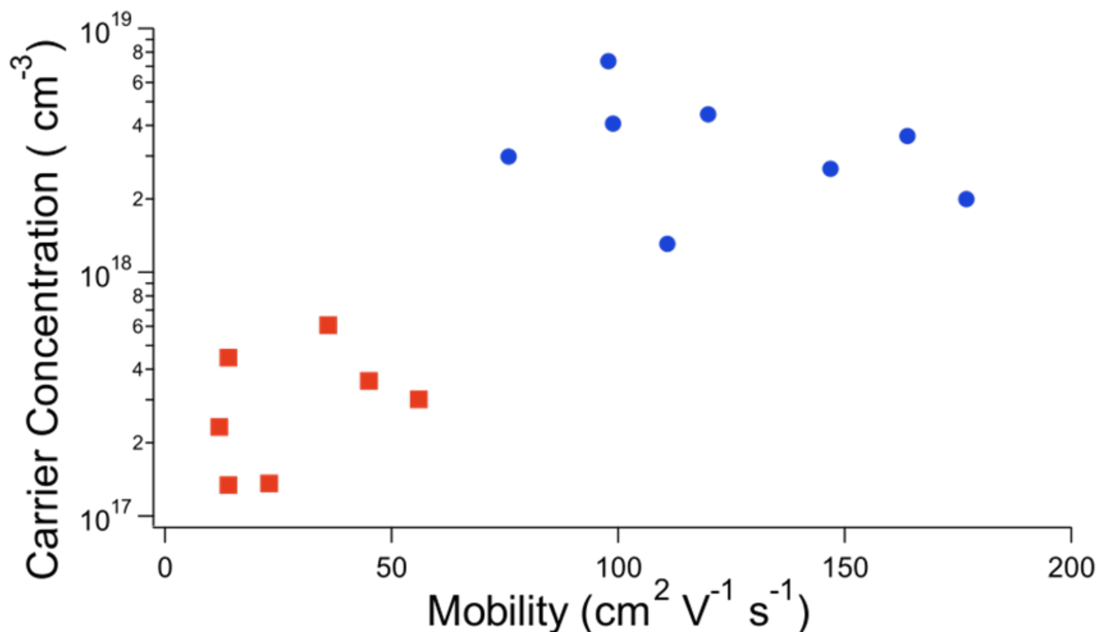

Figure 2.23 - FET Mobility and Carrier Concentration: IGZO (blue circles) exhibited much higher mobilities and carrier concentrations than the starting ZnO (red squares). No diameter dependence was observed for ZnO or IGZO nanowires in the of 75-130 nm.

However, the enhancement over the single crystalline ZnO nanowires may be explained by the induced strain at the InO_2^- layer interfaces. It is well established that piezoresistive materials, both crystalline and amorphous, demonstrate mobility changes with the application of stress.[67,68] As seen in Figure 2.12b, the 17% difference in the d spacing at the octahedral/ wurtzite interface produces a significant amount of strain. Although the inclusions are perpendicular to the transport direction, the mobility could be enhanced by possible strain-

induced changes to the electronic band structure. Further theoretical and experimental work is necessary to determine the extent to which strain plays a role in this polytypoid system.

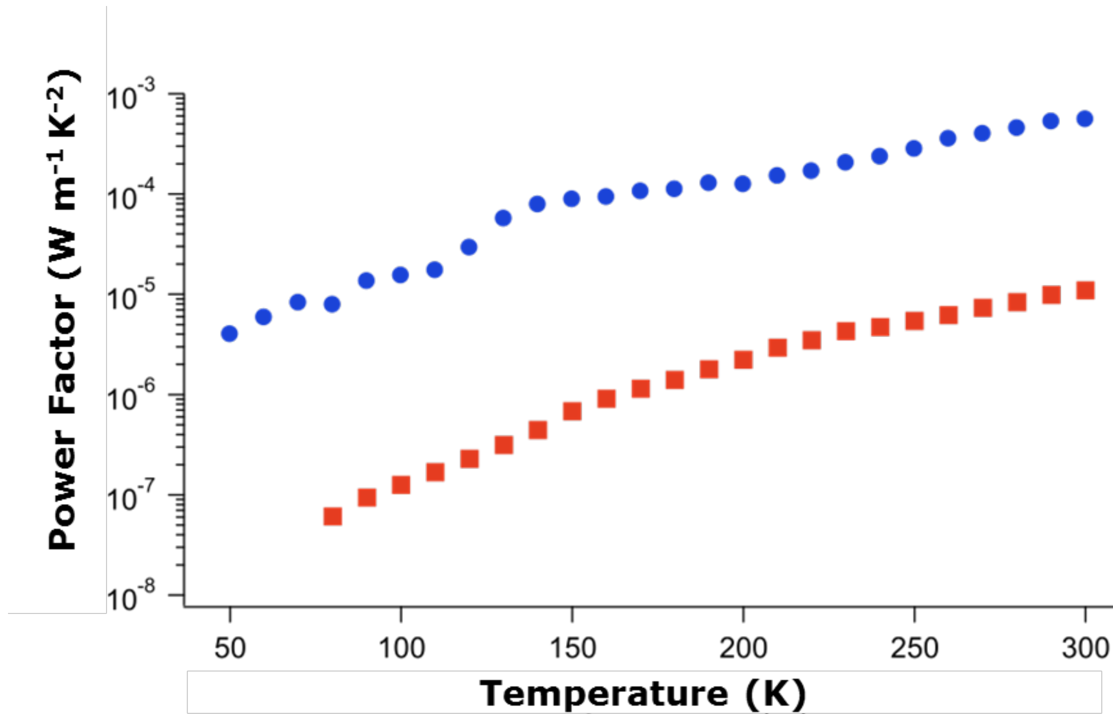

Figure 2.24 - $S^2\sigma$ as function of Temperature: The Seebeck and electrical conductivity were acquired on the same nanowires.

Regardless of the source of enhancement, by converting the ZnO nanowires into IGZO, the resulting power factor ($S^2\sigma$) changed by a factor of 58 to 0.6 mW m^{-1} K^{-2}. While this value is lower than the reported power factor of nominally Al-doped ZnO,[69] it is ~6 times larger than the power factor of bulk IZO materials (Figure 2.24). The complete thermoelectric properties for bulk IGZO have not been reported in a single study within the operating temperature range of our measurement systems. Therefore, transport properties within this work are primarily given relative to the similarly structured bulk IZO.

2.4.d - Thermal Conductivity and Figure of Merit

Not only do the nanostructured features influence electronic transport, they also act as important phonon scattering interfaces, thereby limiting the lattice thermal conductivity.[70] To measure such effects, thermal transport in individual nanowires was accomplished using pre-fabricated MEMS devices, upon which single nanowires were physically manipulated using thin tungsten probe tips (inset of Figure 2.25). Full descriptions of the measurement scheme can be found elsewhere.[71] Compared to literature values for bulk ZnO (100 W m^{-1} K^{-1}), ZnO nanowires demonstrate up to five-fold reduction of thermal conductivity at room temperature (Figure 2.25).[72] An estimation of the average phonon mean free path as a function of temperature shows that the limiting factor is the nanowire diameter until the 150–200 K range,

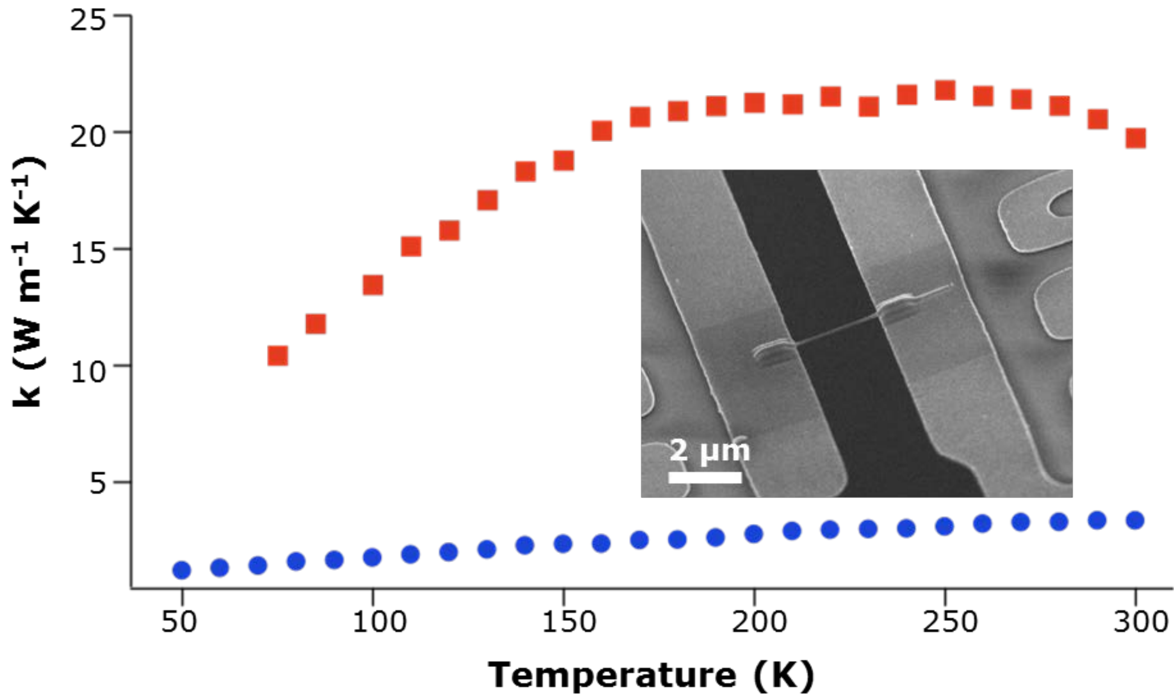

Figure 2.25 – Thermal Conductivity as Function of Temperature: Measurements were conducted on 120 nm 5/5 IGZO (blue circles) and a 90 nm ZnO nanowire (red squares). Inset is an SEM of an individual IGZO nanowire bridging two suspended membranes on a prefabricated MEMS device.

where other scattering mechanisms, such as impurity and Umklapp scattering, begin to limit the conductivity. As seen in Figure 2.26, the linear segment of the ZnO nanowire plot begins to plateau around that temperature range. The IGZO nanowires, on the other hand, show no such plateau, indicating that the inclusions, and not to the nanowire diameter, are limiting the average phonon mean free path throughout the measured temperature range. At 300 K, IGZO nanowires exhibit a thermal conductivity of 3.3 W m^{-1} K^{-1}, which is only slightly lower than what has been observed for IZO in the bulk (3.5 W m^{-1} K^{-1}, n = 3,4).[73] However, since bulk IZO has both higher inclusion density and periodicity, it is surprising that the more disordered 5/5 IGZO nanowires exhibit comparable thermal transport properties. While higher inclusion densities are expected to limit the average phonon mean free path, the disordered nature of the polytypoid IGZO structure combined with the nanowire geometry similarly affects the overall thermal energy propagation, as seen in other systems.[74]

As a direct result of the polytypoid structure, *z*T was increased from 1.7×10^{-4} for ZnO nanowires to 0.055 for the IGZO nanowires at 300 K, an enhancement of 2.5 orders of magnitude (Figure 2.26).[75,76] Such *z*T values represent a factor of ~10 enhancement when compared to the similarly structured bulk IZO superlattice samples at room temperature. However, since oxide-based thermoelectric modules are typically employed at elevated temperatures (700-1000 K), further studies within the relevant temperature range are required.

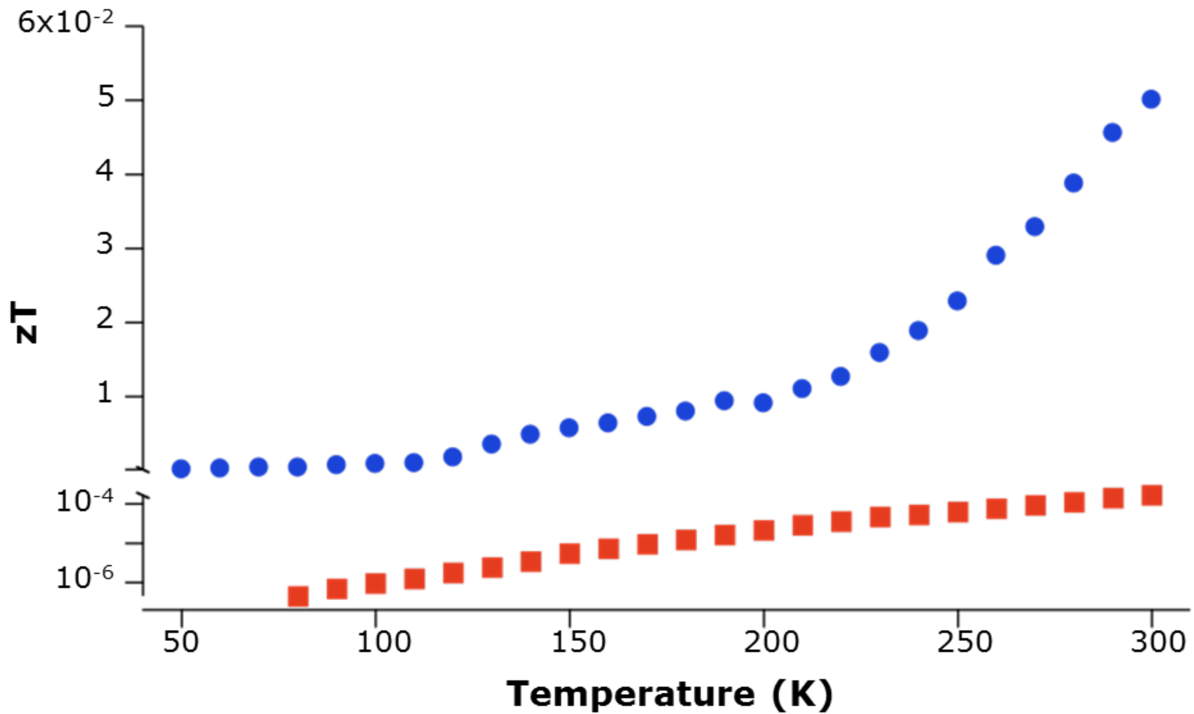

Figure 2.26 – Figure of Merit: Combining all the various components of zT together, IGZO nanowires show 2.5 orders of magnitude enhancement over ZnO nanowires.

2.5 - Conclusions

In summary, $InMO_3(ZnO)_n$ (M = Ga, Fe) polytypoid nanowires were converted from pure ZnO nanowires using a facile diffusion scheme. This solid-state diffusion process can be used to produce a wide range of ZnO alloys with controllable alloy concentration and inclusion layer density. The inclusion growth is believed to originate from a surface defect and propagate though the nanowire by a defect-assisted process. The ultimate structure described here includes multiple inversion domain boundaries and is able to account for experiment observation, as well as being validated through DFT calculations. Single-nanowire measurements on IGZO show that both the power factor and thermal resistivity were enhanced due to the nanostructured features inherent to this thermally stable system. In addition, compared to bulk IZO and other doped ZnO, IGZO nanowires show a marked improvement in zT at room temperature. This work suggests that better control of nanometer-scale features (nanowire geometry, alloying, atomic layer inclusions) could be the key to developing next-generation thermoelectric materials.

2.5 - References

1. Hochbaum, A. I. & Yang, P. Semiconductor nanowires for energy conversion. *Chemical Reviews* **110**, 527–46 (2010).
2. Snyder, G. J. & Toberer, E. S. Complex thermoelectric materials. *Nature Materials* **7**, 105–14 (2008).
3. Hicks, L. & Dresselhaus, M. Thermoelectric figure of merit of a one-dimensional conductor. *Physical review B: Condensed matter* **47**, 631–634 (1993).
4. Donadio, D. & Galli, G. Atomistic simulations of heat transport in silicon nanowires. *Physical review letters* **102**, 195901 (2009).
5. Harman, T. C., Taylor, P. J., Walsh, M. P. & Laforge, B. E. Quantum Dot Superlattice Thermoelectric Materials and Devices. *Science* **297**, (2002).
6. Boukai, A. I. *et al.* Silicon nanowires as efficient thermoelectric materials. *Nature* **451**, 168–171 (2008).
7. Biswas, K. *et al.* High-performance bulk thermoelectrics with all-scale hierarchical architectures. *Nature* **489**, 414–8 (2012).
8. Heremans, J., Jovovic, V. & Toberer, E. Enhancement of thermoelectric efficiency in PbTe by distortion of the electronic density of states. *Science* **554**, (2008).
9. Hsu, K. F. *et al.* Cubic AgPb(m)SbTe(2+m): bulk thermoelectric materials with high figure of merit. *Science (New York, N.Y.)* **303**, 818–21 (2004).
10. Hochbaum, A. I. *et al.* Enhanced thermoelectric performance of rough silicon nanowires. *Nature* **451**, 163–7 (2008).
11. Rogacheva, E. I. *et al.* Quantum size effects in PbSe quantum wells. *Applied Physics Letters* **80**, 2690 (2002).
12. Liang, W. *et al.* Field-effect modulation of Seebeck coefficient in single PbSe nanowires. *Nano letters* **9**, 1689–1693 (2009).
13. Gu, Y., Kuskovsky, I. L., Yin, M., O'Brien, S. & Neumark, G. F. Quantum confinement in ZnO nanorods. *Applied Physics Letters* **85**, 3833 (2004).
14. Chen, R. *et al.* Thermal Conductance of Thin Silicon Nanowires. *Physical Review Letters* **101**, 1–4 (2008).
15. Yan, Y. *et al.* Polytypoid structures in annealed In[sub 2]O[sub 3]–ZnO films. *Applied Physics Letters* **73**, 2585 (1998).
16. Kimizuka, N., Isobe, M. & Nakamura, M. Sntheses and single-crystal data of homologous compounds, In2O3(ZnO)m (m = 3, 4, and 5), InGaO3(ZnO)3, and Ga2O3(ZnO)m (m = 7, 8, 9, and 16) in the In2O3-ZnGa2O4-ZnO system. *Journal of Solid State Chemistry* **116**, 170–178 (1995).
17. Li, C., Bando, Y., Nakamura, M. & Kimizuka-, N. Antiphase Modulated Structure of Fe2 O3 (ZnO)15 Studied by High-Resolution Electron Microscopy. *Journal of Solid State Chemistry* **142**, 174–179 (1999).
18. Hörlin, T., Svensson, G. & Olsson, E. Extended defect structures in zinc oxide doped with iron and indium. *Journal of Materials Chemistry* **8**, 2465–2473 (1998).

19. Nomura, K. *et al.* Thin-film transistor fabricated in single-crystalline transparent oxide semiconductor. *Science* **300**, 1269–72 (2003).
20. Nomura, K. *et al.* Room-temperature fabrication of transparent flexible thin-film transistors using amorphous oxide semiconductors. *Nature* **432**, 488–92 (2004).
21. Lee, S. & Nathan, A. Localized tail state distribution in amorphous oxide transistors deduced from low temperature measurements. *Applied Physics Letters* **101**, 113502 (2012).
22. Kim, S., Kim, K.-K. & Kim, H. Carrier transport mechanism at metal/amorphous gallium indium zinc oxides interfaces. *Applied Physics Letters* **101**, 033506 (2012).
23. Huang, X. *et al.* Electrical instability of amorphous indium-gallium-zinc oxide thin film transistors under monochromatic light illumination. *Applied Physics Letters* **100**, 243505 (2012).
24. Choi, H.-S. *et al.* The impact of active layer thickness on low-frequency noise characteristics in InZnO thin-film transistors with high mobility. *Applied Physics Letters* **100**, 173501 (2012).
25. Jeong, J., Kim, J., Jun Lee, G. & Choi, B.-D. Intrinsic parameter extraction of a-InGaZnO thin-film transistors by a gated-four-probe method. *Applied Physics Letters* **100**, 023506 (2012).
26. Kim, W.-K. *et al.* Stable high conductive amorphous InGaZnO driven by hydrogenation using hot isostatic pressing. *Applied Physics Letters* **98**, 122109 (2011).
27. Duahn, B. *et al.* Influence of thermal annealing ambient on Ga-doped ZnO thin films. *Journal of Crystal Growth* **309**, 128–133 (2007).
28. Zhou, M. *et al.* Optical and Electrical Properties of Ga-Doped ZnO Nanowire Arrays on Conducting Substrates. *The Journal of Physical Chemistry C* **113**, 8945–8947 (2009).
29. Wiff, J. P., Kinemuchi, Y. & Watari, K. Hall mobilities of Al- and Ga-doped ZnO polycrystals. *Materials Letters* **63**, 2470–2472 (2009).
30. Cheng, H., Xu, X. J., Hng, H. H. & Ma, J. Characterization of Al-doped ZnO thermoelectric materials prepared by RF plasma powder processing and hot press sintering. *Ceramics International* **35**, 3067–3072 (2009).
31. Kinemuchi, Y., Ito, C. & Kaga, H. Thermoelectricity of Al-doped ZnO at different carrier concentrations. *Journal of Materials Research* **22**, 3–7 (2007).
32. Ohtaki, M., Araki, K. & Yamamoto, K. High Thermoelectric Performance of Dually Doped ZnO Ceramics. *Journal of Electronic Materials* **38**, 1234–1238 (2009).
33. Ohta, H., Seo, W. & Koumoto, K. Thermoelectric Properties of Homologous Compounds in the ZnO–In2O3 System. *Journal of the American Ceramic Society* **79**, 2193–2196 (2005).
34. Wu, L., Zhang, X., Wang, Z., Liang, Y. & Xu, H. Synthesis and optical properties of ZnO nanowires with a modulated structure. *Journal of Physics D: Applied Physics* **41**, 195406 (2008).
35. Zhang, X. *et al.* Crystal Structure of In 2 O 3 (ZnO) m Superlattice Wires and Their Photoluminescence Properties. *Crystal Growth & Design* **9**, 364–367 (2009).
36. Li, D., Wang, G., Yang, Q. & Xie, X. Synthesis and photoluminescence of InGaO3 (ZnO) m nanowires with perfect superlattice structure. *The Journal of Physical …* **3**, 21512–21515 (2009).

37. Na, C., Bae, S. & Park, J. Short-period superlattice structure of Sn-doped In2O3 (ZnO) 4 and In2O3 (ZnO) 5 nanowires. *The Journal of Physical Chemistry B* **3**, 12785–12790 (2005).
38. Huang, D. L., Wu, L. L. & Zhang, X. T. Size-Dependent InAlO3(ZnO)m Nanowires with a Perfect Superlattice Structure. *The Journal of Physical Chemistry C* **114**, 11783–11786 (2010).
39. Goldberger, J., Sirbuly, D. J., Law, M. & Yang, P. ZnO Nanowire Transistors. *The Journal of Physical Chemistry B* **109**, 9–14 (2005).
40. Uchida, N., Bando, Y., Nakamura, M. & Kimizuka, N. High-resolution Electron Microscopy of Homologous Compounds InFeO3(ZnO)m. *Journal of Electron Microscopy* **43**, 146–150 (1994).
41. Li, C., Bando, Y., Nakamura, M., Onoda, M. & Kimizuka, N. Modulated Structures of Homologous Compounds InMO3(ZnO)m(M=In, Ga;m=Integer) Described by Four-Dimensional Superspace Group. *Journal of Solid State Chemistry* **139**, 347–355 (1998).
42. Yan, Y., Da Silva, J. L. F., Wei, S.-H. & Al-Jassim, M. Atomic structure of In2O3–ZnO systems. *Applied Physics Letters* **90**, 261904 (2007).
43. Da Silva, J., Yan, Y. & Wei, S.-H. Rules of Structure Formation for the Homologous InMO3(ZnO)n Compounds. *Physical Review Letters* **100**, 25–28 (2008).
44. Yu, W. & Mader, W. Displacement field measurement of metal sub-lattice in inversion domains of indium-doped zinc oxide. *Ultramicroscopy* **110**, 411–417 (2010).
45. Schmid, H., Okunishi, E., Oikawa, T. & Mader, W. Structural and elemental analysis of iron and indium doped zinc oxide by spectroscopic imaging in Cs-corrected STEM. *Micron* **43**, 49–56 (2012).
46. Schmid, H., Okunishi, E. & Mader, W. Defect Structures in ZnO Studied by High-Resolution Structural and Spectroscopic Imaging. *Ultramicroscopy* (2012).doi:10.1016/j.ultramic.2012.07.014
47. Wen, J., Wu, L. & Zhang, X. A unique arrangement of atoms for the homologous compounds InMO3(ZnO)m (M=Al, Fe, Ga, and In). *Journal of Applied Physics* **111**, 113716 (2012).
48. Perdew, J., Burke, K. & Ernzerhof, M. Generalized Gradient Approximation Made Simple. *Physical Review Letters* **77**, 3865–3868 (1996).
49. Kresse, G. & Furthmüller, J. Efficient iterative schemes for ab initio total-energy calculations using a plane-wave basis set. *Physical Review B* **54**, 11169–11186 (1996).
50. Kresse, G. & Joubert, D. From ultrasoft pseudopotentials to the projector augmented-wave method. *Physical Review B* **59**, 1758–1775 (1999).
51. Dudarev, S. L., Botton, G. A., Savrasov, S. Y., Humphreys, C. J. & Sutton, A. P. Electron-energy-loss spectra and the structural stability of nickel oxide: An LSDA+ U study. *Physical Review B* **57**, 1505–1509 (1998).
52. Wang, L., Maxisch, T. & Ceder, G. Oxidation energies of transition metal oxides within the GGA+U framework. *Physical Review B* **73**, 195107 (2006).
53. Shannon, R. D. Revised effective ionic radii and systematic studies of interatomic distances in halides and chalcogenides. *Acta Crystallographica* **A32**, 751–767 (1976).
54. Thomas, D. The diffusion and precipitation of indium in zinc oxide. *Journal of Physics and Chemistry of Solids* **9**, 31–42 (1959).

55. Tomlins, G., Routbort, J. & Mason, T. Zinc self-diffusion, electrical properties, and defect structure of undoped, single crystal zinc oxide. *Journal of Applied Physics* **87**, 117–123 (2000).
56. Nakagawa, T. *et al.* Analysis of Indium Diffusion Profiles Based on the Fermi-Level Effect in Single-Crystal Zinc Oxide. *Japanese Journal of Applied Physics* **47**, 7848–7850 (2008).
57. Nakagawa, T. *et al.* Diffusion Model of Gallium in Single-Crystal ZnO Proposed from Analysis of Concentration-Dependent Profiles Based on the Fermi-Level Effect. *Japanese Journal of Applied Physics* **46**, 4099–4101 (2007).
58. Popovici, G., Kim, W. & Botchkarev, A. Impurity contamination of GaN epitaxial films from the sapphire, SiC and ZnO substrates. *Applied physics …* **71**, 3385–3387 (1997).
59. Li, C., Bando, Y., Nakamura, M. & Kimizuka, N. Relation between In ion ordering and crystal structure variation in homologous compounds InMO3(ZnO)m (M = Al and In; m = integer). *Micron* **31**, 543–50 (2000).
60. Yuan, G.-D. *et al.* Tunable n-Type Conductivity and Transport Properties of Ga-doped ZnO Nanowire Arrays. *Advanced Materials* **20**, 168–173 (2008).
61. Nomura, K. *et al.* Carrier transport in transparent oxide semiconductor with intrinsic structural randomness probed using single-crystalline InGaO[sub 3](ZnO)[sub 5] films. *Applied Physics Letters* **85**, 1993 (2004).
62. Shakouri, A., Lee, E. Y., Venky, D. L. S., John, N. & Bowers, E. Thermoelectric Effects in Submicron Heterostructure Barriers. *Microscale Thermophysical Engineering* **2**, 37–47 (1998).
63. Whitlow, L. & Hirano, T. Superlattice applications to thermoelectricity. *Journal of Applied Physics* **78**, 5460–5466 (1995).
64. Hicks, L. & Dresselhaus, M. Effect of quantum-well structures on the thermoelectric figure of merit. *Physical Review B* **47**, 727–731 (1993).
65. Ohta, H., Huang, R. & Ikuhara, Y. Large enhancement of the thermoelectric Seebeck coefficient for amorphous oxide semiconductor superlattices with extremely thin conductive layers. *physica status solidi (RRL) – Rapid Research Letters* **2**, 105–107 (2008).
66. Senger, R. & Bajaj, K. Optical properties of confined polaronic excitons in spherical ionic quantum dots. *Physical Review B* **68**, 1–8 (2003).
67. Li, B., Han, R. & Wang, Y. Effects of strain on the electron mobility in SOI Si-MOSFET. *Solid-State and Integrated Circuit Designs* 544–546 (1995).at <http://ieeexplore.ieee.org/xpls/abs_all.jsp?arnumber=503345>
68. Alahmed, Z. & Fu, H. Polar semiconductor ZnO under inplane tensile strain. *Physical Review B* **77**, 1–10 (2008).
69. Tsubota, T., Ohtaki, M., Eguchi, K. & Arai, H. Thermoelectric properties of Al-doped ZnO as a promising oxidematerial for high-temperature thermoelectric conversion. *Journal of Materials Chemistry* **7**, 85–90 (1997).
70. Chen, G., Narayanaswamy, a. & Dames, C. Engineering nanoscale phonon and photon transport for direct energy conversion. *Superlattices and Microstructures* **35**, 161–172 (2004).
71. Shi, L. *et al.* Measuring Thermal and Thermoelectric Properties of One-Dimensional Nanostructures Using a Microfabricated Device. *Journal of Heat Transfer* **125**, 881 (2003).

72. Özgür, Ü. *et al.* Thermal conductivity of bulk ZnO after different thermal treatments. *Journal of Electronic Materials* **35**, 550–555 (2006).
73. Kaga, H., Asahi, R. & Tani, T. Thermoelectric Properties of Highly Textured Ca-Doped (ZnO) m In 2 O 3 Ceramics. *Japanese Journal of Applied Physics* **43**, 7133–7136 (2004).
74. Chiritescu, C. *et al.* Ultralow thermal conductivity in disordered, layered WSe2 crystals. *Science (New York, N.Y.)* **315**, 351–3 (2007).
75. Tani, T., Isobe, S., Seo, W.-S. & Koumoto, K. Thermoelectric properties of highly textured (ZnO)5In2O3 ceramics. *Journal of Materials Chemistry* **11**, 2324–2328 (2001).
76. Fang, L. *et al.* Thermoelectric and Magnetothermoelectric Properties of In-doped Nano-ZnO Thin Films Prepared by RF Magnetron Sputtering. *Journal of Superconductivity and Novel Magnetism* **23**, 889–892 (2010).

Chapter 3

The possibility of P-type ZnO Nanowires

3.1 - Introduction

3.1.a – The Importance of p-type ZnO

One dimensional semiconductor nanostructures are promising building blocks for nanoelectronic and nano-optoelectronic devices, such as light-emitting diodes (LEDs), photodiodes, and nanoscale lasers.[1–4] Much of the initial work one these systems, especially lasers, have involved using photo-excitation as the energy input into the system. This optically pumped scheme has two intrinsic drawbacks: First, optically pumping limits the resolution to the diffraction limit of $\lambda/2$, where λ is the wavelength of the input light.[5] Second, in any practically-designed opto-electronic circuit, the input desired is electrical.[6] Therefore, logic and information can be transmitted on chip, rather than having to be externally prompted.

As for what materials would work best for these applications, ZnO is a prime candidate. Due to the wide band gap (3.4 eV) and large binding energy (~60 meV)[7], ZnO is suitable for short wavelength device applications, such as ultraviolet lasers and light-emitting diodes.[8] Room temperature lasing has long been established in ZnO nanowires because of these excellent optical properties.[4]

Typically, ZnO is grown unintentionally n-type, meaning electrons are the majority carrier within the semiconductor.[9,10] This is due to the intrinsically occurring donor defects in ZnO, namely oxygen vacancies and zinc interstitials. Some control over these intrinsic defects has been achieved by controlling the growth conditions and cooling rate down from the growth temperature,[11] but these donors are thermodynamically forming defects that spontaneously form. For the purposes of attaining high conductivity in ZnO, they can be both a blessing and a curse, as will be discussed in the next section of this thesis. ZnO is also capable of being doped to relatively high carrier concentrations using Ga, Al, and other trivalent species.[12–17] These doped forms of ZnO are commonly used as transparent contacts, as the wide band gap of ZnO is typically not affected by the introduction of these defects.[18–21]

While n-type conduction in ZnO is well established and somewhat controllable, there is a need to achieve conduction where the majority of charge carriers are holes. For example, solid-state LEDs are typically designed as a p-n junction, where under applied bias, majority carriers from their respective sides recombine near the junction (within a depletion width). This is typically done via a homojuntion, where the n-type and p-type materials are the same.[2,22–24]

In principle, this restriction of the same material is not needed, but many studies show that the much lower quality interface between materials leads to reduce device performance.[25] This can manifest in markedly worsened output spectra and/or larger operation voltages required for the same amount of light produced. Therefore, it is most desirable to maintain the same material across the junction, wherein there is perfect relation between the two crystal structures (if viewed independently). In turn, this spurns the need for conductive p-type ZnO.

3.1.b – Obstacles to p-type Conduction

Even though the idea of having p-type ZnO is a very enticing prospect, there exist a great deal of problems in its creation and stability. The prerequisites for "useful" p-type ZnO are for the acceptor concentration to be much higher than the donor concentration, and low acceptor ionization energy, preferably well below 0.2 eV in the dilute limit.[26,27] In order to achieve high substitutional acceptor concentration, the solid solubility of the particular acceptor impurity in mind must be high with a low self-compensation ratio. Unfortunately, many of the traditional transition metal dopants with an oxidation state of +1 are not very soluble in ZnO.[2,28–30] Additionally, their high ionization energies render the majority of dopants useless at room temperature.

While suitable dopants and dopant pairs can be chosen to somewhat avoid those two issues, the compensation of native donor defects in omnipresent. On an absolute level, the doping asymmetry caused by compensation arises from the fact that wide-gap semiconductors either have a low valence-band maximum or a high conduction-band minimum.[31,32] Some semiconductors such as ZnTe, CdTe, and diamond in which the valence band is relatively close to the vacuum level have preferable p-type conductivity, Therefore, achieving n-type conductivity is very difficult, diamond being the case in point. In contrast, ZnO, ZnSe, ZnS, and CdS, which their valence bands relatively far from the vacuum level, have preferable n-type conductivity. For ZnO, the same intrinsic defects (oxygen vacancies, V_o, and zinc interstitials, Zn_i) which are responsible for as-made n-type conduction retard the efforts to achieve stable p-type doping by compensating the potential acceptors.

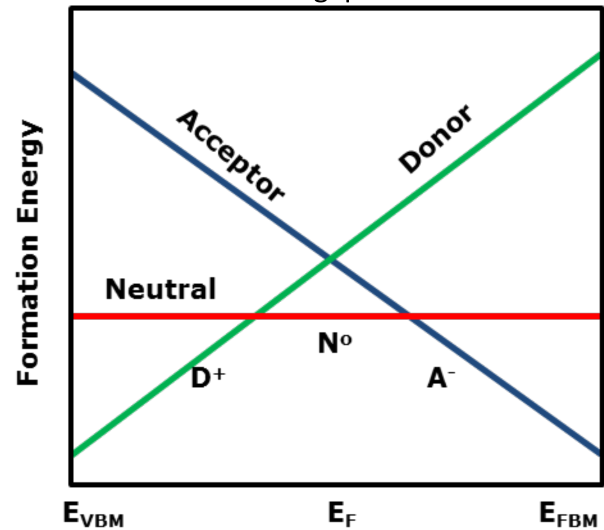

Figure 3.1 – Formation Energy as Function of Fermi Energy: Schematic dependence of the formation energy of charged defects on the Fermi energy position within the band.

Considering the band structure of a doped semiconductor, this compensation is due to the fact that the formation energy of these intrinsic defects is dependent to the chemical potential (Fermi level) of the doped material (Figure 3.1). For ZnO specifically, the formation of Zn_i and V_o becomes much more favorable as the Fermi level approaches the valance band (left

side of Figure 3.1).[33] Eventually, the formation of these defects becomes energetically favorable, and thus will begin to spontaneously form over time. Therefore, in the presence of such compensation, there is an effective thermodynamic limit as to what the finally carrier concentration can be.[34]

3.1.c – Strategy to Bypass Compensation

As is shown in Figure 3.1, there is a dependence of the formation energy of charged defects on the Fermi level. Therefore, when charged extrinsic defects, ie dopants, are introduced into the system, the Fermi level is moved either towards the valence band if an acceptor state or towards the conduction band if a donor state. Once the Fermi level has changed, the intrinsic, charged defects (for ZnO, Zn_i and V_o) either become more or less favorable to form. Since dopants are charged defects by definition (either active or non-active), this presents a fundamental problem for p-type doping.

Consider, however, if the dopant was not always in a charged state. For example, what if the possibility existed where a neutral extrinsic defect could be introduced to the lattice of ZnO during growth, then controllably "turned on" to an acceptor state afterwards? Then the benefits would be two-fold: First, the uncharged species would not affect the intrinsic defect concentration for charged species, such as Zn_i and V_o, since the Fermi level is unaffected by their presence (neutral line in Figure 3.1). Since there is no driving force for formation of compensating donor defects (at least, not any larger force than in pure ZnO), the material could exist indefinitely in this state. Second, the "turn on" step is separated from the high temperatures of crystal growth (assuming gas-phase conditions). Being separate allows this "turn on" to be done at lower temperature;[35] hence less available energy for intrinsic donors to use to form. While still thermodynamically favorable to form, these defects would be kinetically trapped, allowing for much higher hole concentrations and longevity of such conduction.

Such a strategy was employed using uncharged Li-complexes during ZnO growth, followed by dopant an activation anneal at lower temperature to create Li acceptor states. Ab-initio studies have shown that Li interstitials (Li_i) and substitutional Li (for Zn, Li_{Zn}) create a complex that is overall charge neutral.[36,37] After growth, the activation anneal allows the defect complex to break and form charged species, most of which can be acceptors (depending on the annealing environment). Field effect and Seebeck measurements confirm the majority carrier type as positive after annealing. Measurements over time show the conduction to not be stable, reverting to insulating behavior. Reproducibility and other considerations are also discussed.

3.2 – Li-Doped ZnO Nanowires

3.2.a – Synthesis and Conversion

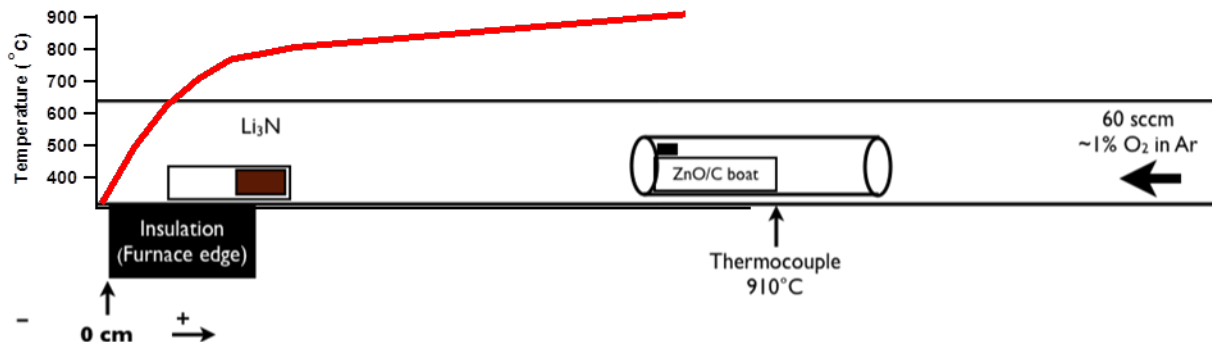

Figure 3.2 – Schematic of CVT Set-up: Positional control of the Li precursor affects the local vapor pressure of Li by changing both temperature and distance. Samples are designated by the relative distance of the Li_3N from the tube edge.

Li-doped ZnO nanowires were synthesized using a modified chemical vapor transport scheme, depicted in Figure 3.2. Briefly, a mixture of ZnO and graphite powered (1:1 by weight) is placed into an alumina boat and positioned inside a quartz tube such that the right edge of the boat is in line with the thermocouple of the tube furnace. An Au-coated (~2-5 nm) sapphire substrate (2 mm x 2 mm piece) that was thoroughly clean by sonication in acetone for 1 hour was placed on the left edge of the boat.[38] The Li precursor used was Li_3N, [39,40] which was placed a certain distance away downstream from the growth zone of the ZnO nanowires. The position of the Li_3N was measured as distance from the left edge of the furnace, wherein longer distances are closer to the center of the tube where growth occurs.

The position of the Li_3N dictates the available vapor pressure of the Li to the growth zone of ZnO nanowires. Because of the dissipation of heat from the center of the tube furnace towards the edge, the position of the Li_3N dictates its temperature. The temperature as a function of position was measured at a set point of 910 ^{o}C (temperature overlay in Figure 3.2), and varies mostly linearly for distances > 5cm. At 6 cm, the temperature is 808 ^{o}C. Temperatures measured closer to the edge of the tube furnace smaller than 5 cm dropped off precipitously, where 3 cm and 1 cm measure 710 ^{o}C and 495 ^{o}C, respectively. While it is convenient to control the temperature, and thus the vapor pressure of Li species, this way, it is not a straightforward relation between position and actual vapor pressure at the ZnO nanowire growth zone. Merely decreasing the distance between the two precursors (ignoring changes in temperature) increases the vapor pressure at the growth zone increases. Adding in the non-uniform temperature to the picture and this becomes a non-linear dependence. Controlling the amount of Li then becomes more challenging, as the window for optimal incorporation while maintaining good nanowire morphology is small.

After the positions of the various precursors were set, 60 sccm of Ar containing ~1% of oxygen purged the reaction tube for 30 minutes at room temperature. The temperature then rapidly climbed to 910 ^{o}C, where it sat for 10-15 minutes, then allowed to cool at a reduced rate. These nanowires were between 10-20 microns long, and varied between 50-200 nm in diameter. For 8 cm samples, there were noticeable morphological changes to the nanowires, as they had much smaller aspect ratios and also consisted of other shaped materials. These changes were attributed to the presence of too much Li. Samples 6 cm and smaller maintained excellent morphology, as seen in Figure 3.3a-c. These nanowires are single crystalline, and maintain good vertical orientation.

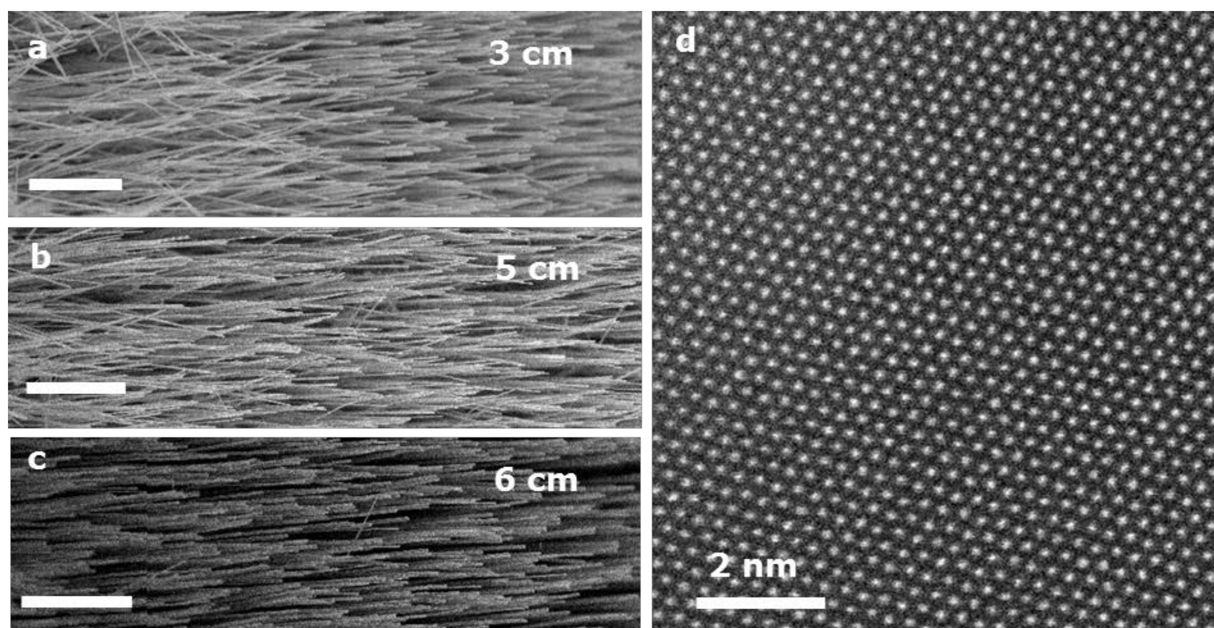

Figure 3.3 – Li-doped Morphology and Crystallinity: SEM images of Li-doped ZnO nanowires grown with Li precursor (a) 3 cm, (b) 5 cm, and (c) 6 cm away from the furnace edge. Scale bars are 2 μm. (d) High Resolution STEM image of a 6 cm Li-doped sample is an example of the single crystal nature of the samples grown in that condition.

Dopant activation annealing was performed both on the growth substrate and single nanowire devices. The on-device annealing was done in either a tube furnace or RTA, with more consistent results occurring in samples annealed in the tube furnace. The following conditions were all used successfully to obtain p-type behavior from tube furnace annealing: 400, 450, and 500 ^{o}C in pure O_2 for 30 or 40 minutes. For the RTA anneal, 400 in O_2 for a total of 5 minutes was also successful. The high oxygen concentration environment is used to facilitate Zn vacancy formation.

3.2.b – Solid-State Characterization

Further analysis of as-made samples was carried out via X-Ray Diffraction. The 100 diffraction peaks of several Li-doped samples are compared to that of pure ZnO nanowires in Figure 3.4a. No shift was observed in the 002 or 101 peaks. An obvious shift is observed from

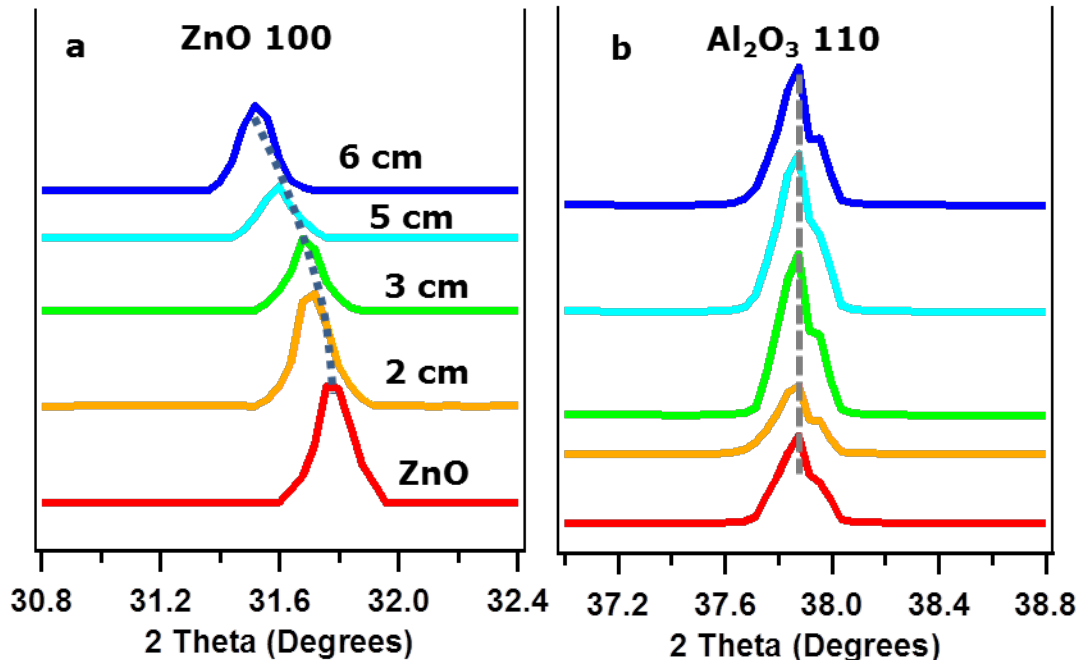

Figure 3.4 – Lattice Expansion in Li-doped ZnO Nanowires: (a) Shift to lower scattering angles is observed for samples grown with the Li precursor closer. As an internal standard, all spectra are calibrated to the 110 peak of the substrate (b). The features on the substrate peak are probably due to detector saturation.

the Li-doped samples, with the largest shift occurring in the 6 cm sample (closest to the growth zone of ZnO). Acting as an internal standard, the 110 peak from the Al_2O_3 substrate is also shown (Figure 3.4b). The extra features on the substrate peaks are attributed to artifacts due to detector saturation. The .27 degree shift seen in the 6 cm sample can be explained by Li incorporation into the ZnO lattice. Li most favorably forms interstitials within ZnO, pushing Zn and O away from each other, ie expanding the lattice. While not overly quantitative, this amount of expansion roughly corresponds to ~3-5% Li incorporation.[36,37,41,42] However, this speciation of Li acts as a donor. Since single nanowire measurements show the electrical conductivity decrease in the as-made samples (as compared to pure ZnO, described in more detail in the next section of this thesis), this is not thought to be the main form of Li. Considering both the lowered conductivity and lattice expansion observed, the main speciation is thought to be the neutral Li-Li complex. Further work examining the local environment of the Li and Zn should be undertaken. Note also that after the activation anneal, the expansion should be somewhat reduced, as the Li-Li complex devolves into independent Li dopants that can then occupy Zn vacancies. However, this measurement was not performed while the samples being produced were consistent.

As further indication of Li incorporation into the ZnO nanowires, photoluminescence (PL) spectra of various samples were acquired. Figure 3.5a shows room temperature PL of pure and 6 cm Li-doped ZnO nanowires. The difference in PL intensity is not meaningful, as the amount of sample is not known. These spectra exhibit little difference from each other at room temperature; however, when taken again at 8K (Figure 3.5b), distinct peaks are observed in the

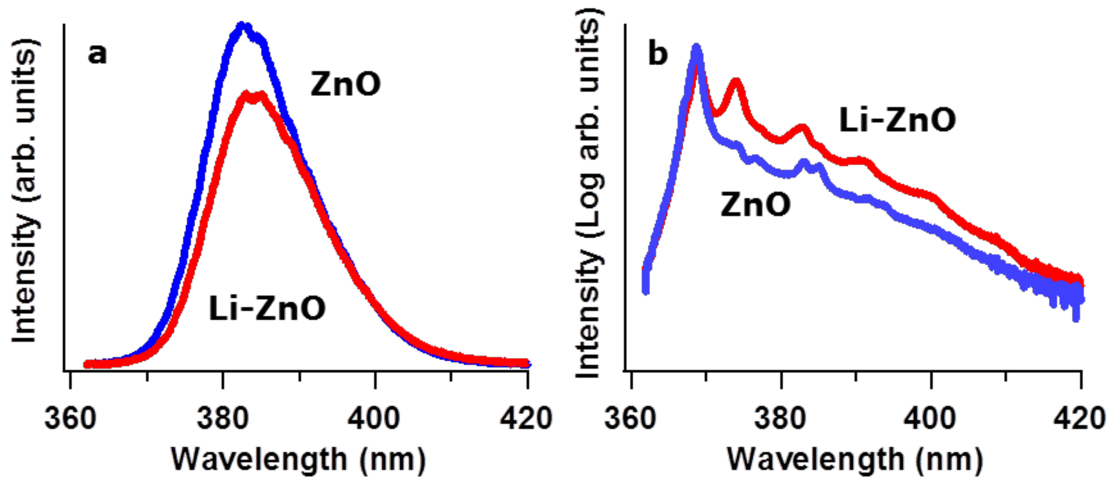

Figure 3.5 – Photoluminescence Detection of Li in ZnO : (a) Room temperature PL of pure ZnO (blue) and 5-cm Li-doped ZnO (red). (b) PL taken of the same samples at ~8K. Features begin to appear in Li-doped ZnO below 90 K.

Li-doped samples. These peaks occurring at 373.9 nm and 382.8 nm are characteristic of the presence of Li in ZnO, as observed by other studies. The peak at 373.9 is typically the strongest, and most present in LI-doped samples. The exact state responsible for this peak is not known.[43–45] It is worth noting that in every sample that exhibited eventual p-type behavior, this peak was observed. However, the converse is not true. This may be due to the fact that the conversion rate is ~40%, meaning that the nanowires on the devices in certain samples did not show p-type behavior for any number of reasons (oxidized electrodes, not enough LI present,…).

Therefore, PL was obtained from a single nanowire device. Figure 3.6 is a plot of PL acquired at 8 K of the same Li-doped ZnO nanowire already in an electrical device. The pre-anneal spectrum contains the 374 nm characteristic peak, indicating the incorporation of Li in the nanowire. After annealing at 450 ^{o}C for 30 minutes in O_2, this specific nanowire sample did exhibit p-type behavior. Accompanied with this change in carrier type are new spectral features. The spectrum changes to a much broader peak centered ~380 nm (note that this spectrum was also taken at 8 K). The shift of the band edge to lower energy photons could be a result of defect levels close to the band edges. Since p-type behavior was observed, it is reasonable to assume that most of the new defect levels are near the valence band.

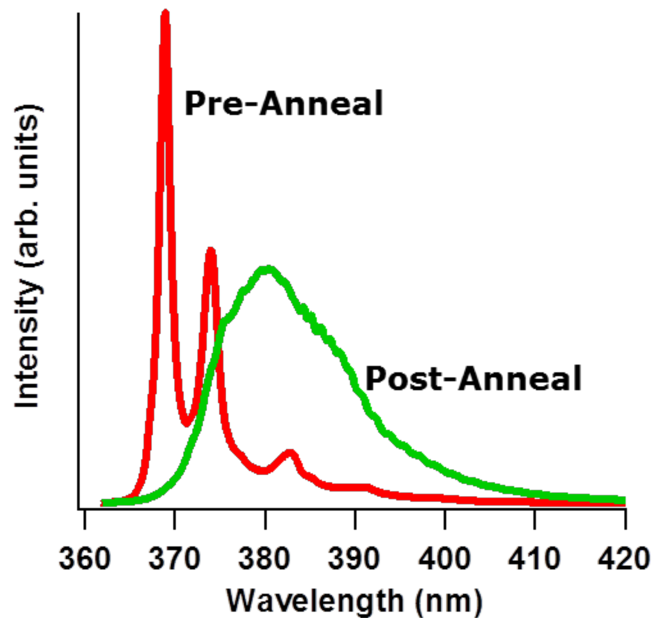

Figure 3.6 – PL of Single Nanowire on Device: PL of the same Li-doped ZnO nanowire in a Seebeck device (red) before the dopant activation anneal and (green) afterwards.

3.3 – Carrier Type Determination

3.3.a – Field-Effect Conduction

As alluded to earlier in this chapter, field effect transistors were fabricated with the active channel material being Li-doped ZnO nanowires. When possible, a four-point contacting scheme was utilized to extract the effects of contact resistance from the intrinsic resistance. Both Ti/Au and Ni/Au (50/150 nm) were used to obtain Ohmic contact to the samples. Note that if the Au film does not completely cover the Ti metal layer, severe oxidation of the metal electrodes occurred, ruining the devices, sometimes completely.

The as-grown Li-doped ZnO nanowires exhibited high resistances, with the average mobility and carrier concentration ~3 $cm^2V^{-1}s^{-1}$ and ~10^{15}-10^{16} cm^{-3}, respectively (Figure 3.11). Because of the large amount of Li required to shift the lattice parameter (on the order of 2-6%), a decrease of the mobility as compared to pure ZnO nanowires was expected, since the concentration of point defects rose substantially. Also, the carrier concentrations for the as-made samples are over an order of magnitude lower than that of pure ZnO. There then must either exist acceptor states tapping free electrons or a lowered amount of intrinsically donating defects in the Li-doped ZnO nanowires.

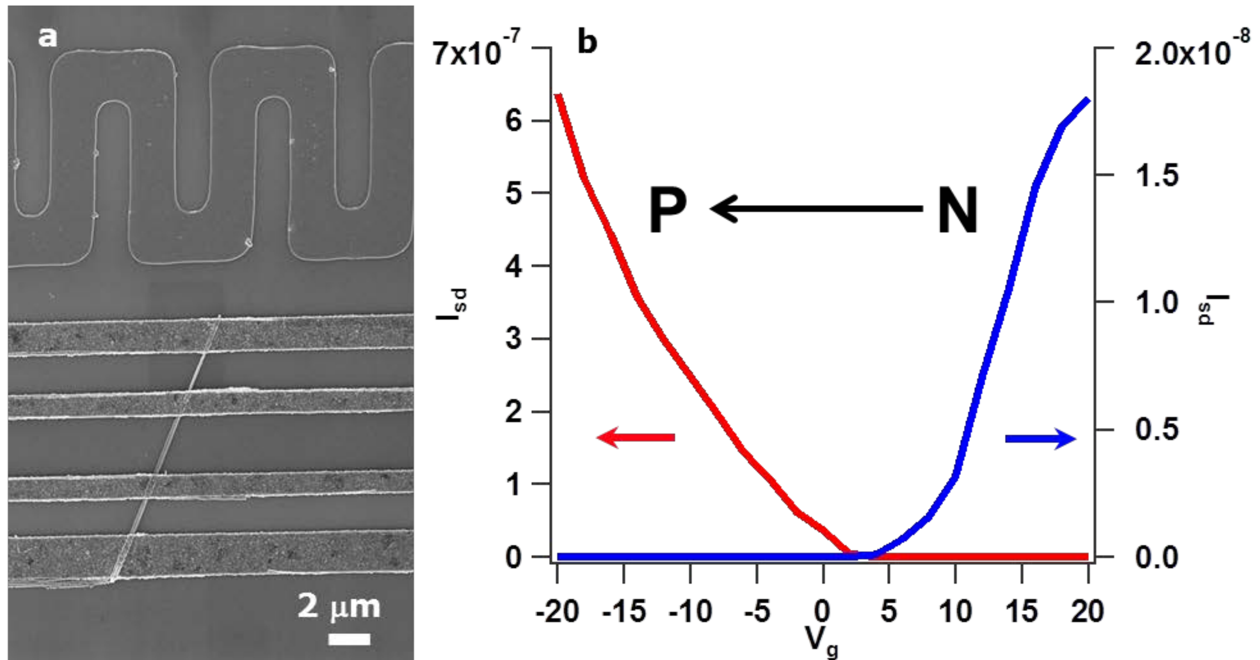

Figure 3.7 – Carrier Type Switching : (a) SEM of a nanowire in a Seebeck device after annealing step. (b) Field effect conduction before (blue) and after (red) the activation anneal was performed On-Chip. V_{ds} = .5 V.

When successful, the n-type conduction of the as-made Li-doped ZnO nanowires is converted to p-type via an annealing step (Figure 3.7b). This on-chip annealing allows for exact tracking of the change of carrier type in the same single crystal nanowire (Figure 3.7a). This switching was repeated several times on multiple devices. In each case, the conductance of the nanowire increased, sometimes substantially. Also interesting is that the threshold voltage remains positive even after activation. Effectively, the “normally off” n-type device was converted to a “normally on” p-type device.

The average mobility and carrier concentrations for the annealed samples are 12 $cm^2V^{-1}s^{-1}$ and ~10^{17} cm^{-3}, respectively (Figure 3.11). While there is certainly room for improvement in carrier concentration, the mobility is higher than previously measured p-type ZnO studies.[44,46–48]

3.3.b – Seebeck Coefficient

As an FET device, nanowires are less than desirable. Large uncertainties exist in many of the measured responses, including slope direction of the transconductance and amount of depletion in the active channel.[49,50] These problems are ever present, especially in the back-gated geometry.[51] Therefore, the Seebeck coefficient was used to confirm the majority carrier type. The relation between the sign of the Seebeck coefficient and majority carrier type can be complicated for heavily doped systems. For example, many metals (Cu, Pb, Al, Au, …) have positive Seebeck coefficients due to where the Fermi level lies relative to the density of states.[52] If a material has a positively-sloped DOS at the Fermi level, the Seebeck will be positive. However, for semiconductors with a gap between bands, the slopes of the DOS near the edges

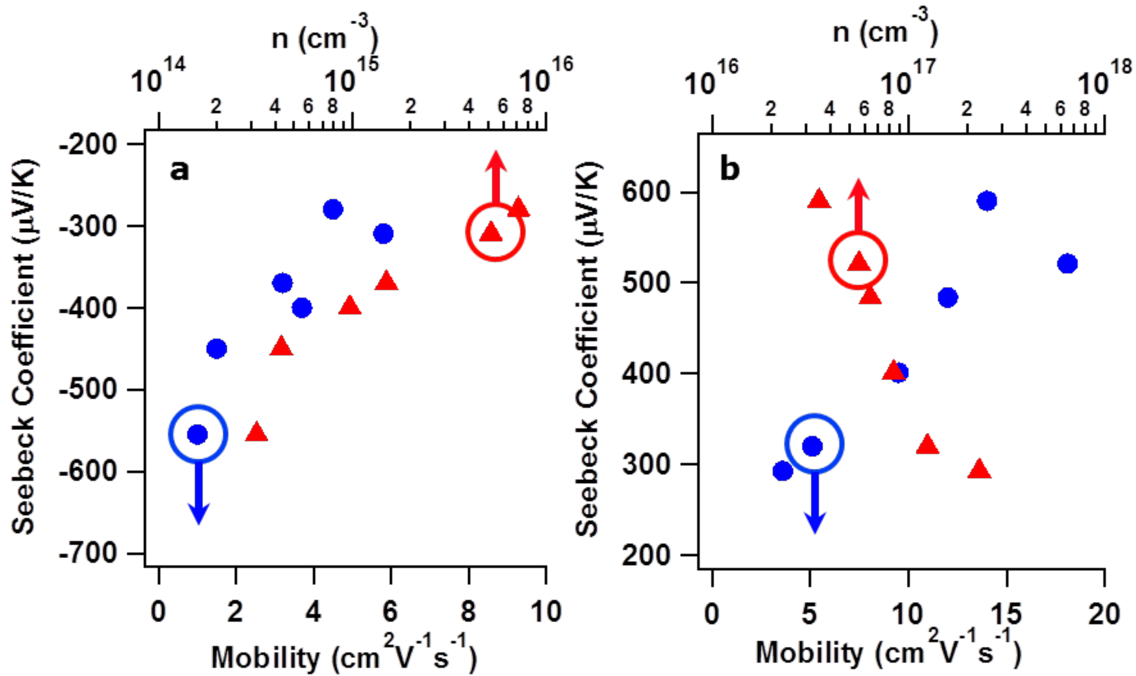

Figure 3.8 – Seebeck Confirmation of Pre-and Post-Annealed Samples: (a) Pre-annealed samples are n-type having a (-) Seebeck response. (b) Activated Li-doped ZnO exhibit (+) Seebeck coefficients. The same nanowires were also measured for mobility (blue, bottom axis) and carrier concentration (red, top axis).

of those bands are respectively different (conduction band is opposite from the valence band).[53] Therefore, if the Fermi level is closer to the conduction band, the slope of the DOS is negative, giving the Seebeck voltage a negative sign. Likewise, if the Fermi level is closer to the valence band edge, the Seebeck voltage will be positive. Therefore, by doping a semiconductor n- or p-type, the sign of the Seebeck will reflect that majority type as a consequence of the Fermi level position within the band.

Since the devices used for the FET measurements also included the capability of measuring the Seebeck voltage, all transport data was acquired on the same individual nanowires and plotted in Figure 3.8. Again, the as-made Li-doped samples have lower mobility and carrier concentrations while also having a relatively large negative Seebeck coefficient (~-400 μV K^{-1}). This relation of large Seebeck with low mobility and carrier concentration is consistent with the Boltzman transport relation between the three variables (See Chapter 1).[54] After annealing, the nanowires exhibit increases in mobility and carrier concentration, as well as a positive Seebeck voltage (Figure 3.8b). This switching of sign is further indication that the majority carriers in the annealed samples are now holes.

3.4 – Stability and Reproducibility

3.4.a – As function of Time and Size

While the conversion from n-type to p-type was successful, the longevity of the p-type response was not very long. Figure 3.9 plots the Seebeck coefficient as function of time for three different Li-doped ZnO nanowire devices. From this plot, there are several aspects to note. First, the longest lived sample without any type of surface modification was less than 148.2 hours, while the shortest was between 10-18 hours. The precise time of reversion is not known due to the discrete segmentation of sampling. The diameters of those samples are not known, due to the lack of diligence on my part. However, the nanowires in Figure 3.9 were measured via SEM after reversion was observed as not to affect the transport properties of the samples with the electron beam. While just three samples, a clear trend as relates to the diameter of the nanowire and longevity can be seen, with the larger sample being more stable over time. The proposed reason for this is the following: formation of donating states on the surface of the nanowires compensates the acceptors distributed throughout the whole nanowire. For smaller nanowires, the surface to volume ratio is larger than thicker samples; thereby they would be more affected by the creation of these surface states. Another explanation is that the thicker nanowires are grown with a larger concentration of Li; therefore, more compensating donor states (V_o or Zn_i) are required to make the reversion happen. Either way, such a dependence on nanowire diameter requires further study, as it has direct consequences on the viability of nanoscale applications of p-type ZnO.

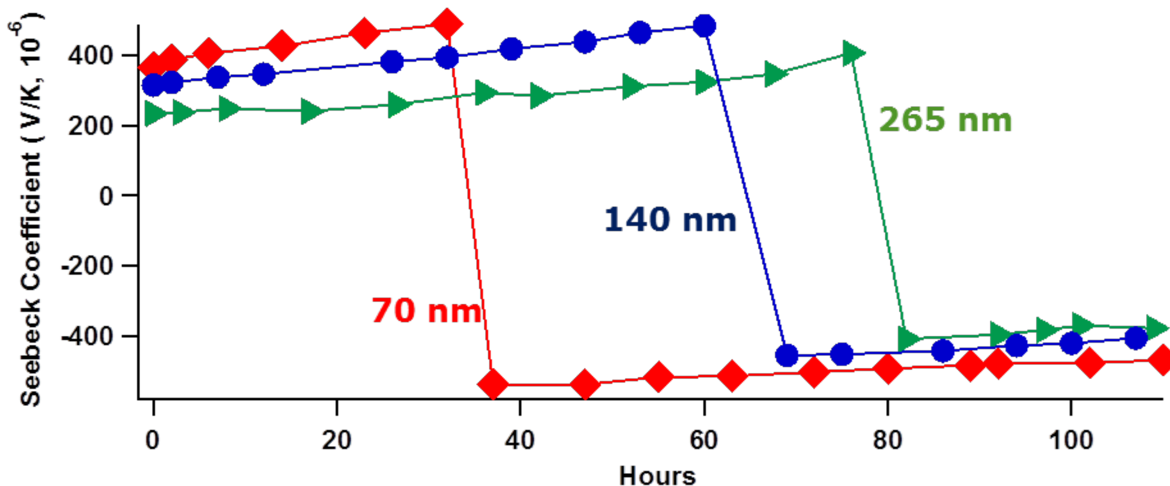

Figure 3.9 – Lifetime of P-Type Behavior: Seebeck Coefficient as a function of time illustrates the inherent instability of p-type ZnO. Additionally, longevity of hole conduction was observed to be dependent on the nanowire diameter.

Another point of interest on the traces of Figure 3.9 is the trend of the magnitude of the Seebeck with time before reversion. In each case, the Seebeck becomes slightly more positive before ultimately switching to negative. This could be due to the position of the Fermi level

changing as more and more donors are spontaneously being created to compensate the excess of holes. As the Fermi level approaches the middle of the bad, the carrier concentration is decreasing, which in turn increases the Seebeck. While it is unclear if this effect would change the Seebeck in this magnitude, the possibility of real time monitoring of the instability of samples is interesting.

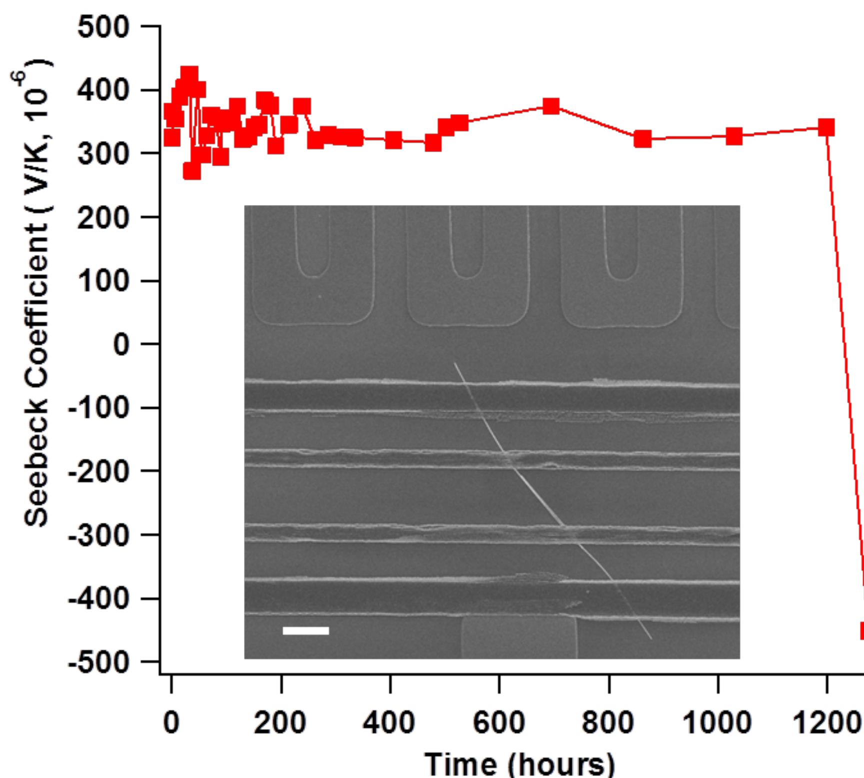

Figure 3.10 – Surface Passivation for Increased Stability: A Li-doped ZnO nanowire coated with ALD Alumina exhibited over an order of magnitude increase in longevity. Inset is an SEM of a single nanowire Seebeck device with scale bar of 2 μm.

In an attempt to increase the longevity of the p-type response, one sample was coated with 20 cycles of ALD alumina. Figure 3.10 shows the successful result of that experiment. The nanowire in this case gave a positive Seebeck for nearly 50 days, much longer than any un-coated device. Note that the sampling rate was not as dense as it should have been. Further work using an automated measuring system rather than a somewhat forgetful graduate student should be employed to prove the cause of such a change in stability.

3.4.b – Thoughts on Issues with Reproducibility

While much of the data presented in this chapter is exciting and not all that different than what is seen in the literature for Li doped ZnO, much of this data cannot be reproduced. In samples made since, no XRD shift has been observed, as well as a glaring lack of the characteristic peak in the low-temperature PL. These nanowire samples have been insulating,

with actual measurements of the carrier concentration and mobility nearly impossible, as there exists very little I_{ds}.

Naturally, the attributed cause for this problem is synthetic. As mentioned earlier, the non-linear dependence of the partial pressure of Li on position leave a very small window of conditions needed for good incorporation while preserving the nanowire morphology. Also, the dependence of the Li speciation is highly dependent on the oxygen concentration.[37] If too much oxygen is present during growth, not only will the li precursor oxidize before getting to the growth zone of the ZnO, but the Li that does make it will have a lessened thermodynamic driving force to form the neutral Li-Li defect complex. Rather, separate Li_i and Zn_{Li} become increasingly stable to exist. Therefore, more care must be taken to control the exact amount of oxygen present during growth.

3.5 – Conclusions

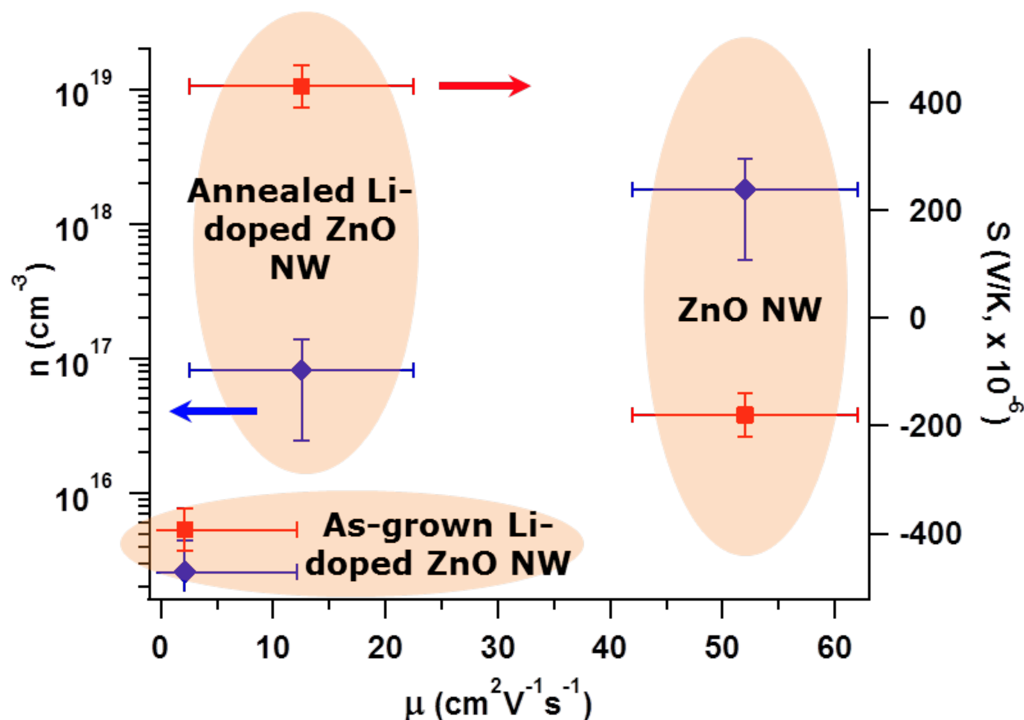

Figure 3.11 – Summary of Electrical Responses: ZnO, As-made Li-doped ZnO, and Annealed Li-doped ZnO nanowires various responses are plotted. Seebeck (red, right side) and carrier concentration (blue, left side) and shown as a function of mobility. Note that the data was plotted this way for ease, not to imply an observed dependence.

Li-doped ZnO nanowires were synthesized via CVT and exhibited p-type conduction after annealing to activate the dopants. XRD and PL measurements were performed to confirm the incorporation of Li into the ZnO nanowires. Expansion of the lattice, as well as the appearance of a signature peak in the PL, was observed for samples grown in the presence of

Li_3N. Electrical responses, including field effect transconductance and Seebeck voltages, were performed on single nanowires, the results and summary of which are shown in Figure 3.11. The stability of the p-type behavior was measured to be on the order of days, possibly showing size dependences. Further work is needed to repeat these measured responses, as well as confirm p-type conduction in doped ZnO.

3.6 – References

1. Duan, X., Huang, Y., Agarwal, R. & Lieber, C. Single-nanowire electrically driven lasers. *Nature* **421**, 241–245 (2003).
2. Chen, M. *et al.* Near UV LEDs made with in situ doped pn homojunction ZnO nanowire arrays. *Nano letters* (2010).at <http://pubs.acs.org/doi/abs/10.1021/nl101907h>
3. Cho, H. D. *et al.* Photovoltaic device on a single ZnO nanowire p-n homojunction. *Nanotechnology* **23**, 115401 (2012).
4. Huang, M. H. *et al.* Room-temperature ultraviolet nanowire nanolasers. *Science (New York, N.Y.)* **292**, 1897–9 (2001).
5. Gargas, D. J., Toimil-Molares, M. E. & Yang, P. Imaging single ZnO vertical nanowire laser cavities using UV-laser scanning confocal microscopy. *Journal of the American Chemical Society* **131**, 2125–7 (2009).
6. Joyce, H. J. *et al.* III–V semiconductor nanowires for optoelectronic device applications. *Progress in Quantum Electronics* **35**, 23–75 (2011).
7. Janotti, A. & Van de Walle, C. G. Fundamentals of zinc oxide as a semiconductor. *Reports on Progress in Physics* **72**, 126501 (2009).
8. Jiao, S. J. *et al.* ZnO p-n junction light-emitting diodes fabricated on sapphire substrates. *Applied Physics Letters* **88**, 031911 (2006).
9. Schlenker, E. *et al.* On the difficulties in characterizing ZnO nanowires. *Nanotechnology* **19**, 365707 (2008).
10. Goldberger, J., Sirbuly, D. J., Law, M. & Yang, P. ZnO Nanowire Transistors. *The Journal of Physical Chemistry B* **109**, 9–14 (2005).
11. Gargas, D. J., Gao, H., Wang, H. & Yang, P. High quantum efficiency of band-edge emission from ZnO nanowires. *Nano letters* **11**, 3792–6 (2011).
12. Ahn, C. H., Han, W. S., Kong, B. H. & Cho, H. K. Ga-doped ZnO nanorod arrays grown by thermal evaporation and their electrical behavior. *Nanotechnology* **20**, 015601 (2009).
13. Sakurai, M., Wang, Y. G., Uemura, T. & Aono, M. Electrical properties of individual ZnO nanowires. *Nanotechnology* **20**, 155203 (2009).
14. Yuan, G.-D. *et al.* Tunable n-Type Conductivity and Transport Properties of Ga-doped ZnO Nanowire Arrays. *Advanced Materials* **20**, 168–173 (2008).
15. Wiff, J. P., Kinemuchi, Y. & Watari, K. Hall mobilities of Al- and Ga-doped ZnO polycrystals. *Materials Letters* **63**, 2470–2472 (2009).
16. Cai, K. F., Müller, E., Drašar, C. & Mrotzek, a. Preparation and thermoelectric properties of Al-doped ZnO ceramics. *Materials Science and Engineering: B* **104**, 45–48 (2003).

17. Bazzani, M., Neroni, A., Calzolari, A. & Catellani, A. Optoelectronic properties of Al:ZnO: Critical dosage for an optimal transparent conductive oxide. *Applied Physics Letters* **98**, 121907 (2011).
18. Messaoudi, C., Sayah, D. & Abd-Lefdil, M. Transparent conducting undoped and indium-�doped zinc oxide films prepared by spray pyrolysis. *physica status solidi (a)* **93**, 93–97 (1995).
19. Nomura, K. *et al.* Room-temperature fabrication of transparent flexible thin-film transistors using amorphous oxide semiconductors. *Nature* **432**, 488–92 (2004).
20. Leenheer, A. *et al.* General mobility and carrier concentration relationship in transparent amorphous indium zinc oxide films. *Physical Review B* **77**, 1–5 (2008).
21. Ataev, B. M., Bagamadova, a. M., Mamedov, V. V., Omaev, a. K. & Rabadanov, M. R. Conductive and transparent zinc oxide films. *Inorganic Materials* **36**, 219–222 (2000).
22. Li, P. *et al.* Electrical and photoresponse properties of an intramolecular pn homojunction in single phosphorus-doped ZnO nanowires. *Nano letters* (2009).at <http://pubs.acs.org/doi/abs/10.1021/nl803443x>
23. Sun, J. C. *et al.* Realization of ultraviolet electroluminescence from ZnO homojunction with n-ZnO⁄p-ZnO:As⁄GaAs structure. *Applied Physics Letters* **90**, 121128 (2007).
24. Tsai, S.-Y., Hon, M.-H. & Lu, Y.-M. Annealing effect on conductivity behavior of Li–doped ZnO thin film and its application as ZnO-based homojunction device. *Journal of Crystal Growth* **326**, 85–89 (2011).
25. Chen, H. C. *et al.* White-Light Electroluminescence From n-ZnO/p-GaN Heterojunction Light-Emitting Diodes at Reverse Breakdown Bias. *IEEE Transactions on Electron Devices* **58**, 3970–3975 (2011).
26. Zhang, S., Wei, S.-H. & Zunger, A. Intrinsic n-type versus p-type doping asymmetry and the defect physics of ZnO. *Physical Review B* **63**, 1–7 (2001).
27. Avrutin, V., Silversmith, D. J. & Morkoc, H. Dopin Asymmetry Problem in ZnO: Current Status and Outlook. *Proceedings of the IEEE* **98**, 1269–1280 (2010).
28. Barnes, T. M., Olson, K. & Wolden, C. a. On the formation and stability of p-type conductivity in nitrogen-doped zinc oxide. *Applied Physics Letters* **86**, 112112 (2005).
29. Lee, J. W., Subramaniam, N. G., Lee, J. C., Kumar S, S. & Kang, T. W. Study of stable p-type conductivity in bismuth-doped ZnO films grown by pulsed-laser deposition. *EPL (Europhysics Letters)* **95**, 47002 (2011).
30. Yang, Y. *et al.* Nonvolatile resistive switching in single crystalline ZnO nanowires. *Nanoscale* **3**, 1917–21 (2011).
31. Zhang, S. B., Wei, S.-H. & Zunger, A. A phenomenological model for systematization and prediction of doping limits in II–VI and I–III–VI[sub 2] compounds. *Journal of Applied Physics* **83**, 3192 (1998).
32. Zhang, S. ., Wei, S.-H. & Zunger, a Overcoming doping bottlenecks in semiconductors and wide-gap materials. *Physica B: Condensed Matter* **273-274**, 976–980 (1999).
33. Avrutin, V., Silversmith, D. & Morkoç, H. Doping asymmetry problem in ZnO: current status and outlook. *Proceedings of the IEEE* (2010).at <http://ieeexplore.ieee.org/xpls/abs_all.jsp?arnumber=5462903>
34. Wager, J. Thermodynamics and kinetics of vacancy self-compensation in wide-bandgap semiconductors. *Philosophical Magazine A* **67**, 897–904 (1993).

35. Kim, K.-K., Kim, H.-S., Hwang, D.-K., Lim, J.-H. & Park, S.-J. Realization of p-type ZnO thin films via phosphorus doping and thermal activation of the dopant. *Applied Physics Letters* **83**, 63 (2003).
36. Onodera, A., Yoshio, K. & Satoh, H. Li-substitution effect and ferroelectric properties in piezoelectric semiconductor ZnO. *Japanese Journal of Applied Physics* **37**, 5315–5317 (1998).
37. Zeng, Y. J. *et al.* Identification of acceptor states in Li-doped p-type ZnO thin films. *Applied Physics Letters* **89**, 042106 (2006).
38. Huang, M. *et al.* Catalytic Growth of Zinc Oxide Nanowires by Vapor Transport. *Advanced Materials* **13**, 113–116 (2001).
39. Ko, H.-J., Chen, Y., Hong, S.-K. & Yao, T. Doping effects in ZnO layers using Li3N as a doping source. *Journal of Crystal Growth* **251**, 628–632 (2003).
40. Yersak, T. a., Trevey, J. E. & Lee, S.-H. In situ lithiation of TiS2 enabled by spontaneous decomposition of Li3N. *Journal of Power Sources* **196**, 9830–9834 (2011).
41. Rauch, C. *et al.* Lithium related deep and shallow acceptors in Li-doped ZnO nanocrystals. *Journal of Applied Physics* **107**, 024311 (2010).
42. Chen, L., Xiong, Z., Wan, Q. & Li, D. Suppression of the formation of interstitial Li through (F, Li) codoping ZnO. *Journal of Physics: Conference Series* **276**, 012158 (2011).
43. Kirste, R. *et al.* Raman and photoluminescence spectroscopic detection of surface-bound Li(+)O2(-) defect sites in Li-doped ZnO nanocrystals derived from molecular precursors. *Chemphyschem* **12**, 1189–95 (2011).
44. Lee, J. *et al.* P-type conduction characteristics of lithium-doped ZnO nanowires. *Advanced materials* **23**, 4183–7 (2011).
45. Thompson, R., Li, D., Witte, C. & Lu, J. Weak localization and electron-electron interactions in Indium-doped ZnO nanowires. *Nano letters* **9**, (2009).
46. Adamopoulo s, G. *et al.* Spray-deposited Li-doped ZnO transistors with electron mobility exceeding 50 cm^2/Vs. *Advanced materials* **22**, 4764–9 (2010).
47. Yankovich, A. *et al.* Stable p-Type Conduction from Sb-Decorated Head-to-Head Basal Plane Inversion Domain Boundaries in ZnO Nanowires. *Nano letters* (2012).at <http://pubs.acs.org/doi/abs/10.1021/nl203848t>
48. Yuan, G. D. *et al.* p-Type ZnO nanowire arrays. *Nano letters* **8**, 2591–7 (2008).
49. Wunnicke, O. Gate capacitance of back-gated nanowire field-effect transistors. *Applied Physics Letters* **89**, 083102 (2006).
50. Khanal, D. & Wu, J. Gate coupling and charge distribution in nanowire field effect transistors. *Nano letters* **7**, 2778–2783 (2007).
51. Garnett, E. C. *et al.* Dopant profiling and surface analysis of silicon nanowires using capacitance – voltage measurements. *Nature Nanotechnology* **4**, 21–23 (2009).
52. Molki, A. Simple Demonstration of the Seebeck Effect. *Science Education Review* **9**, 103–107 (2010).
53. Lee, C.-H., Yi, G.-C., Zuev, Y. M. & Kim, P. Thermoelectric power measurements of wide band gap semiconducting nanowires. *Applied Physics Letters* **94**, 022106 (2009).
54. Pei, Y. *et al.* Stabilizing the optimal carrier concentration for high thermoelectric efficiency. *Advanced materials (Deerfield Beach, Fla.)* **23**, 5674–8 (2011).

Chapter 4

Ionic Conduction in Core/Shell Oxide Nanowires

4.1 - Introduction

4.1.a – Conduction in CeO_2 and ZrO_2

The interest in fuel cells that can operate at lower temperature has spurned research directed at all steps of the process: chemical decomposition, ionic conduction, and species formation. The first and last steps are limited by the catalysts used to perform the individual reactions. While making those reactions occur at low temperatures appears to be the larger of the bottlenecks in the whole process, much work as gone into finding and designing electrolytes capable of conducting the species of interest from anode to cathode (or vice versa).[1,2] Ideally, this electrolyte would require no liquid and be resistant to material corrosion and water management problems.[2–8] The all-solid-state construction of solid-oxide fuel cells using ceramics and metals satisfy such requirements, save the low operation temperatures. SOFCs are typically run anywhere from 1073–1273 K, which is not practical for some applications.[1,9–12] Therefore, much research has been devoted to designing new oxide materials capable of operating at lower temperatures.

In general, there are two types of electrolyte (i.e., oxygen-ion and proton-conducting electrolytes) possible for use in SOFCs. To date, many studies have focused on SOFC technology using oxygen-ion conducting electrolytes because of the chemical stability and low electrical resistance of oxygen-ion conductors. Two of the most commonly used oxides are stabilized zirconia and doped ceria. These materials, when doped appropriately, are ionically conducting.[13–15] For ZrO_2, doping with yttrium locks the structure into the fluorite structure, which can conduct O^- through the oxygen vacancies. Similarly, ionic conduction in CeO_2 occurs through naturally occurring or doping-induced oxygen vacancies. CeO_2 also conducts electrons, making it a mixed conductor in certain environments.[16,17]

4.1.b – Nanoscale Effects on Ionic Conduction in Oxides

Besides adding exotic dopants to try to tailor conduction in CeO_2 and ZrO_2, nanostructuring the materials has been shown to vary conduction properties.[7,11,18–21] Increases

in electrical conductivity over ionic conductivity have been demonstrated in CeO_2 by shrinking the gain size down to the nanoscale.[22] Different effects have been shown to happen to ZrO_2 when similarly structured. However, the real interesting effects can be observed in the combination of the two materials. By simply combining the two materials in a solid solution, increases in the overall conduction have been observed.[23] Furthermore, using the same two materials, increases in ionic conductivity can also occur by layering them on one another.[24] This indicates that the interface between the two materials could provide a pathway for easier conduction of oxygen ions. The reasons for such increases in ionic conduction are still subjects of many studies.

Therefore, this study developed CeO_2/ZrO_2 core-shell nanowires to demonstrate unique, geometric-based properties for low temperature ionic conductors and oxygen filters. By taking advantage of both the large amount of surface/interface area per unit volume and the special effects (ie, depletion, strain, …) such interfaces have on ionic conduction, nanomaterials not only give promise of optimal device geometries, but also afford the ability to manipulate those geometries in order to deconvolute the relative contribution of the various transport mechanisms towards overall conduction.[20,25,26] The benefits to both the science of ionic transport and practical low temperature devices make this an extremely promising approach.

4.2 – Synthesis of CeO_2/ZrO_2 Nanowires

4.2.a – Hydrothermal Synthesis and Coating Method

Considering also the relatively large amount of sample needed for device fabrication and characterization, hydrothermal synthesis of the nanowires was utilized. Previous reports of CeO_2 nanowire growth involved acidic environments, with great care taken at controlling the pH. This study, however, utilized a basic condition reaction which proved to be more robust:

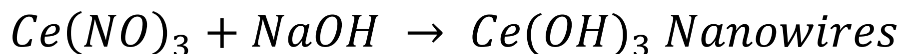

$$Ce(NO)_3 + NaOH \rightarrow Ce(OH)_3\ Nanowires$$

The $Ce(OH)_3$ product from this reaction was nearly 100% of the nanowire morphology with excellent aspect ratio control (Figure 4.1a). Figure 4.1b shows the XRD spectrum which confirmed that the major phase was that of $Ce(OH)_3$, with some slight contribution from CeO_2. This is due to incomplete oxidation of the product during synthesis. Therefore, The $Ce(OH)_3$ nanowires were then annealed at 500 ^oC in air for at least 3 hours to convert them to CeO_2 nanowires (Figure 4.2b). The resulting nanowires are single crystalline, but become shorter, on average (Figure 4.2a). Little to no sintering was observed with this annealing condition.

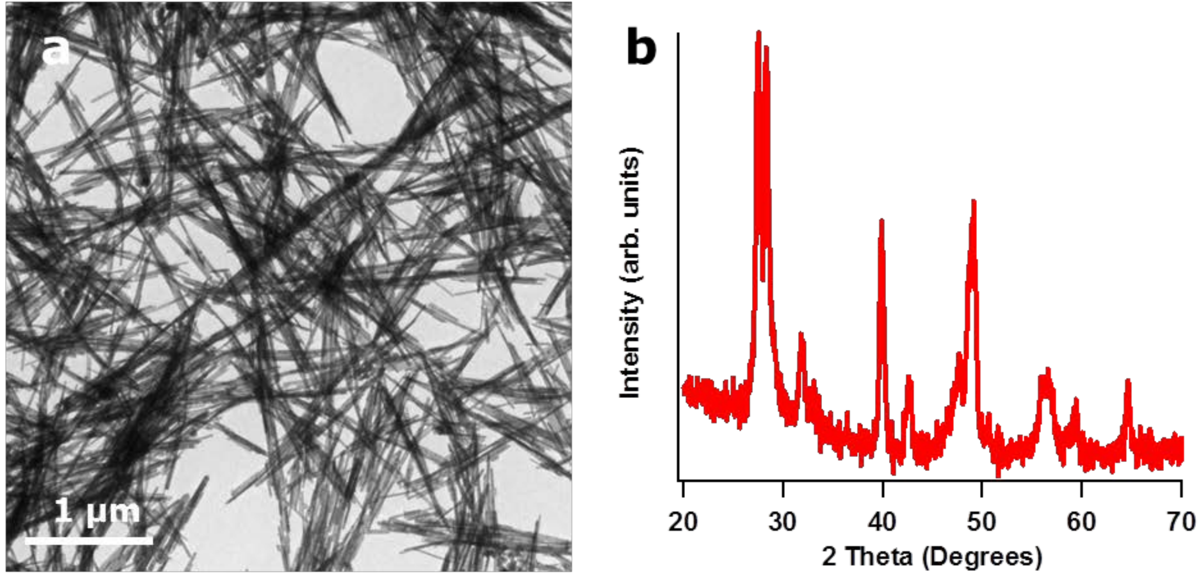

Figure 4.1 – Synthesis of $Ce(OH)_3$: (a) TEM of $Ce(OH)_3$ nanowires. (b) XRD shows peaks of both CeO_2 and $Ce(OH)_3$ phases.

Application of the ZrO_2 was accomplished via a sol gel technique. This process involves mixing a solution of Zirconium Isopropoxide in ethanol with the CeO_2 nanowires and waiting for the solvent to evaporate off (can take longer than 8 hours, depending on concentration). After the ethanol has been removed, a second calcination step was done to crystalize the ZrO_2 shell (600 ^oC in air for at least 2 hours).

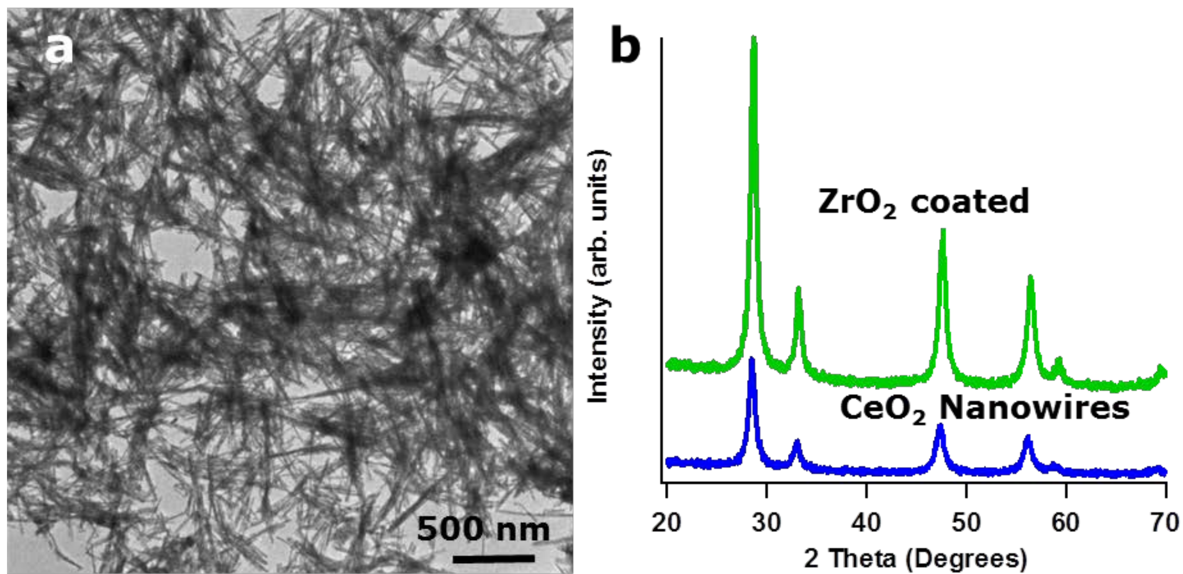

Figure 4.2 – After Calcination: (a) TEM of CeO_2 nanowires. Nanowires are shorter after calcination. (b) XRD shows peaks of CeO_2 even on samples coated with ZrO_2

4.2.b – Shell Crystallization

After application and calcination of the shell, no new peaks associated with ZrO_2 were observed in the XRD (Figure 4.2b). To check the crystallinity of the shell, HRSTEM and HRTEM were performed. Figure 4.3a gives an example of the crystallinity of the shell. Domains measured up to hundreds of nanometers, but the shell thickness varied from 3-10 nanometers in different areas. To confirm the shell and core constituents, line scan EELS were performed near the edge of the structure (Figure 4.3b). Little to no diffusion was observed across the interface. The slight increase in the Zr signal after the core has been cleared is due to the larger amount of Zr interacting with the electron beam before scattering by some other species.

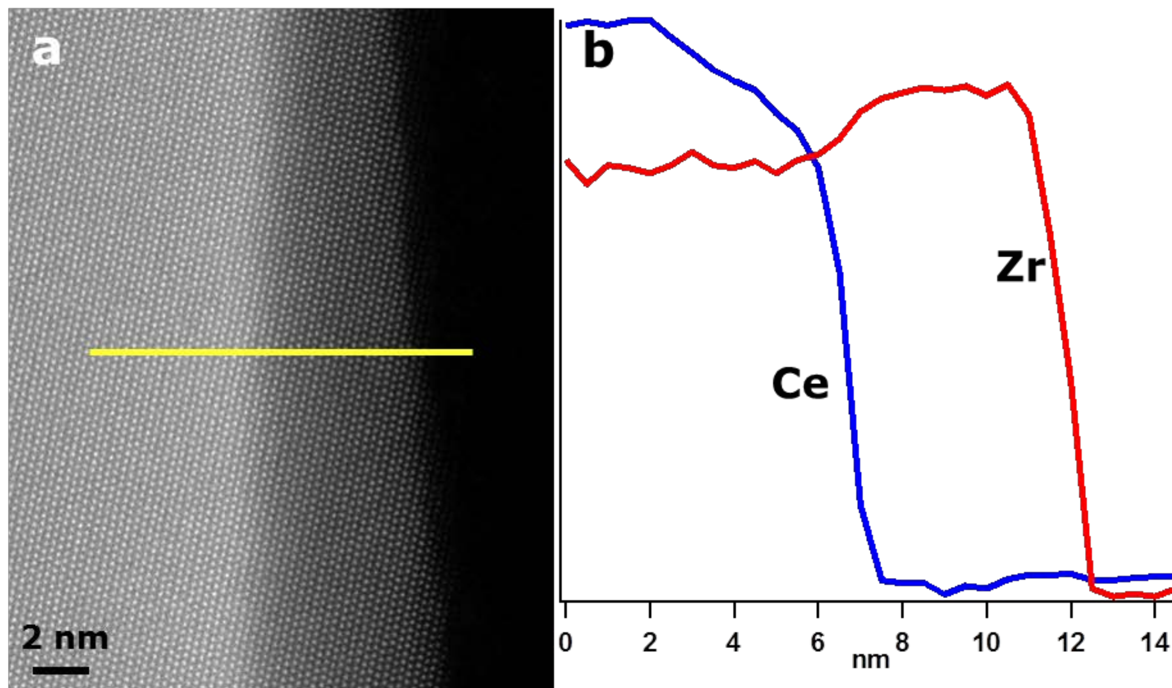

Figure 4.3 – Coating Structure: (a) HRSTEM of CeO_2 coated with ZrO_2. (b) EELS lines scan of Ce and Zr show no notable diffusion of the materials into one another. The yellow line indicates the area examined.

4.2.c – Interfacial Structure

The actual interfacial structure was investigated by HRTEM. In Figure 4.4a, the core and shell are clearly denoted due to intentional underfocusing. Now that the interface position is established, the focused and slightly filtered image in Figure 4.4b gives a much clearer picture as to the crystal relation, or lack thereof, between the two materials (note the filter used was a FFT mask to reduce noise around the atomic lines). The image shows that there is no relation between the materials, making this an incoherent interface.[20] Therefore any transport effects seen from the addition from the ZrO_2 coating are not strain related.

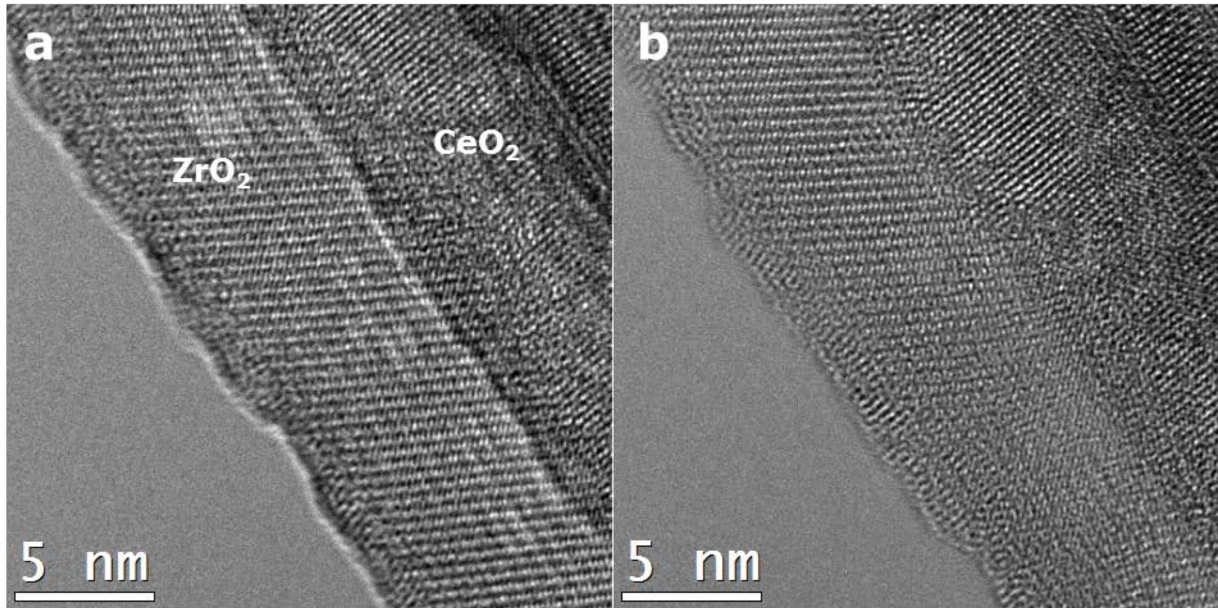

Figure 4.4 – Interfacial Relation: (a) HRTEM of CeO_2 coated with ZrO_2 after calcination taken under focused. (b) Partially Fourier-filtered image in focus.

4.3 – Nanowire Thin Films

While performing single nanowire impedance measurements is always the goal for the maximum amount of directly interpretable data, ionic conduction currents occur on far too low of a level for current impedance analyzers to measure accurately. Therefore, nanowire thin film networks were utilized for the purpose of measurement signal. Not only are these nanowire thin films easier to measure, but they are more robust and still contain a large interface to volume ratio.

4.3.a – ZrO_2 Coating Schemes

With the validation of nanowire thin films established, the question regarding how to apply the shell remains. In general, for the current system and synthetic methods in hand, there are two ways the CeO_2/ZrO_2 nanowire thin film could be constructed, each with its own consequences. The first scheme considered is pictorially described on the left side of Figure 4.5. This method involves applying the ZrO_2 coating while the CeO_2 nanowires are still in solution followed by drying into a film. After film formation, perform the second calcination to crystalize the ZrO_2.

This method was ultimately not perused, even though it provides some inherent benefits. Those benefits include a higher degree of conformity in the shell coating, as well as ease of process. However, this conformity also prevents any CeO_2 nanowires from being in intimate contact with any other CeO_2 nanowire, hence the “Separate” designation. If the

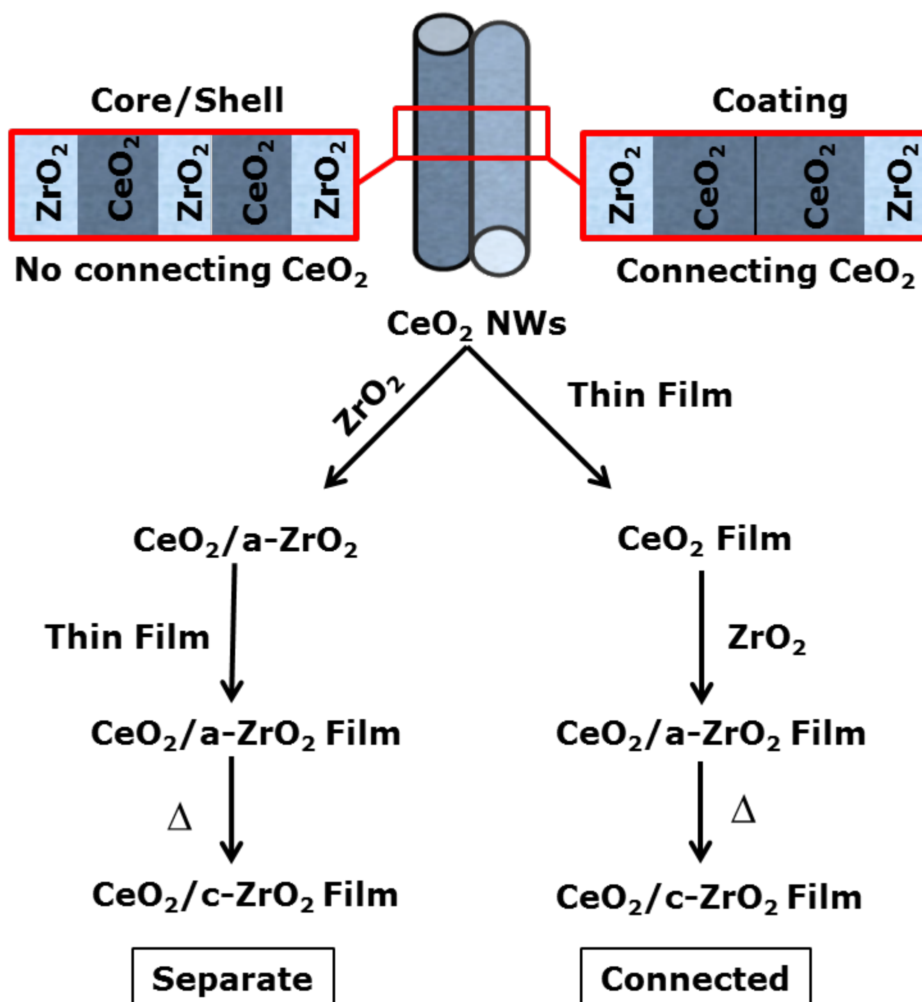

Figure 4.5 – General Scheme for Nanowire Thin Film Designs: Schematic of the 2 possible scenarios that are possible with the available materials and application methods. All measurements discussed in this work are of the Connected construction.

interface effects are to be observed, those interfaces must be continuous from contact to contact. Otherwise, transport will be limited by the more resistive ZrO_2.

With this in mind, the method of first creating the nanowire thin film, then applying the ZrO_2 coating, was used (right side of Figure 4.5). This design allows for the connection between CeO_2 nanowires to remain intact, while still providing a relatively large amount of interface exposed to the ZrO_2 ("Connected" motif). Additionally, this design allows for the same film to be measured before and after coating.

4.3.b – Thin Film Creation and Optimization

Nanowire thin films were created by drop casting CeO_2 nanowire solution onto 1 x 1 cm^2 Pt-covered quartz substrates and allowing the solvent to slowly evaporate. The importance of the rate of evaporation is seen by the film quality, where films dried more quickly had a larger distribution of thicknesses across the substrate. When performed slowly enough, film

thicknesses in the center 50-60% of the substrate varied by only < 7%. The average thickness of the films was then controlled via the concentration of the CeO_2 nanowire solution. Measured devices varied in thickness from 210 nm to 1.3 μm. Figure 4.6b is a cross-section SEM image of such a nanowire film on a Pt-covered substrate.

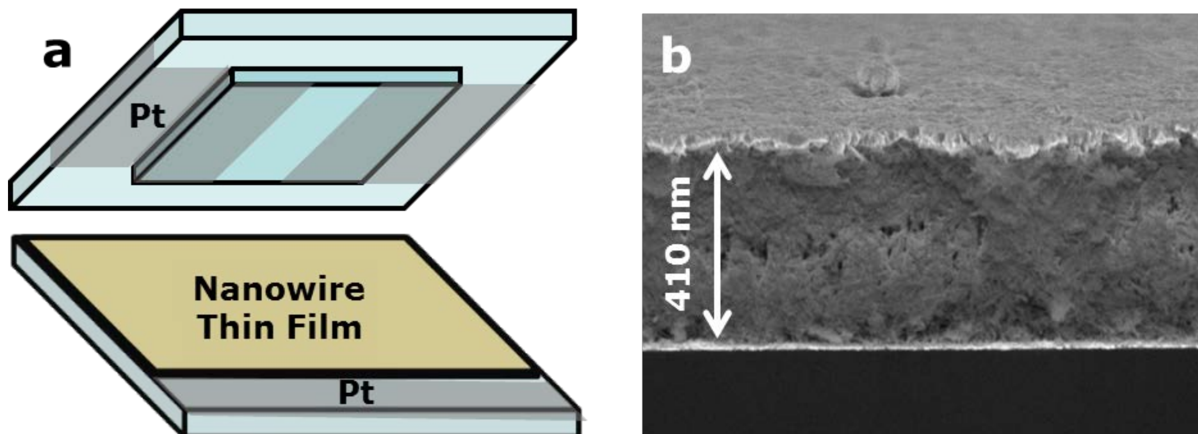

Figure 4.6 – Nanowire Thin Films: (a) Schematic of the device structure used to measure cross plane conductivity. (b) Cross section SEM of a nanowire thin film. Pt was deposited on the surface for better image quality.

4.3.c – Contacting Considerations

The top contacts used for the cross-plane measurement are depicted in Figure 4.6a. They consist of etched quartz, such that the 5mm x 5mm center protrudes out nearly 400 microns. Pt deposited on the etched side defines the contact area with the thin film. To ensure adequate electrical contact, the top contact and substrate are pressed and held together with force from a loaded spring controller. For the ZrO_2 coated samples, the additional step of etching (Ar plasma, 100 W, 60 seconds) through the initial layer of ZrO_2 is needed for reliable contact.

4.4 – Ionic Conduction

The impedance of the thin film samples was measured using a Bio-Logic VSP and VMP3B-5 potentiostat. The frequency range used was 1 M Hertz to 1 Hertz. Nyquist plots exhibiting ionic conduction were fit to semi circles, ignoring data points that were acquired outside the measurement range of the instrument. Samples were held in various partial pressures of O_2 for 2 hours in ensure stability. Note that the data in the section were gathered from the same sample, measured first as pure CeO_2 nanowire thin film, then again after ZrO_2 coating.

4.4.a – Activation Energy

Figure 4.7 plots the ionic conductivity as a function of temperature for a CeO2 nanowire thin film in various O_2 environments. Activation energies calculated from these Arrhenius Plots are between 1.1-1.3 eV. This is comparable to other reports of pure CeO_2, bulk and polycrystalline. The highest conductivity measured at 650 oC is about an order of magnitude lower than what previous studies have found. This could be attributed to both the porosity of the film (not considered in the geometry) and resistance at the contacts. Even though the conductivity of the pure CeO_2 nanowire film is low, the conductivity increases by over an order of magnitude upon application of the ZrO_2 coating (Figure 4.8). Additionally, the activation energy calculated from the data in Figure 4.8 is .81-.85 eV. This substantial drop in the activation energy required to conduct ions through the material is an indication that either the mechanism or pathway of conduction has changed.

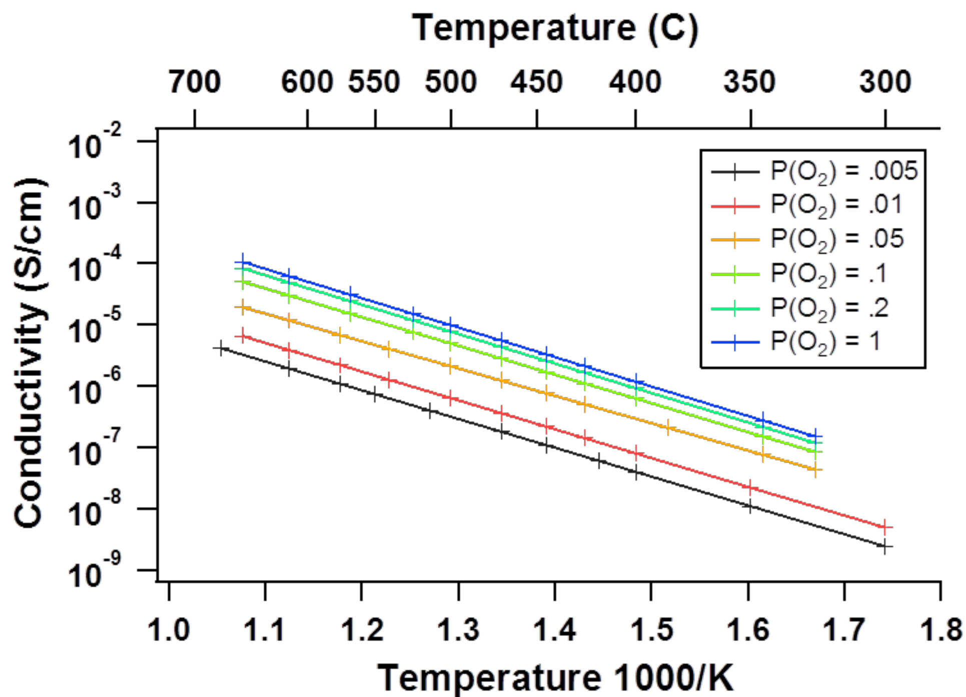

Figure 4.7 – Ionic Conductivity of CeO_2 Nanowire Thin Films: Ionic Conductivity as a function of temperature for pure CeO_2 nanowires in various oxygen environments.

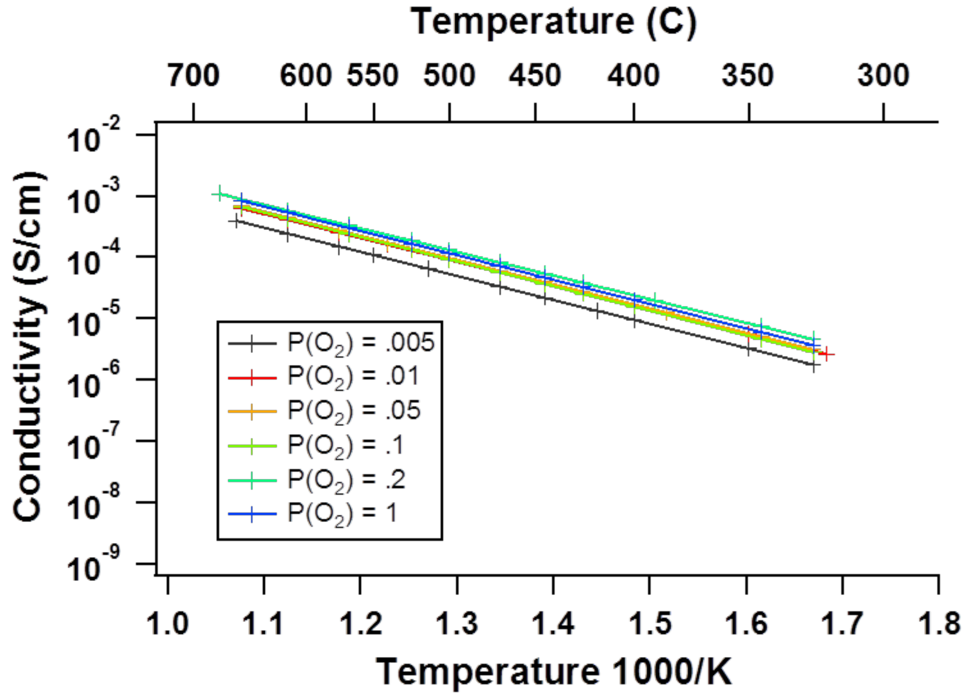

Figure 4.8 – Ionic Conductivity of CeO_2/ZrO_2 Nanowire Thin Films: Ionic Conductivity as a function of temperature for pure CeO_2/ZrO_2 nanowires in various oxygen environments. No real dependence was observed.

4.4.b – Ionic Transport Number

To analyze the relative contributions of electrons and ions towards the total conduction, the ratio of the ionic impedance measured from the Nyquist plot to the DC resistance was measured. This is known as the ionic transport number (ITN), where 1 is conduction occurs completely by ionic species. The ITN for the ZrO_2 coated CeO_2 nanowire film is plotted as a function of temperature in Figure 4.9. As temperature increases, the amount of energy needed to conduct oxygen is more readily available, thereby increasing the relative amount of ionic conduction. When measured in various O_2 atmospheres, there seems to be little change in the overall trend w.r.t temperature. Presumably, CeO_2 becomes more electrically conductive in reducing, or non-oxidative, conditions. However, this trend is somewhat lessened by the presence of the ZrO_2 coating, which may be acting as an oxidative barrier to the CeO_2.[27]

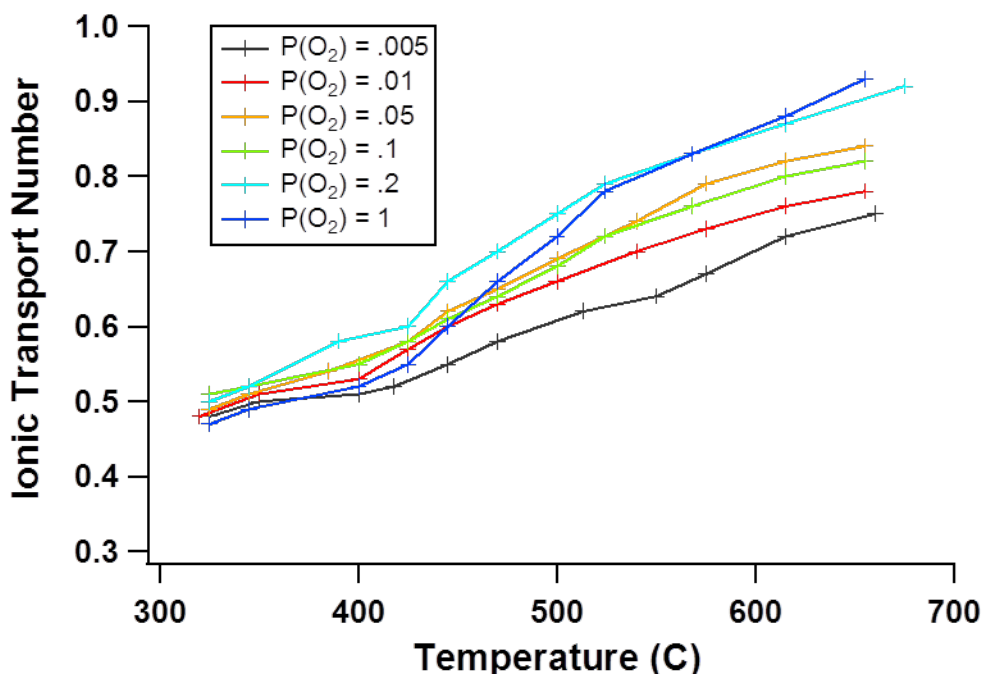

Figure 4.9 – Ionic Transport Number of CeO_2/ZrO_2 Nanowire Thin Films: As the temperature increases, the ratio of ionic conduction to electrical conduction increases.

4.4.c – Dependence on O_2 Partial Pressure

Further evidence of this change in conduction mechanism is seen in the dependence on O_2 partial pressure. Qualitatively, it is obvious from Figures 4.7 and 4.8 that the CeO_2 film has a dependence on the oxidative environment while the ZrO_2 coated sample does not. A more quantitative representation of the dependences of the two films is shown in Figure 4.10 (red lines, left axis). As the partial pressure of oxygen decrease, the CeO_2 sample also decrease in ionic conductivity. Simultaneously, the ITN for CeO_2 is also decreasing, with a sharp change occurring between 10-20% oxygen partial pressure. This is an indication that the ceria is changing more into an electrical conductor, possibly by changing oxidation state.

The calculated ITN of the ZrO_2 coated sample does not have as sharp of a drop as a function of partial pressure of oxygen. In fact, ionic conduction remains resilient in even the more reducing environments, as compared to the pure CeO_2 nanowire measurement. This result provides more evidence that the ZrO_2 coating is providing shielding for conduction to occur at the interface.

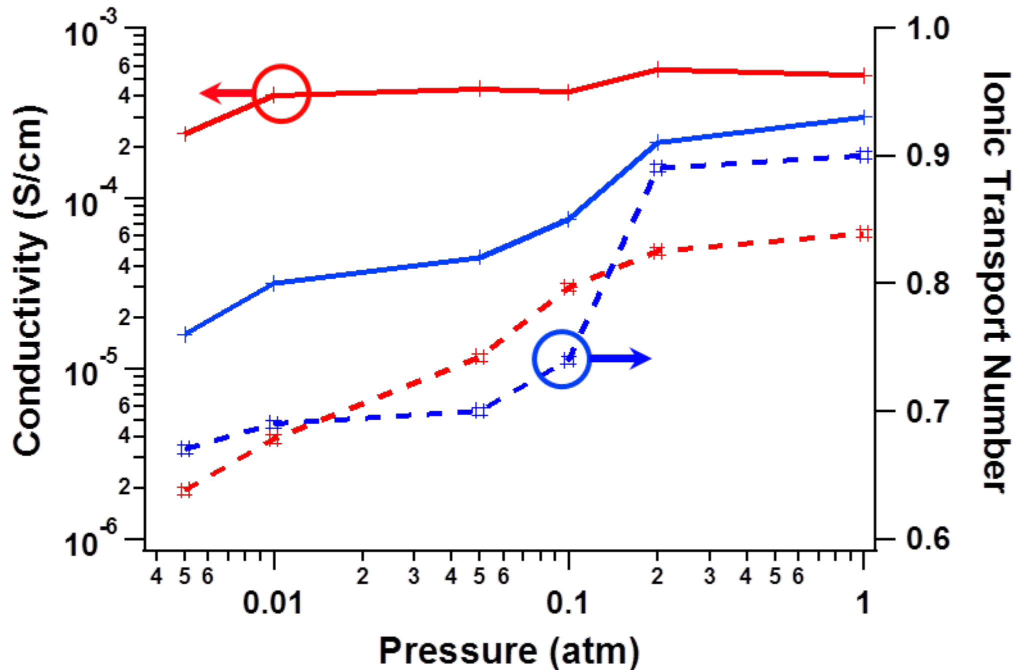

Figure 4.10 – Effects of ZnO_2 on Nature of Conduction: Conductivity (red, left axis) and ITN (blue, right axis) at 615 °C as function of partial pressure of O_2 for both CeO2 (dashed lines) and CeO_2/ZrO_2 (solid lines).

4.5 – Conclusions

The exact role the ZrO_2 coating plays in enhancing the ionic conduction in the CeO_2 nanowire system requires more study. However, the demonstration of the incoherent interface between the two materials indicates that strain effects do not contribute. Therefore, possible depletion in the CeO_2 from the coating could cause oxygen to become more mobile near the interface. A shell-thickness dependence study is required to definitively assign blame to that specific reason. Yet this data indicates that improvements in conduction can be made through nanostructuring the interface between materials. This methodology continues to hold promise to unlock the possibility of a room temperature ionic conductor.

4.6 – References

1. Patcharavorachot, Y., Brandon, N. P., Paengjuntuek, W., Assabumrungrat, S. & Arpornwichanop, A. Analysis of planar solid oxide fuel cells based on proton-conducting electrolyte. *Solid State Ionics* **181**, 1568–1576 (2010).
2. Marques, F. *et al.* Oxygen ion conductors for fuel cells and membranes: selected developments. *Solid State Ionics* **177**, 1697–1703 (2006).
3. Tarancón, A., Burriel, M., Santiso, J., Skinner, S. J. & Kilner, J. a. Advances in layered oxide cathodes for intermediate temperature solid oxide fuel cells. *Journal of Materials Chemistry* **20**, 3799 (2010).
4. Tao, S. & Irvine, J. T. S. A redox-stable efficient anode for solid-oxide fuel cells. *Nature Materials* **2**, 320–3 (2003).
5. Menzler, N. H., Tietz, F., Uhlenbruck, S., Buchkremer, H. P. & Stöver, D. Materials and manufacturing technologies for solid oxide fuel cells. *Journal of Materials Science* **45**, 3109–3135 (2010).
6. Nesaraj, A. Recent developments in solid oxide fuel cell technology-a review. *Journal of Scientific & Industrial Research* **69**, 169–176 (2010).
7. Orera, a. & Slater, P. R. New Chemical Systems for Solid Oxide Fuel Cells †. *Chemistry of Materials* **22**, 675–690 (2010).
8. Sun, C., Hui, R. & Roller, J. Cathode materials for solid oxide fuel cells: a review. *Journal of Solid State Electrochemistry* **14**, 1125–1144 (2009).
9. Fabbri, E., Pergolesi, D. & Traversa, E. Materials challenges toward proton-conducting oxide fuel cells: a critical review. *Chemical Society reviews* **39**, 4355–69 (2010).
10. Kuhn, M. & Napporn, T. W. Single-Chamber Solid Oxide Fuel Cell Technology—From Its Origins to Today's State of the Art. *Energies* **3**, 57–134 (2010).
11. Jacobson, A. J. Materials for Solid Oxide Fuel Cells †. *Chemistry of Materials* **22**, 660–674 (2010).
12. Tarancón, A. Strategies for Lowering Solid Oxide Fuel Cells Operating Temperature. *Energies* **2**, 1130–1150 (2009).
13. Malzbender, J., Steinbrech, R. W. & Singheiser, L. A review of advanced techniques for characterising SOFC behaviour. *Fuel Cells* **9**, 785–793 (2009).
14. Murray, E., Tsai, T. & Barnett, S. A direct-methane fuel cell with a ceria-based anode. *Nature* **400**, 649–651 (1999).
15. Garcia-Barriocanal, J. *et al.* Colossal ionic conductivity at interfaces of epitaxial ZrO2:Y2O3/SrTiO3 heterostructures. *Science* **321**, 676–80 (2008).
16. Yahiro, H., Eguchi, Y., Eguchi, K. & Arai, H. Oxygen ion conductivity of the ceria-samarium oxide system with fluorite structure. *Journal of applied electrochemistry* **18**, 527–531 (1988).
17. Fagg, D. P. *et al.* Ceria based mixed conductors with adjusted electronic conductivity in the bulk and/or along grain boundaries. *Solid State Ionics* **180**, 896–899 (2009).

18. Brinkman, K. S., Takamura, H., Tuller, H. L. & Iijima, T. The Oxygen Permeation Properties of Nanocrystalline CeO2 Thin Films. *Journal of the Electrochemical Society* **157**, B1852 (2010).
19. Sillassen, M. *et al.* Low-Temperature Superionic Conductivity in Strained Yttria-Stabilized Zirconia. *Advanced Functional Materials* **20**, 2071–2076 (2010).
20. Maier, J. Nanoionics: ionic charge carriers in small systems. *Physical Chemistry Chemical Physics* **11**, 3011–3022 (2009).
21. Bellino, M. G., Lamas, D. G. & Walsöe de Reca, N. E. Preparation and ionic transport properties of YDC–YSZ nanocomposites. *Journal of Materials Chemistry* **18**, 4537 (2008).
22. Tschope, A., Kilassonia, S., Zapp, B. & Birringer, R. Grain-size-dependent thermopower of polycrystalline cerium oxide. *Solid State Ionics* **149**, 261–273 (2002).
23. Lee, J., Yoon, S. M., Kim, B., Lee, H. & Song, H. S. Electrical conductivity and defect structure of CeO2 -ZrO2 mixed oxide. *Journal of Materials Science* **7**, 1165–1171 (2002).
24. Azad, S. *et al.* Nanoscale effects on ion conductance of layer-by-layer structures of gadolinia-doped ceria and zirconia. *Applied Physics Letters* **86**, 131906 (2005).
25. Guo, X. & Maier, J. Ionically Conducting Two-Dimensional Heterostructures. *Advanced Materials* **21**, 2619–2631 (2009).
26. Tuller, H. L., Litzelman, S. J. & Jung, W. Micro-ionics: next generation power sources. *Physical chemistry chemical physics* **11**, 3010 (2009).
27. Dalmaschio, C. J. *et al.* Oxide surface modification: synthesis and characterization of zirconia-coated alumina. *Journal of colloid and interface science* **343**, 256–62 (2010).

Appendix:

List of Publications

1. **S. C. Andrews**, M. A. Fardy, M. C. Moore, S. Aloni, M. Zhang, V. Radmilovic, P. Yang, “Atomic-Level Control of the Thermoelectric Properties in Polytypoid Nanowires,” *Chem. Sci.*, 2, 706, 2011
2. J. Lim, K. Hippalgaonkar, **S. C. Andrews**, A. Majumdar, P. Yang, “Quantifying Surface Roughness Effects on Phonon Transport in Silicon Nanowires,” *Nano Letters*, 12, 2475, 2012
3. C. Hahn, M. A. Fardy, C. Nguyen, M. Natera-Comte, **S. C. Andrews**, P. Yang, “Synthesis and Photocatalytic Properties of Single Crystalline (Ga1-xZnx)(N1-xOx) Nanotubes,” *Israel J. Chem.*, 52,11-12, 2012
4. H. Gao, A. Fu, **S. C. Andrews**, P. Yang, “Cleaved-Coupled Nanowire Lasers,” *PNAS*, 110, 3, 865-869, 2013
5. C. Hahn; A.A. Cordones, **S. C. Andrews**, H. Gao, A, Fu, S.R. Leone, P. Yang, “Effect of Thermal Annealing in Ammonia on the Properties of InGaN Nanowires with Different Indium Concentration,” *J. Phys. Chem. C.*, 117, 7, 2013
6. J. Henzie, **S. C. Andrews**, X.Y. Ling, Z. Li, P. Yang, “Oriented Assembly of Polyhedral Plasmonic Nanoparticle Clusters,” *PNAS*, Early Edition, 2013
7. B. Liu, H. M. Chen, C. Liu, **S. C. Andrews**, C. Hahn, C. H. Wu, P. Yang, “Large-Scale Synthesis of Transition-metal Doped TiO_2 Nanowires with Controllable Overpotential,” Submitted, 2013
8. N.P. Dasgupta, C. Liu, **S.C. Andrews**, F.B. Prinz, P. Yang, “Atomic Layer Deposition of Platinum Catalysts on Nanowire Surfaces for Photoelectrochemical Water Reduction,” Submitted, 2013
9. A. P. Goldstein, **S. C. Andrews**, R. F. Berger, J. B. Neaton, P. Yang, “Zigzag Inversion Domain Boundaries in Indium Zinc Oxide-Based Nanowires: Structure and Formation,” Submitted, 2013
10. J. Lim, H. Wang, J. Tang, **S. C. Andrews**, D. Lee, and P. Yang, “Simultaneous measurement of electrical and thermal properties of holey silicon for thermoelectric application,” In Preparation
11. **S. C. Andrews**, H. M. Chen, B. Liu, J. Lee, P. Yang, “Ionic Transport in CeO_2/ZrO_2 Core/Shell Nanostructures,” In Preparation
12. **S. C. Andrews**, B. Wiers, P. Yang, J. Long, “Electrical Conduction in single crystal $Fe_2(bdp)_3$ MOF,” In Preparation